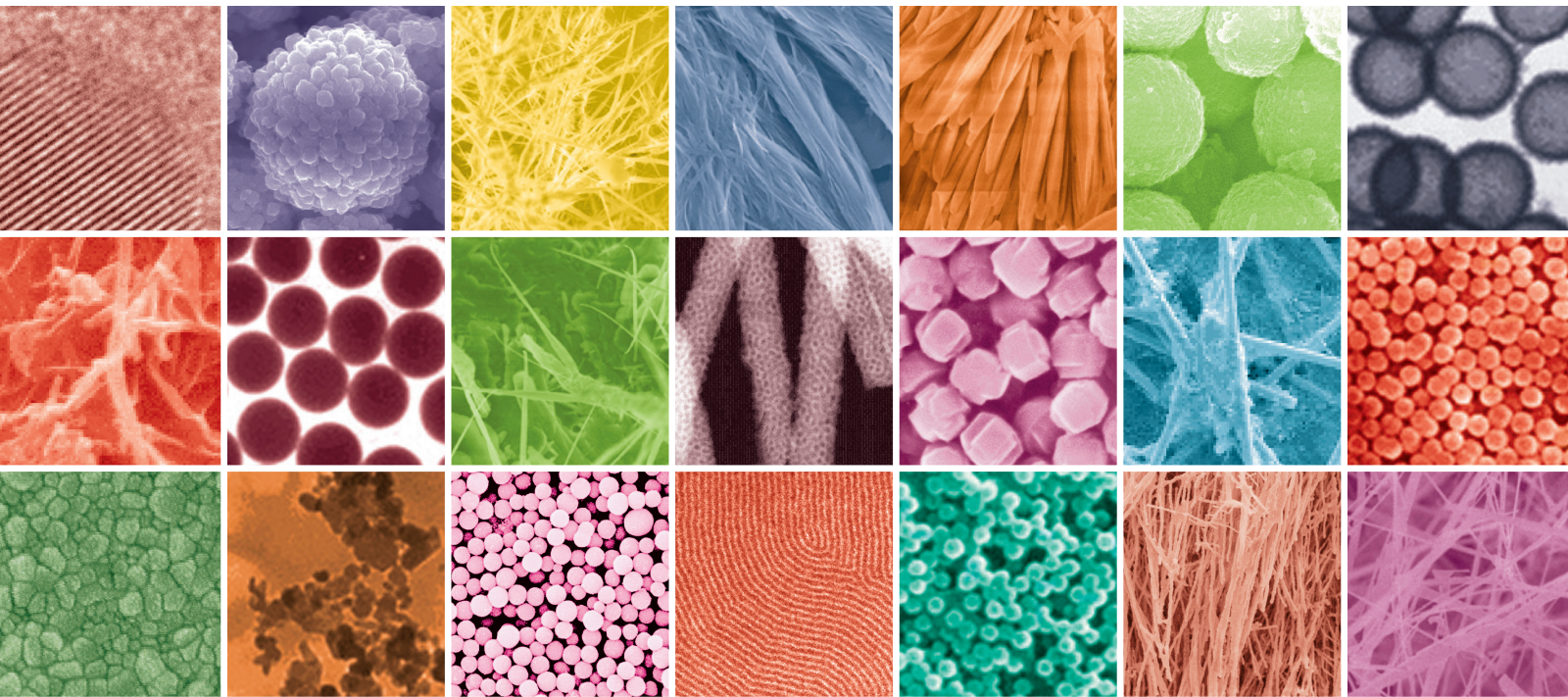


Multifunctional Nanomaterials for Biomedical Engineering: Unique Properties, Fabrications, and Diverse Applications

Guest Editors: Jen-Jie Chieh, Sharmila M. Mukhopadhyay, and Yali Cui





Multifunctional Nanomaterials for Biomedical Engineering: Unique Properties, Fabrications, and Diverse Applications

Multifunctional Nanomaterials for Biomedical Engineering: Unique Properties, Fabrications, and Diverse Applications

Guest Editors: Jen-Jie Chieh, Sharmila M. Mukhopadhyay,
and Yali Cui



Copyright © 2015 Hindawi Publishing Corporation. All rights reserved.

This is a special issue published in "Journal of Nanomaterials." All articles are open access articles distributed under the Creative Commons Attribution License, which permits unrestricted use, distribution, and reproduction in any medium, provided the original work is properly cited.

Editorial Board

Katerina Aifantis, Greece
Nageh K. Allam, USA
Margarida Amaral, Portugal
Xuedong Bai, China
Enrico Bergamaschi, Italy
Theodorian Borca-Tasciuc, USA
C. Jeffrey Brinker, USA
Christian Brosseau, France
Xuebo Cao, China
Sang-Hee Cho, Republic of Korea
Shafiq Chowdhury, USA
Cui Chunxiang, China
Miguel A. Correa-Duarte, Spain
Shadi A. Dayeh, USA
Ali Eftekhari, USA
Claude Estournes, France
Alan Fuchs, USA
Lian Gao, China
Russell E. Gorga, USA
Hongchen Chen Gu, China
Mustafa O. Guler, Turkey
John Zhanhu Guo, USA
Smrati Gupta, Germany
Michael Harris, USA
Zhongkui Hong, USA
Michael Z. Hu, USA
David Hui, USA
Y.-K. Jeong, Republic of Korea
Sheng-Rui Jian, Taiwan
Wanqin Jin, China
Rakesh K. Joshi, India
Zhenhui Kang, China

Fathallah Karimzadeh, Iran
Do Kyung Kim, Republic of Korea
Kin Tak Lau, Australia
Burtrand Lee, USA
Benxia Li, China
Jun Li, Singapore
Shijun Liao, China
Gong Ru Lin, Taiwan
J.-Y. Liu, USA
Jun Liu, USA
Tianxi Liu, China
Songwei Lu, USA
Daniel Lu, China
Jue Lu, USA
Ed Ma, USA
Gaurav Mago, USA
Sanjay R. Mathur, Germany
Nobuhiro Matsushita, Japan
A. McCormick, USA
Vikas Mittal, UAE
Weihai Ni, Germany
Sherine Obare, USA
Edward Andrew Payzant, USA
Kui-Qing Peng, China
Anukorn Phuruangrat, Thailand
Ugur Serincan, Turkey
Huaiyu Shao, Japan
Donglu Shi, USA
Suprakas Sinha Ray, South Africa
Vladimir Sivakov, Germany
Marinella Striccoli, Italy
Bohua Sun, South Africa

Saikat Talapatra, USA
Nairong Tao, China
Titipun Thongtem, Thailand
Somchai Thongtem, Thailand
Valeri P. Tolstoy, Russia
Tsung-Yen Tsai, Taiwan
Takuya Tsuzuki, Australia
Raquel Verdejo, Spain
Mat U. Wahit, Malaysia
Shiren Wang, USA
Yong Wang, USA
Cheng Wang, China
Zhenbo Wang, China
Jinquan Wei, China
Ching Ping Wong, USA
Xingcai Wu, China
Guodong Xia, Hong Kong
Zhi Li Xiao, USA
Ping Xiao, UK
Shuangxi Xing, China
Yangchuan Xing, USA
N. Xu, China
Doron Yadlovker, Israel
Ying-Kui Yang, China
Khaled Youssef, USA
Kui Yu, Canada
Haibo Zeng, China
Tianyou Zhai, Japan
Renyun Zhang, Sweden
Yanbao Zhao, China
Lianxi Zheng, Singapore
Chunyi Zhi, Japan

Contents

Multifunctional Nanomaterials for Biomedical Engineering: Unique Properties, Fabrications, and Diverse Applications, Jen-Jie Chieh, Sharmila M. Mukhopadhyay, and Yali Cui
Volume 2015, Article ID 942698, 2 pages

Physicochemical Analysis of the Polydimethylsiloxane Interlayer Influence on a Hydroxyapatite Doped with Silver Coating, C. L. Popa, A. Groza, P. Chapon, C. S. Ciobanu, R. V. Ghita, R. Trusca, M. Ganciu, and D. Predoi
Volume 2015, Article ID 250617, 10 pages

Comparison of the Effect of Sol-Gel and Coprecipitation Routes on the Properties and Behavior of Nanocomposite Chitosan-Bioactive Glass Membranes for Bone Tissue Engineering, Elke M. F. Lemos, Sandhra M. Carvalho, Patrícia S. O. Patrício, Claudio L. Donnici, and Marivalda M. Pereira
Volume 2015, Article ID 150394, 8 pages

Effectiveness of Two Self-Etchings Bonded Clinically in Caries Affected Dentin with Homogeneous Smear Layer, Roberto Pinna, Paolo Usai, Mariantonietta Arrica, and Egle Milia
Volume 2015, Article ID 489183, 7 pages

Assaying Biomarkers via Real-Time Measurements of the Effective Relaxation Time of Biofunctionalized Magnetic Nanoparticles Associated with Biotargets, Shu-Hsien Liao, Jean-Hong Chen, Yu-Kai Su, Kuen-Lin Chen, Heng-Er Horng, and Hong-Chang Yang
Volume 2015, Article ID 497296, 7 pages

Time-Evolution Contrast of Target MRI Using High-Stability Antibody Functionalized Magnetic Nanoparticles: An Animal Model, K. W. Huang, S. Y. Yang, H. E. Horng, J. J. Chieh, H. H. Chen, C. C. Wu, J. H. Chen, I.T. Lin, C. C. Yang, and H. C. Yang
Volume 2014, Article ID 351848, 7 pages

Editorial

Multifunctional Nanomaterials for Biomedical Engineering: Unique Properties, Fabrications, and Diverse Applications

Jen-Jie Chieh,¹ Sharmila M. Mukhopadhyay,² and Yali Cui³

¹*Institute of Electro-Optical Science and Technology, National Taiwan Normal University, Taipei 116, Taiwan*

²*Mechanical & Materials Engineering, Wright State University, Dayton, OH 45324, USA*

³*National Engineering Research Center for Miniaturized Detection Systems, Xi'an, Shaanxi 710069, China*

Correspondence should be addressed to Jen-Jie Chieh; jjchieh@ntnu.edu.tw

Received 3 May 2015; Accepted 3 May 2015

Copyright © 2015 Jen-Jie Chieh et al. This is an open access article distributed under the Creative Commons Attribution License, which permits unrestricted use, distribution, and reproduction in any medium, provided the original work is properly cited.

Nanomaterials possess many unique properties useful for biomedical applications ranging from preoperative and intra-operative imaging to coatings, assays, and cell scaffolds. Their popularity and production value are full of competitiveness. Their related methodologies and instruments are also created or emphasized as the mainstream. Since multifunctional nanomaterials attract interests and attention of researchers, engineers, and businessmen in biomedical engineering, this journal is set up to publish a special issue devoted to this topic. The result is a collection of five original research articles, whose authors belong to academic or research institutions of five different countries from Asia, Europe, and America. Papers are representative of a large share of biomaterials with multiple functions, applications and syntheses, and characteristic methods.

From a scientific and engineering point of view, the perspective is to promote merits of biomaterials. S.-H. Liao et al. from Taiwan (“Assaying Biomarkers via Real-Time Measurements of the Effective Relaxation Time of Biofunctionalized Magnetic Nanoparticles Associated with Biotargets”) proposed two different methods for assaying alpha-fetoprotein biomarkers of liver cancers based on the same biofunctionalized magnetic nanoparticles. One is the effective relaxation time by the ac magnetic susceptometer, and the other is saturation magnetization by the vibrating sample magnetometer. Both showed the high future clinical possibility. E. M. F. Lemos et al. from Brazil (“Comparison of the Effect of Sol-Gel and Coprecipitation Routes on the Properties and Behavior of Nanocomposite Chitosan-Bioactive Glass Membranes for Bone Tissue Engineering”) developed

hybrid composite films for achieving adequate performance for the application as a guide to the cell growth of bone tissue. There were two synthetic routes of sol-gel and coprecipitation by combining chitosan (CS) with bioactive glass in solution form (BG-Sol) and in nanoparticle dispersion form (BGNP) by the two different synthesis routes. Both systems of CS-BG as CS-BGNP films exhibited high tensile strength, high bioactivity, and cell viability. These results indicate that the use of bioactive glass successfully acted as an agent for loading and improved bioactivity, particularly in the form of nanoparticle dispersion (BGNP), whose results are the most promising. R. Pinna et al. from Italy (“Effectiveness of Two Self-Etchings Bonded Clinically in Caries Affected Dentin with Homogeneous Smear Layer”) characterized the interface of two self-etching adhesives bonded in carious affected dentin with homogeneous smear layer. The observation of nanoscale structures by TEM was used to study different factors, such as different two-step self-etching systems and clinical conditions of pulpal pressure. Hence, this work originally proposed the correlate self-etchings with the heterogeneous aspects of vital carious affected dentin, which occur in daily practice under clinical conditions. K. W. Huang et al. from Taiwan (“Time-Evolution Contrast of Target MRI Using High-Stability Antibody Functionalized Magnetic Nanoparticles: An Animal Model”) developed the surface biofunctions, Fe₃O₄ magnetic nanoparticles for the ability of immunoassay by immunomagnetic reduction, and in vivo target labeling by magnetic resonance imaging. This work verified the application of nanoparticles to both MRI contrast and immunoassay of a colorectal cancer.

C. L. Popa et al. from Romania (“Physicochemical Analysis of the Polydimethylsiloxane Interlayer Influence on a Hydroxyapatite Doped with Silver Coating”) described the captivating physico-chemical process during the interaction of a silver doped hydroxyapatite coating with a polydimethylsiloxane layer was investigated by different complementary methods, such as the X-ray diffraction, Fourier Transform Infrared Spectroscopy, Scanning Electron Microscopy, and Glow Discharge Optical Emission Spectrometry. It indicated that some phenomenon could be characterized or found consistently by different methodologies. For example, the FT-IR analysis, in agreement with the XRD measurements, showed that the physical procedure used for the generation of the Ag:HAp-PDMS composite layer is useful for the formation of SiO_4^{4-} ions. The X-ray diffraction and Fourier Transform Infrared Spectroscopy measurements show that the hydroxyapatite doped with silver is in a crystalline form and some SiO_4^{4-} ions formation takes place at the surface and in the bulk of the new hydroxyapatite doped with silver/polydimethylsiloxane composite layer. Uniformly, the authors highlighted the potentiality of this emerging field of biomaterials related to its multiple functions, applications and syntheses, and characteristic methods.

Jen-Jie Chieh
Sharmila M. Mukhopadhyay
Yali Cui

Research Article

Physicochemical Analysis of the Polydimethylsiloxane Interlayer Influence on a Hydroxyapatite Doped with Silver Coating

C. L. Popa,^{1,2} A. Groza,³ P. Chapon,⁴ C. S. Ciobanu,¹ R. V. Ghita,¹
R. Trusca,⁵ M. Ganciu,³ and D. Predoi¹

¹National Institute for Materials Physics, P.O. Box MG 07, Magurele, 077125 Bucharest, Romania

²Faculty of Physics, University of Bucharest, 405 Atomistilor Street, P.O. Box MG1, 077125 Magurele, Romania

³National Institute for Laser, Plasma and Radiation Physics, 409 Atomistilor Street,
P.O. Box MG 36, Magurele, 077125 Bucharest, Romania

⁴Horiba Jobin Yvon S.A., 16-18 rue du Canal, 91165 Longjumeau Cedex, France

⁵S.C. METAV R&D S.A., 020011 Bucharest, Romania

Correspondence should be addressed to A. Groza; andreea@infim.ro and D. Predoi; dpredoi@gmail.com

Received 6 October 2014; Revised 15 December 2014; Accepted 15 December 2014

Academic Editor: Jen-Jie Chieh

Copyright © 2015 C. L. Popa et al. This is an open access article distributed under the Creative Commons Attribution License, which permits unrestricted use, distribution, and reproduction in any medium, provided the original work is properly cited.

We investigate by different complementary methods the processes occurring when a polydimethylsiloxane film is used as interlayer for a silver doped hydroxyapatite coating. The X-ray diffraction and Fourier Transform Infrared Spectroscopy measurements show that the hydroxyapatite doped with silver is in a crystalline form and some SiO_4^{4-} ions formation takes place at the surface and in the bulk of the new hydroxyapatite doped with silver/polydimethylsiloxane composite layer. The possibility of SiO_4^{4-} ions incorporation in the structure of silver doped hydroxyapatite by the mechanism of $\text{SiO}_4^{4-}/\text{PO}_4^{3-}$ ions substitution is analysed. The new formed silver doped hydroxyapatite/polydimethylsiloxane composite layer is compact, homogeneous, with no cracks as it was shown by Scanning Electron Microscopy and Glow Discharge Optical Emission Spectrometry.

1. Introduction

Hydroxyapatite (HAp, $\text{Ca}_{10}(\text{PO}_4)_6(\text{OH})_2$) is a biomaterial with a wide range of applications in medicine due to its biocompatibility, bioactivity, and osteoconductivity [1–4]. Hydroxyapatite has been used to fill a wide range of bony defects in orthopedic and maxillofacial surgeries and dentistry [5–8]. It has also been widely used as a coating for metallic prostheses to improve their biological properties [9–11].

From an antibacterial point of view, silver nanoparticles are widely used in medical devices and supplies such as wound dressings, scaffold, skin donation, recipient sites, and sterilized materials in hospitals, medical catheters, contraceptive devices, surgical instruments, bone prostheses, artificial teeth, and bone coating.

Recently, the use of inorganic antibacterial agents, like silver or copper, incorporated in the structure of hydroxyapatite has been shown to be of great interest in the fight against microbes [4]. Hydroxyapatite (HAp) has a very high cation exchange rate with silver ions. Even if at high concentration the silver can be toxic, in small concentrations it has a broad spectrum of antibacterial activity for a wide range of microorganisms like viruses, bacteria, or fungi [2]. Therefore the optimization of the Ag concentration in the HAp structure is critical to guarantee an optimum antibacterial effect without cytotoxicity.

The most common technique to incorporate Ag into HAp structure is via an ion exchange method, in which the Ca ions in HAp are replaced by Ag ions while dipping the HAp coatings into AgNO_3 for a period of time [2]. The limitation of this ion exchange method is that Ag will reside mostly on

the outer surface of the coating and will be quickly depleted *in vivo/in vitro* without long-term antibacterial effect.

In our previous studies [11] we presented preliminary results regarding the synthesis, characterization, and antibacterial properties of hydroxyapatite (HAp) and silver doped hydroxyapatite (Ag:HAp). The exact antibacterial action of silver nanoparticles (AgNPs) is not completely understood [12]. On the other hand, in the literature, studies on the preparation and characterization of the silver doped hydroxyapatite powders are almost absent. Antibacterial studies on the Ag:HAp nanopowders are also not presented. Recent studies [11, 13] have demonstrated that Ag:HAp nanoparticles prepared by coprecipitation method at 100°C show great promise as antibacterial agents against both gram-positive and gram-negative bacteria [13, 14].

Coatings of HAp have been deposited as amorphous layers by various techniques like plasma-spray technique, pulsed laser deposition, electrodeposition, sol-gel processing, and radio-frequency magnetron sputtering [15, 16]. Therefore, the coatings are thermally crystallized at elevated temperatures. During these thermal treatments, many cracks are formed due to a thermal expansion mismatch between the coating and the metal substrate, which severely reduces the bonding strength of the coating layer with the substrate [16].

In order to improve the delamination of HAp coatings different types of interlayers between the substrate and the HAp coating have been used as reinforcement agents. For example, SiO₂ layers are known for their own excellent compatibility with the living tissues and their high chemical inertness [17].

The polydimethylsiloxane (PDMS) is an elastomer with biocompatible properties and is frequently used as substrate for biological studies [6, 18]. The hydrophobic character of a PDMS layer, due to the methyl groups present on its surface, makes it suitable for nonadherent cell culture studies [19]. On the other hand, the oxidation of the PDMS surfaces can be achieved by different treatment methods [19], leading to the formation of hydrophilic SiO₂ surfaces which may favor the cells adhesion.

In this paper a method for generation of a Ag:HAp-PDMS composite layer by thermal evaporation of Ag:HAp nanoparticles and their deposition on the surface of a pure Si disk substrate previously covered with a PDMS layer is presented. The role of the polymer layer and the associated physicochemical processes that take place during the interaction of the hydroxyapatite vapours with the polymer are investigated by Scanning Electron Microscopy (SEM), X-ray diffraction (XRD), Fourier Transform Infrared Spectroscopy (FTIR), and Glow Discharge Optical Emission Spectroscopy (GDOES).

2. Experimental Section

2.1. Deposition of PDMS Polymer Layer on Commercially Pure Si Disks. The PDMS layers have been generated in atmospheric air pressure corona discharges starting from liquid precursors of vinyl terminated polydimethylsiloxane. The method and the experimental conditions used for the

deposition of thin PDMS layers (with an average thickness in the hundred nanometers range) on metallic substrates were presented in detail in [8, 9].

2.2. Silver Doped Hydroxyapatite (Ag:HAp) Nanoparticles. In order to synthesize the silver doped hydroxyapatite (Ag:HAp) precursors of calcium nitrate [Ca(NO₃)₂·4H₂O, Aldrich, USA], ammonium hydrogen phosphate ((NH₄)₂HPO₄; Wako Pure Chemical Industries Ltd.) and AgNO₃ (Alpha Aesare, Germany, 99.99% purity) were used. Controlled amounts of ammonium hydrogen phosphate and silver nitrate were dissolved in ethanol. After adding distilled water, the solution was stirred vigorously for 24 h at 40°C. In a separate container, a stoichiometric amount of calcium nitrate was dissolved in ethanol with vigorous stirring for 24 h at 40°C. The Ca-containing solution was added slowly to the P-containing solution and then aged at room temperature for 72 h and further at 40°C for 24 h. The composition ratios in the Ag:HAp ($x_{Ag} = 0$ and $x_{Ag} = 0.5$) sol were adjusted to have [Ca+Ag]/P as 1.67 [11, 47]. The obtained Ag:HAp nanopowders were treated at 800°C for 6 hours.

2.3. Deposition of Ag:HAp Solid Layers on Silicon Substrates Previously Coated with a PDMS Layer. Starting from an Ag:HAp ($x_{Ag} = 0.5$) powder (source material), by the thermal evaporation technique, an Ag:HAp solid layer has been deposited on a silicon substrate previously coated with a PDMS film. By this technique the Ag:HAp is evaporated in vacuum. The vapours travel directly to the substrate where they condense to a solid state. A HOCH VACUUM Dresden installation was used under environment conditions. The pressure in the deposition chamber was in the range of $8 \cdot 10^{-5}$ torr. The time range for a deposition cycle was around 120 min. The substrate was maintained at room temperature and at ground electrical potential. The Ag:HAp powder evaporation temperature was 1100°C. The tungsten boat temperature during the Ag:HAp powder evaporation is in the range of 1178–1205°C. The distance between substrate and boat is 5 cm.

The evaporation time measured during deposition is situated in the range of 20 sec for a maximum current intensity of $I = 75$ A and in the range of 15 sec for a maximum current $I = 80$ A. Taking into account the deposition characteristics, such as the total amount of HAp totally deposited (in mg) and the substrate-boat distance, the calculated evaporation velocities are $v_1 = 0.167$ mg/s or $v_1 \sim 8.3$ nm/s. The calculated thickness of a Ag:HAp ($x_{Ag} = 0.5$) layer deposited, in the experimental conditions presented above, on a silicon substrate is about 480 nm. In the presence of a PDMS film, the evaporated Ag:HAp nanoparticles that travel to the substrate condense, being trapped into the polymer bulk. Thus, an Ag:HAp-PDMS composite layer is generated.

2.4. Samples Characterizations. The morphology of the material was studied using a Quanta Inspect F Scanning Electron Microscope (SEM) equipped within gun beam in emission field, with wolfram filament and with a linear resolution of 5 nm. A part (10 mm) of a Si substrate with a diameter

of 20 mm was covered with a PDMS layer by the method presented above. Then an Ag:HAp layer was deposited by thermal evaporation technique on the entire surface of the Si substrate. The XRD patterns were recorded in the range of 25–55° using a Philips PW1830 diffractometer with filtered Cu K α radiation. The IR spectra of the Ag:HAp-PDMS composite layer formed on a silicon substrate have been obtained using an IR Perkin Elmer spectrometer equipped with a variable angle specular reflectance accessory. In order to perform depth profile studies of the Ag:HAp-PDMS composite layer we varied the angle of incidence light on the sample (equal but opposite to the angle of reflected light) from 30° to 60°. Here should be: Thus, function of the angle of incidence of the light on the sample the penetration depth of the light into the layer can be changed. For an angle of reflection of 30°, the geometrical position of the variable angle specular reflectance accessory inside the IR spectrometer allows the investigation of the composite layer/substrate interface. As the angle of reflection is increased up to 60° we can get information about molecules bonds arrangement in the composite layer bulk and as close as possible to the layer surface [9]. For certain spectral ranges, the peak fitting analyses were performed using procedures of Kolmas et al. [48]: (i) baseline correction, (ii) second derivative calculation and self-deconvolution assessment in order to determine the number and positions of the bands, and (iii) curve fittings with fixed peak positions using Lorentzian functions. In the previous studies Matsuhira and Rivas [49] and Gómez-Ordóñez and Rupérez [50] showed that second derivatives of FTIR spectra are generally used as an aid for wavenumber determination of weak absorption bands or to improve resolution of overlapped bands in the original spectra. To that end, in our studies, derivation including Savitzky-Golay algorithm with nine smoothing points was performed. The depth profile analysis of the Ag:HAp-PDMS composite layer formed on a silicon substrate was performed by Glow Discharge Optical Emission Spectroscopy (GDOES) using a GD Profiler 2 from Horiba/Jobin-Yvon. The selected operating conditions were as follows: 650 Pa for pressure and 35 W RF power, working in pulsed mode at 1 kHz pulsing frequency, and a duty cycle of 0.25. In this technique an area of 4 mm of the layer is sputtered by a pulsed RF Ar plasma. The sputtered atoms from the layer are then excited by inelastic collisions in the plasma and the emitted light is monitored in real time providing intensities of the elements of the investigated sample from the surface down to the substrate as a function of time.

An accurate conversion of sputtering time into sputtered depth is not straightforward because the sputtering rate is material dependent and varies during the elemental depth profiling measurement.

3. Results and Discussions

3.1. Scanning Electron Microscopy. In Figure 1(a) an image of the interface zone between the Ag:HAp-PDMS composite layer (the dark zone) and the Ag:HAp layer (the light zone) is presented. The polymer acts as a matrix layer for the Ag:HAp

coating. Also, it can be observed that both the Ag:HAp-PDMS composite layer and the Ag:HAp layer are compact and homogeneous with no cracks. In this way, by placing a polymer as interlayer on a material surface intended to be used as substrate for Ag:HAp coating, it is possible to improve its delamination property and thus the adherence of the Ag:HAP layer to the substrate. A high resolution SEM image of the Ag:HAp-PDMS composite layer is presented in Figure 1(b).

3.2. X-Ray Diffraction. XRD patterns of the Ag:HAp nanopowder and the Ag:HAp-PDMS composite layer are shown in Figure 2. All the observed diffraction maxima correspond to the hexagonal hydroxyapatite phase in good agreement with the standard ASTM data (JCPDS number 9-0432). The peaks associated with other phases are not observed. The absence of other phases can indicate an incorporation of SiO₂ into the Ag:HAp structure, by substitution of SiO₄⁴⁻ ions with PO₄³⁻ ions [51, 52]. The XRD characterizations of the Ag:HAp-PDMS composite layer are endorsed by the surface morphologies observed by SEM (Figure 1).

3.3. Fourier Transform Infrared Spectroscopy (FT-IR). In the following section we will present the FT-IR analysis of each component that constitutes the Ag:HAp-PDMS composite layer.

First, we investigated the polymer structure. The IR spectra and the IR bands assignment of the polymer generated from liquid precursors of vinyl terminated PDMS on a silicon substrate function of the angle of the incident light on the sample are presented in Figure 3 and Table 1.

A possible pathway of the polymerization mechanism of the vinyl terminated PDMS precursors involves the breaking of the double bond of the end group and thus the further linkage of the polymeric chains [9].

As we increase the angle of incident light on the sample up to 60°, it can be observed that the band from 1152 cm⁻¹ increases and the band from 860 cm⁻¹ decreases appearing like a shoulder on the new 880 cm⁻¹ band. The increase of the intensities of the 1152 cm⁻¹ and 880 cm⁻¹ IR bands accompanied by the decrease of 860 cm⁻¹ IR band can be understood knowing that, during the polymerization process of PDMS in negative corona discharge, the formation of the new Si-O bonds due to the injection of the negative ions in the liquid precursor bulk is associated with the diminishing of Si-CH₃ bonds [9, 53]. Thus, in the polymer layer bulk, mainly at the polymer layer surface SiO₂ structures [9] can be generated.

In the same time, in [9] it was mentioned that during the polymerization process of PDMS in negative corona discharge in air at atmospheric pressure some water molecules can be injected into the layer bulk. They can be decomposed in OH groups due to the high electric fields associated with corona discharges [9, 54].

Therefore, the band from 1650 cm⁻¹ present in the IR spectrum of the PDMS polymer, assigned to partly hydrated silica and to the stretching vibrations of adsorbed OH group

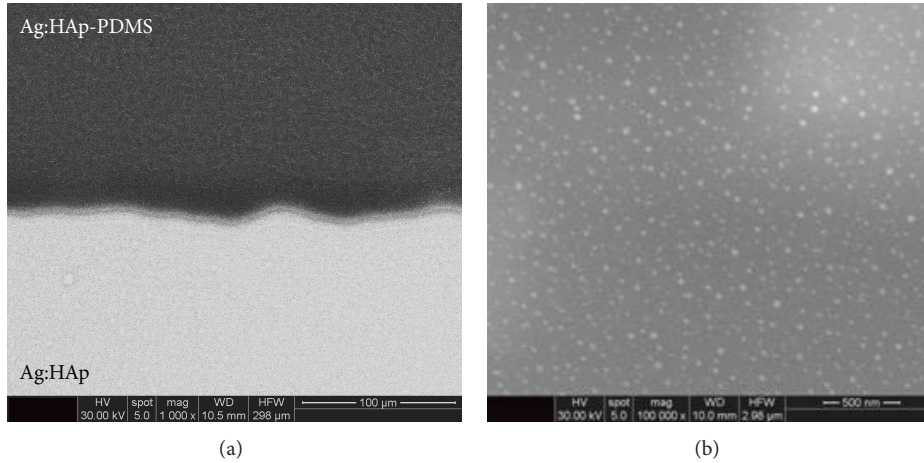


FIGURE 1: SEM image of (a) interface between the Ag:HAp-PDMS composite layer and the Ag:HAp layer and (b) Ag:HAp-PDMS composite layer.

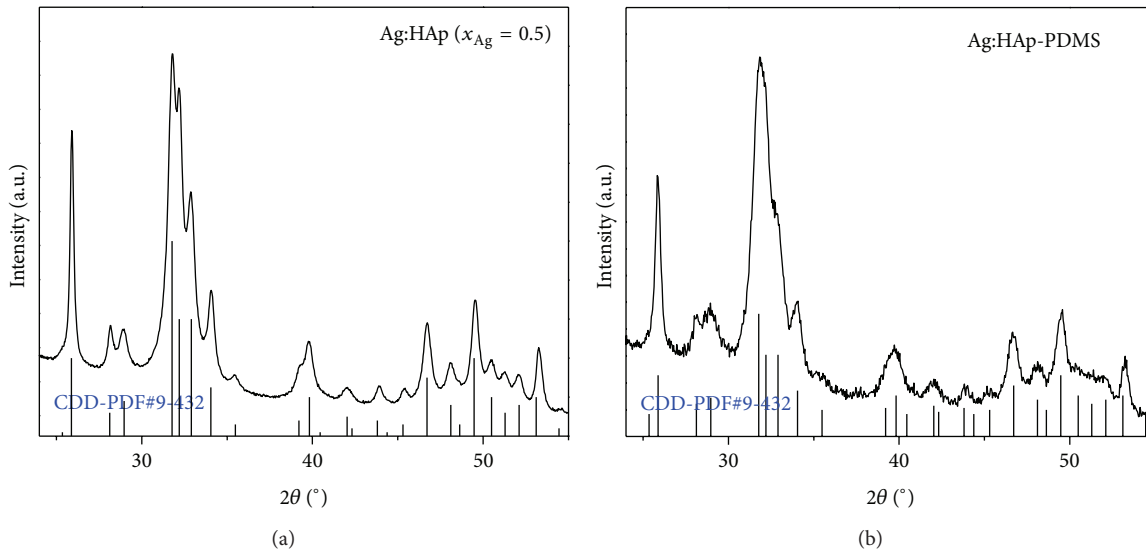


FIGURE 2: XRD diffraction patterns of the Ag:HAp nanopowder (a) and the Ag:HAp-PDMS composite layer (b).

respectively (Si-OH) [46] indicates the formation of Si-OH group [55]. The existence of the Si-OH in the PDMS layer is also suggested by the formation of the new Si-O bonds by the possible hydroxylation $\text{Si-OH} + \text{Si-OH} = \text{Si-O-Si} + \text{H}_2\text{O}$ reaction [55].

Second, we performed FT-IR analysis on the Ag:HAp-PDMS composite layer. The IR spectra are presented in Figure 4. Furthermore, the IR bands assignment is highlighted in Table 1.

The IR band from 1152 cm^{-1} , Figure 3, is shifted to 1140 cm^{-1} , Figure 4, being visible only in the spectrum obtained for an angle of incident light on the sample of 60° . The shift of this band and its absence in the IR spectra obtained at $r = 30^\circ$, 40° , and 50° , respectively, Figure 4, can indicate the rearrangements of Si and O atoms in the SiO_2 structures when an Ag:HAp layer is deposited, by the thermal

evaporation technique, on a substrate previously coated with a PDMS film.

The formation of SiO_4^{4-} groups was evidenced by the 490 and 695 cm^{-1} IR bands (Figure 4 and Table 1).

The 1004 and 1071 cm^{-1} IR bands (Figure 3 and Table 1) seem to be shifted to 995 and 1066 cm^{-1} (Figure 4), respectively, possibly due to the overlapping of IR bands characteristics to PDMS and Ag:HAp.

In comparison with the IR spectrum of the PDMS layer (Figure 3), in the IR spectrum of Ag:HAp-PDMS composite layer (Figure 4) we can observe a broad band in $3000\text{--}3600\text{ cm}^{-1}$ region due to the adsorbed H_2O from the Ag:HAp structure, OH or Si-OH groups [36, 46], its intensity being diminished as we approach the surface of the Ag:HAp-PDMS composite layer (Figure 4). The diminishing of the band intensity as close as possible to the surface layer can be

TABLE 1: FT-IR bands associated with the functional groups present in the structure of Ag:HAP-PDMS composite layer.

Wavenumber (cm^{-1})	IR bands assignment	
	PDMS layer	Ag:HAP-PDMS layer
490	—	SiO_4^{4-} [20–23], Figure 4
498, 512, 543, 550	—	SiO_4^{4-} [24, 25], Figure 5(a)
562, 590, 602, 611	—	P-O bending vibrations in PO_4^{3-} tetrahedron in crystalline HAP [20–23, 26–35], Figure 5(a)
620	$\text{Si}(\text{CH}_3)_2$ asymmetrical stretching vibration [36], Figure 3	—
695	—	Crystallinity of SiO_2 type materials [37], Figure 4
780	—	Si-O-P vibration [38], Figure 5(c)
784	Si-C stretching vibration [36], Figure 3	—
814, 816, 817.5	—	Si-O-Si bonds [27, 28], Figure 5(c)
828	—	Si-O-Ag [39, 40], Figure 5(d)
860	Si- CH_3 rocking vibration [36], Figure 3	—
862	—	Si-O, Si-C vibrations [28], Figure 5(e)
870	—	CO_3^{2-} vibrations [20, 30, 41], Figure 5(e)
877	—	HPO_4^{2-} ions [32, 34, 42, 43], Figure 5(e)
889	Si-O bending vibration [37, 44], Figure 3	—
925, 945, 975	—	P-O vibrations in PO_4^{3-} group [20–23, 26–30, 45], Figure 5(b)
1004, 1071	Si-O-Si vibrations [36], Figure 3	—
1000, 1044, 1067, 1085	—	PO_4^{3-} [20–23, 26–35], Figure 5(b)
1140	—	Si-O vibrations [9, 37, 44], Figure 4
1152	Si-O vibrations [9, 37, 44], Figure 3	—
1254, 1400	CH_3 vibrations in $\text{Si}=\text{CH}_3$ group [36], Figure 3	CH_3 vibrations in $\text{Si}=\text{CH}_3$ group [36], Figure 4
1650	H_2O , OH, Si-OH [46], Figure 3	H_2O , OH, Si-OH [46], Figure 4
2912, 2964	C-H vibrations [36], Figure 3	—

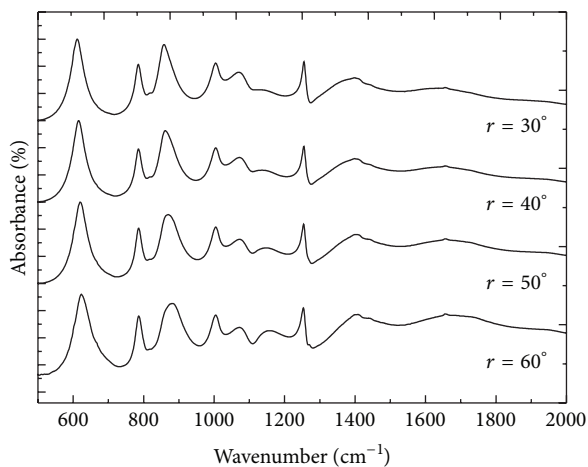


FIGURE 3: IR spectra of a polymer generated from a vinyl terminated polydimethylsiloxane liquid precursors on a silicon substrate for different reflection angles.

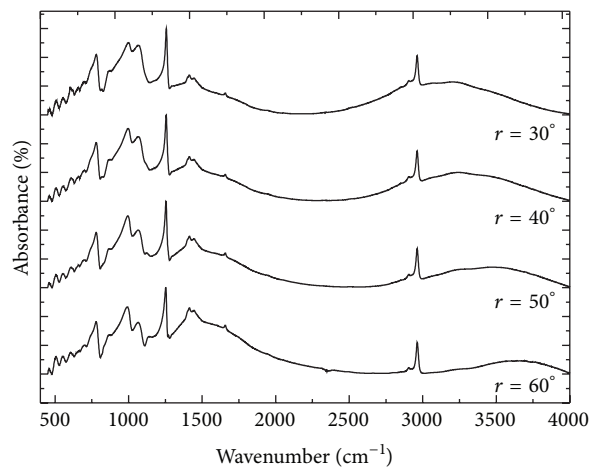


FIGURE 4: FTIR spectra of the Ag:HAP-PDMS composite layer function of the angle of the incident light on the sample.

explained if we consider that during the deposition process the Ag:HAp evaporated molecules that travel to the substrate diffuse into the PDMS layer bulk, heating it. During the condensation of the Ag:HAp molecules on the substrate, we suppose that several processes, such as the water evaporation and the generation of some new bonds in the bulk of the Ag:HAp-PDMS composite layer, are taking place.

The IR band from 1650 cm^{-1} observed in the spectrum of the PDMS layer (Figure 3) is still present in the spectrum of the Ag:HAp-PDMS composite layer (Figure 4). In some previous studies on polydimethylsiloxane/HAp composites [38], it was shown that an IR band at around 1650 cm^{-1} originates from the deformational vibrations of hydroxyapatite OH groups, which form hydrogen bonds with the silicate OH groups.

According to previous studies [27, 56], the IR spectral regions specific to chemical bonds present in Si based compounds (mainly Si-O) and HAp (P-O bonds), respectively, are almost similar. Thus, we have performed a peak fitting analysis of the IR spectrum of the Ag:HAp-PDMS composite layer for a proper identification of the processes that take place during its formation (Figure 5). It was previously shown [24, 25, 38, 57, 58] that the overlapping of Si-O and P-O bands could indicate the incorporation of Si based structures in the Ag:HAp.

In Figures 5(a) and 5(b) all the IR bands specific to P-O vibrations in PO_4^{3-} ions and those specific to Si-O bonds in SiO_4^{4-} ions which are also summarized in Table 1 can be observed. The appearance of these Si-O peaks might indicate a partial loss of phosphate groups and/or of the symmetry at the site caused by substitution of silicate species in Si-HAp [24, 25]. At the same time, the IR band from 1000 cm^{-1} (Figure 5(b)) and 925 cm^{-1} highlights the incorporation of Si into the HAp structure [57, 58]. Jovanovic et al. [38] suggested that the overlap of the Si-O and P-O bands might indicate a substitution of PO_4^{3-} with SiO_4^{4-} .

The results of the peak fitting analysis presented in Figure 5(c) reveal the presence of Si-O-Si bonds specific to inorganic silica moiety [29], also asserting their presence in the Ag:HAp-PDMS composite layer. The Si-OH groups are present in the Ag:HAp-PDMS composite layer (Figure 4) due to the formation of the interlinked bonds of Si-O-Ag or Si-O-P type, Figure 5(d). According to [39, 40] a double displacement reaction, $\text{Si-O-H} + \text{Ag}^+ = \text{Si-O-Ag} + \text{H}^+$, would be expected to have occurred, causing the appearance of Si-O-Ag vibration bands in the FT-IR spectrum of Ag:HAp-PDMS composite layer. Likewise, the Si-O-P bonds can be formed due to the interaction of the silicate molecules with OH groups from the structure of hydroxyapatite [38].

In Figure 5(e) the results of the peak fitting analysis obtained in the $850\text{--}890\text{ cm}^{-1}$ spectral region where the overlapping of the Si-O, Si-C, HPO_4^{2-} , and CO_3^{2-} characteristic bands has previously been explained [20, 25, 30, 32, 34, 35, 41–43] are presented.

The peaks associated with all the functional groups present in the IR spectra of Ag:HAp-PDMS composite layer are summarized in Table 1.

3.4. Glow Discharge Optical Emission Spectrometry (GDOES). In Figure 6(a) the depth profile curves of the Si, O, C, and H atoms in the bulk and at the surface of the PDMS layer are presented.

The depth profiles of the P, Ca, Ag, and O atoms in a Ag:HAp layer were presented elsewhere [20].

In Figure 6(b) it can be observed that the depth profile curves of all the elements identified in the bulk of the Ag:HAp-PDMS composite layer have similar behaviour. There is no sharp delimitation between the Ca, Ag, P, O, and H depth profile curves specific to a Ag:HAp layer and those of Si, O, C, and H atoms present in the PDMS layer. This could result from different causes: roughness of the interface (as the GD averages the signals over the entire erosion zone), flatness of the crater bottom, or formation of a composite material. The operating conditions selected for the present analysis provide a flat crater bottom, while for other similar samples [20] the interface did not indicate any roughness. Therefore, the GD results correlate the observations made and tend to indicate that during the deposition process there are some interactions between the Ag:HAp particles and the polymer and thus the formation of a composite material.

Compared to Figure 6(a), in Figure 6(b), the intensity of the Si depth profile decreases and a broadening of its shape can be also observed. The redistribution of Si atoms in the bulk of the new composite layer emphasizes the possibility of Si involvement in the formation of new Si-O, Si-O-Ag, and Si-O-P chemical bonds. The Si depth profile curves reach a plateau only after the Ca profile curve drops down.

This observation is an indication of silicon atoms involvement not only in the silicon oxide structures, Si-O-Ag or Si-O-P bonds formation, but also in the structure of the Ag:HAp-PDMS composite layer, in accordance with FT-IR investigations. A plateau in a profile curve followed by an increase is an indication of substrate interface. This kind of behaviour of a certain depth profile curve when all the other depth profile curves decrease is generally observed when an element contained in the investigated layer is also present in the substrate material [9, 59].

In the current study we have presented for the first time the formation of an Ag:HAp-PDMS composite layer by deposition of Ag:HAp nanoparticles on a substrate previously coated with a PDMS layer via a simple and reproducible method. The studies of the Ag:HAp-PDMS composite layer are captivating, mainly because of their interesting physico-chemical properties and unique structure, which make them attractive for many applications. Due to the presence of Ag in the layer structure, this compound presents a great interest in future biological and biochemical studies. In previous studies [20], it was shown that Ag:HAp thin films have antimicrobial properties against *Escherichia coli* and *Staphylococcus aureus* bacteria. According to Shevchenko et al. [40], formation of Si-O-M linkages can be indicated by the shift of Si asymmetric valence band to the field of lower frequencies. On the other hand, the GDOES analysis showed that during the deposition process there are some interactions between Ag:HAp and the polymer thus forming a new composite material. These results are supported by the presence of vibrational bands associated with Si-O-Ag bonds in the obtained IR spectrum

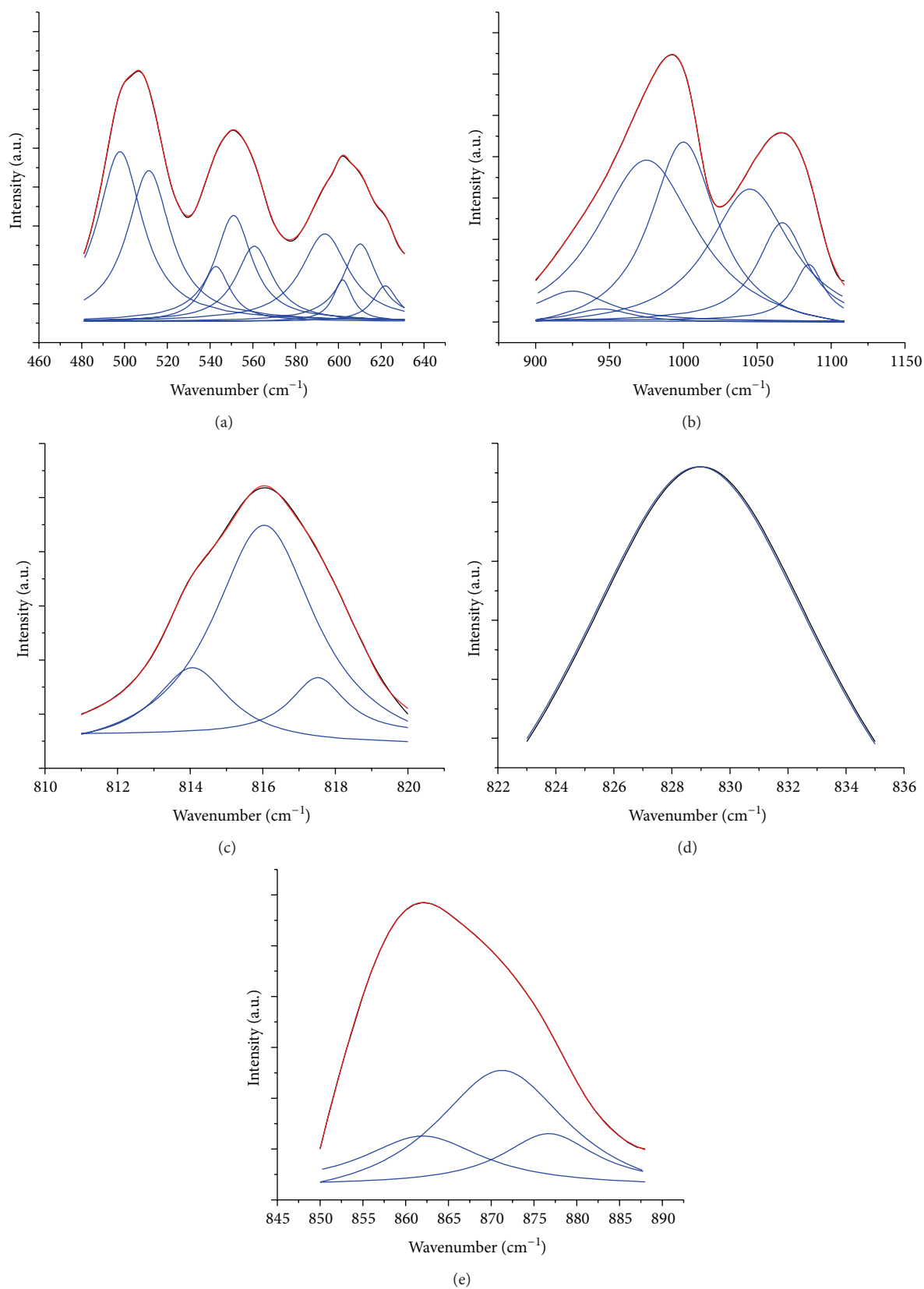


FIGURE 5: FT-IR deconvoluted spectra of the Ag:HAp-PDMS composite layer in the spectral regions: (a) 450–650 cm⁻¹, (b) 900–1200 cm⁻¹, (c) 810–820 cm⁻¹, (d) 822–835 cm⁻¹, and (e) 850–890 cm⁻¹, for an incident angle of the light on the sample of 60°. The experimental curve is plotted in red and calculated theoretical bands are in blue.

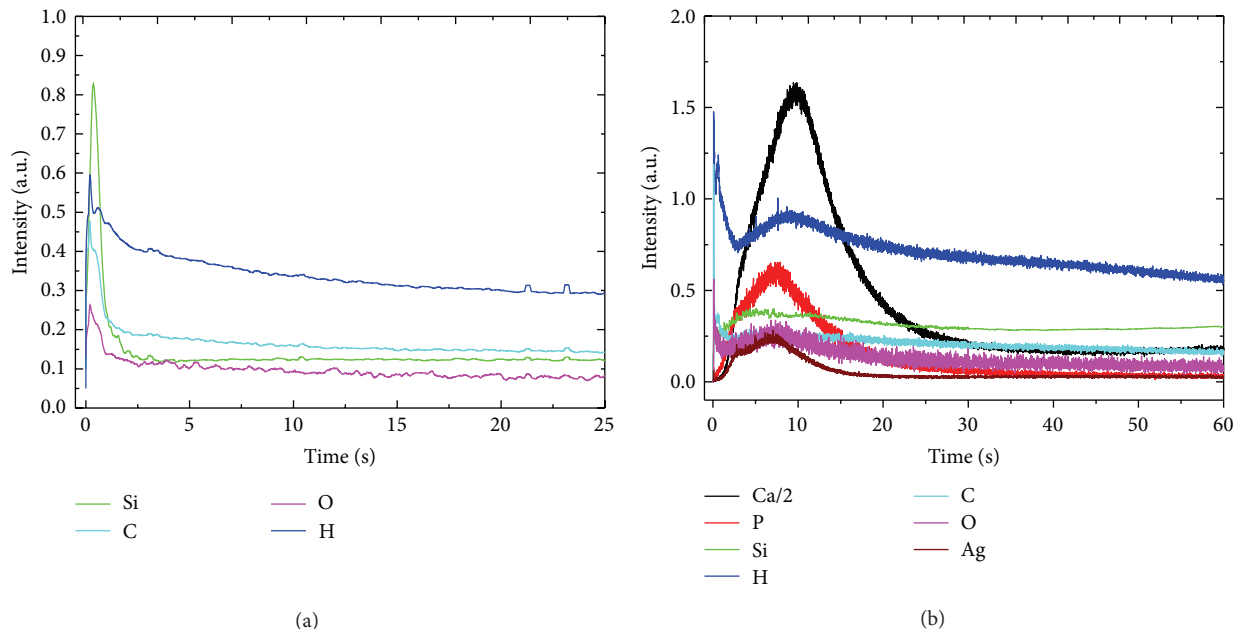


FIGURE 6: GDOES spectra of (a) PDMS layer and (b) Ag:HAp-PDMS composite layer, generated on a Si substrate.

(Figure 5(d)) which ascertain the presence of Ag in the structure of the Ag:HAp-PDMS composite layer [40]. Moreover, this study develops a novel and facile method to produce composites based on Ag (Ag:HAp-PDMS composite layer) which can be used for large-scale applications.

4. Conclusions

In this paper a method for the deposition of a Ag:HAp coating on a substrate previously covered with a PDMS layer is presented. As the SEM investigations showed, the PDMS layer acts as a matrix in which the Ag:Hap is incorporated. In this way, a Ag:HAp-PDMS composite layer is formed. The XRD measurements showed that the crystalline form of the Ag-HAP is maintained in the composite layer.

By FT-IR and GDOES spectral techniques we investigated the physicochemical processes that take place during the interaction of Ag:HAp with the PDMS layer. The FT-IR analysis, in agreement with the XRD measurements, showed that the physical procedure used for the generation of the Ag:HAp-PDMS composite layer is useful for the formation of SiO_4^{4-} ions. On the other hand, the SiO_4^{4-} ions can be incorporated into the Ag:HAp structures substituting the PO_4^{3-} ions from the structure of Ag:HAp. We suppose that after the condensation of the Ag:HAp on the substrate, due to the heating of the SiO_2 network present in the polymer bulk, the SiO_4^{4-} ions are generated.

The GDOES depth profiling curves of the Ag:HAp-PDMS composite layer indicate that its composition is homogeneous which can be explained by the formation of the Si-O-Ag and Si-O-P bonds, respectively, and the Si involvement in Ag:HAp structure.

Conflict of Interests

The authors declare that there is no conflict of interests regarding the publication of this paper. The authors also declare that they do not have any other conflicts to declare.

Acknowledgments

The financial and encouragement support provided by the Ministry of Education of Romania, Project nos. PN-II-ID-PCE-2011-3-0958 and PT-PCCA-2011-3.1-1136, is acknowledged.

References

- [1] A. Dudek and L. Adamczyk, "Properties of hydroxyapatite layers used for implant coatings," *Optica Applicata*, vol. 43, pp. 143–151, 2013.
- [2] C. S. Ciobanu, E. Andronescu, and D. Predoi, "BET and XRD studies on the hydroxyapatite and europium doped hydroxyapatite," *Journal of Optoelectronics and Advanced Materials*, vol. 13, no. 7, pp. 821–824, 2011.
- [3] D.-H. Kim, Y.-M. Kong, S.-H. Lee et al., "Composition and crystallization of hydroxyapatite coating layer formed by electron beam deposition," *Journal of the American Ceramic Society*, vol. 86, no. 1, pp. 186–188, 2003.
- [4] K. Mediaswanti, C. Wen, E. P. Ivanova, C. C. Berndt, and J. Wang, *Titanium alloys—Advances in Properties Control*, Edited by J. Sieniawski and W. Ziaja, InTech, 2013.
- [5] J. C. Selby and M. A. Shannon, "A method to fabricate mesoscopic freestanding polydimethylsiloxane membranes used to probe the rheology of an epithelial sheet," *Journal of Biochemical and Biophysical Methods*, vol. 70, p. 932, 2008.

- [6] D. Fuard, T. Tzvetkova-Chevolleau, S. Decossas, P. Tracqui, and P. Schiavone, "Optimization of poly-di-methyl-siloxane (PDMS) substrates for studying cellular adhesion and motility," *Microelectronic Engineering*, vol. 85, no. 5-6, pp. 1289–1293, 2008.
- [7] M. Calasans-Maia, E. Sales, J. M. Granjeiro, R. T. Lopes, and I. Lima, "Bone implant interface investigation by synchrotron radiation X-ray microfluorescence," in *Proceedings of the 20th International Congress: X-ray Optics and Microanalysis*, vol. 1221 of *AIP Conference Proceedings*, pp. 160–163, Karlsruhe, Germany, 2009.
- [8] A. Groza, A. Surmeian, M. Ganciu, and I. I. Popescu, "Infrared spectral investigation of the linseed oil polymerization in a corona discharge in air at atmospheric pressure," *Europhysics Letters*, vol. 68, no. 5, pp. 652–657, 2004.
- [9] A. Groza, A. Surmeian, C. Diplasu et al., "Physico-chemical processes occurring during polymerization of liquid polydimethyl-siloxane films on metal substrates under atmospheric pressure air corona discharges," *Surface and Coatings Technology*, vol. 212, pp. 145–151, 2012.
- [10] C. S. Ciobanu, S. L. Iconaru, I. Pasuk et al., "Structural properties of silver doped hydroxyapatite and their biocompatibility," *Materials Science and Engineering C*, vol. 33, no. 3, pp. 1395–1402, 2013.
- [11] C. S. Ciobanu, F. Massuyeau, L. V. Constantin, and D. Predoi, "Structural and physical properties of antibacterial Ag-doped nano-hydroxyapatite synthesized at 100°C," *Nanoscale Research Letters*, vol. 6, article 613, 2011.
- [12] X. Li, S. Li, M. Zhang, W. Zhang, and C. Li, "Evaluations of antibacterial activity and cytotoxicity on Ag nanoparticles," *Rare Metal Materials and Engineering*, vol. 40, no. 2, pp. 209–214, 2011.
- [13] C. S. Ciobanu, S. L. Iconaru, P. le Coustumer, L. V. Constantin, and D. Predoi, "Antibacterial activity of silver-doped hydroxyapatite nanoparticles against gram-positive and gram-negative bacteria," *Nanoscale Research Letters*, vol. 7, article 324, 2012.
- [14] C. S. Ciobanu, S. L. Iconaru, M. C. Chifriuc, A. Costescu, P. Le Coustumer, and D. Predoi, "Synthesis and antimicrobial activity of silver-doped hydroxyapatite nanoparticles," *BioMed Research International*, vol. 2013, Article ID 916218, 10 pages, 2013.
- [15] A. Dudek and L. Adamczyk, "Properties of hydroxyapatite layers used for implant coatings," *Optica Applicata*, vol. 43, no. 1, pp. 143–151, 2013.
- [16] D.-H. Kim, Y.-M. Kong, S.-H. Lee et al., "Composition and crystallization of hydroxyapatite coating layer formed by electron beam deposition," *Journal of the American Ceramic Society*, vol. 86, no. 1, pp. 186–188, 2003.
- [17] K. Mediaswanti, C. Wen, E. P. Ivanova, C. C. Berndt, and J. Wang, "Sputtered hydroxyapatite nanocoatings on novel titanium alloys for biomedical applications," in *Titanium Alloys-Advances in Properties Control*, J. Sieniawski and W. Ziaja, Eds., pp. 21–44, InTech, Rijeka, Croatia, 2013.
- [18] J. C. Selby, M. A. Shannon, and J. Biochem, "A method to fabricate mesoscopic freestanding polydimethylsiloxane membranes used to probe the rheology of an epithelial sheet," *Journal of Biochemical and Biophysical Methods*, vol. 70, no. 6, pp. 932–944, 2008.
- [19] P. Ingram, M. Im, S. McDermott, M. Wicha, and E. Yoon, "Spheroid cell culture on PDMS hydrophobic surfaces and integration into microfluidic devices," in *Proceedings of the International Conference on Miniaturized Systems for Chemistry and Life Sciences (MicroTAS '11)*, J. Landers, Ed., pp. 1539–1541, Seattle, Wash, USA, 2011.
- [20] S. L. Iconaru, P. Chapon, P. le Coustumer, and D. Predoi, "Antimicrobial activity of thin solid films of silver doped hydroxyapatite prepared by sol-gel method," *The Scientific World Journal*, vol. 2014, Article ID 165351, 8 pages, 2014.
- [21] A. Costescu, I. Pasuk, F. Ungureanu et al., "Physico-chemical properties of nano-sized hexagonal hydroxyapatite powder synthesized by sol-gel," *Digest Journal of Nanomaterials and Biostructures*, vol. 5, no. 4, pp. 989–1000, 2010.
- [22] A. Aminian, M. Solati-Hashjin, A. Samadikuchaksaraei et al., "Synthesis of silicon-substituted hydroxyapatite by a hydrothermal method with two different phosphorous sources," *Ceramics International*, vol. 37, no. 4, pp. 1219–1229, 2011.
- [23] K. A. Hing, P. A. Revell, N. Smith, and T. Buckland, "Effect of silicon level on rate, quality and progression of bone healing within silicate-substituted porous hydroxyapatite scaffolds," *Biomaterials*, vol. 27, no. 29, pp. 5014–5026, 2006.
- [24] A. Balamurugan, A. H. S. Rebelo, A. F. Lemos, J. H. G. Rocha, J. M. G. Ventura, and J. M. F. Ferreira, "Suitability evaluation of sol-gel derived Si-substituted hydroxyapatite for dental and maxillofacial applications through *in vitro* osteoblasts response," *Dental Materials*, vol. 24, no. 10, pp. 1374–1380, 2008.
- [25] N. Higon, M. V. Cabanas, J. Pena, and M. Vallet-Regi, "Dip coated silicon-substituted hydroxyapatite films," *Acta Biomaterialia*, vol. 2, no. 5, pp. 567–574, 2006.
- [26] C. M. Botelho, M. A. Lopes, I. R. Gibson, S. M. Best, and J. D. Santos, "Structural analysis of Si-substituted hydroxyapatite: zeta potential and X-ray photoelectron spectroscopy," *Journal of Materials Science: Materials in Medicine*, vol. 13, no. 12, pp. 1123–1127, 2002.
- [27] T. Liu, D. Lai, X. Feng, H. Zhu, and J. Chen, "Synthesis and characterization of a novel mesoporous bioactive glass/hydroxyapatite nanocomposite," *Materials Letters*, vol. 92, pp. 444–447, 2013.
- [28] A. Hilonga, J. K. Kim, P. B. Sarawade, and H. T. Kim, "Influence of annealing conditions on the properties of reinforced silver-embedded silica matrix from the cheap silica source," *Applied Surface Science*, vol. 256, no. 9, pp. 2849–2855, 2010.
- [29] S. Zhang, F. Xu, Y. Wang, W. Zhang, X. Peng, and F. Pepe, "Silica modified calcium alginate-xanthan gum hybrid bead composites for the removal and recovery of Pb(II) from aqueous solution," *Chemical Engineering Journal*, vol. 234, pp. 33–42, 2013.
- [30] S. L. Iconaru, M. Motelica-Heino, and D. Predoi, "Study on europium-doped hydroxyapatite nanoparticles by fourier transform infrared spectroscopy and their antimicrobial properties," *Journal of Spectroscopy*, vol. 2013, Article ID 284285, 10 pages, 2013.
- [31] Y. Leung and M. A. Walters, "Second derivative infrared spectra of hydroxyapatite," *Spectrochimica Acta*, vol. 46, pp. 1453–1459, 1990.
- [32] M. Markovik, B. O. Fowler, and M. S. Tung, "Preparation and comprehensive characterization of a calcium hydroxyapatite reference material," *Journal of research of the National Institute of Standards and Technology*, vol. 109, p. 553, 2004.
- [33] Y. Wang, X. Zhang, J. Yan, Y. Xiao, and M. Lang, "Surface modification of hydroxyapatite with poly(methyl methacrylate) via surface-initiated ATRP," *Applied Surface Science*, vol. 257, pp. 6233–6238, 2011.
- [34] S. Agathopoulos, D. U. Tulyaganov, J. M. G. Ventura, S. Kannan, M. A. Karakassides, and J. M. F. Ferreira, "Formation of

- hydroxyapatite onto glasses of the CaO-MgO-SiO₂ system with B₂O₃, Na₂O, CaF₂ and P₂O₅ additives," *Biomaterials*, vol. 27, no. 9, pp. 1832–1840, 2006.
- [35] L. M. Miller, V. Vairavamurthy, M. R. Chance et al., "In situ analysis of mineral content and crystallinity in bone using infrared micro-spectroscopy of the ν_4 PO₄³⁻ vibration," *Biochimica et Biophysica Acta*, vol. 1527, no. 1-2, pp. 11–19, 2001.
- [36] G. Socrates, *Infrared Characteristic Group Frequencies*, John Wiley & Sons, Chichester, UK, 2nd edition, 1994.
- [37] B. J. Saikia, G. Parthasarathy, and N. C. Sarmah, "Fourier transform infrared spectroscopic estimation of crystallinity in SiO₂ based rocks," *Bulletin of Materials Science*, vol. 31, no. 5, pp. 775–779, 2008.
- [38] J. Jovanovic, B. Adnadjevic, M. Kicanovic, and D. Uskokovic, "The influence of hydroxyapatite modification on the cross-linking of polydimethylsiloxane/HAp composites," *Colloids and Surfaces B: Biointerfaces*, vol. 39, no. 4, pp. 181–186, 2004.
- [39] L. Armelao, R. Bertoncello, and M. De Dominicis, "Silver nanocluster formation in silica coatings by the sol-gel route," *Advanced Materials*, vol. 9, no. 9, pp. 736–741, 1997.
- [40] G. P. Shevchenko, S. V. Vashchanka, Y. V. Bokshits, and S. K. Rakhmanov, "On the nature of the processes occurring in silver doped SiO₂ films under heat treatment," *Journal of Sol-Gel Science and Technology*, vol. 45, no. 2, pp. 143–149, 2008.
- [41] S. Hayakawa, T. Kanaya, K. Tsuru et al., "Heterogeneous structure and in vitro degradation behavior of wet-chemically derived nanocrystalline silicon-containing hydroxyapatite particles," *Acta Biomaterialia*, vol. 9, no. 1, pp. 4856–4867, 2013.
- [42] C. S. Ciobanu, E. Andronescu, B. S. Vasile, C. M. Valsangiacom, R. V. Ghita, and D. Predoi, "Looking for new synthesis of hydroxyapatite doped with europium," *Optoelectronics and Advanced Materials, Rapid Communications*, vol. 4, no. 10, pp. 1515–1519, 2010.
- [43] A. V. Lluch, G. G. Ferrer, and M. M. Pradas, "Biomimetic apatite coating on P(EMA-co-HEA)/SiO₂ hybrid nanocomposites," *Polymer*, vol. 50, no. 13, pp. 2874–2884, 2009.
- [44] L. J. Bellamy, *The Infrared Spectra of Complex Molecules*, John Wiley & Sons, New York, NY, USA, 3rd edition, 1975.
- [45] L. Duta, F. N. Oktar, G. E. Stan et al., "Novel doped hydroxyapatite thin films obtained by pulsed laser deposition," *Applied Surface Science*, vol. 265, pp. 41–49, 2013.
- [46] L. G. Benning, V. R. Phoenix, N. Yee, and M. J. Tobin, "Molecular characterization of cyanobacterial silicification using synchrotron infrared micro-spectroscopy," *Geochimica et Cosmochimica Acta*, vol. 68, no. 4, pp. 729–741, 2004.
- [47] C. S. Ciobanu, F. Massuyeau, E. Andronescu, M. S. Stan, A. Dinischiotu, and D. Predoi, "Biocompatibility study of europium doped crystalline hydroxyapatite bioceramics," *Digest Journal of Nanomaterials and Biostructures*, vol. 6, no. 4, pp. 1639–1647, 2011.
- [48] J. Kolmas, A. Jaklewicz, A. Zima et al., "Incorporation of carbonate and magnesium ions into synthetic hydroxyapatite: the effect on physicochemical properties," *Journal of Molecular Structure*, vol. 987, no. 1–3, pp. 40–50, 2011.
- [49] B. Matsuhiro and P. Rivas, "Second-derivative Fourier transform infrared spectra of seaweed galactans," *Journal of Applied Phycology*, vol. 5, no. 1, pp. 45–51, 1993.
- [50] E. Gómez-Ordóñez and P. Rupérez, "FTIR-ATR spectroscopy as a tool for polysaccharide identification in edible brown and red seaweeds," *Food Hydrocolloids*, vol. 25, no. 6, pp. 1514–1520, 2011.
- [51] C. L. Popa, C. S. Ciobanu, S. L. Iconaru et al., "Systematic investigation and *in vitro* biocompatibility studies on mesoporous europium doped hydroxyapatite," *Central European Journal of Chemistry*, vol. 12, no. 10, pp. 1032–1046, 2014.
- [52] R. V. Ghita, S. L. Iconaru, C. L. Popa et al., "Tetraethyl orthosilicate coated hydroxyapatite powders for lead ions removal from aqueous solutions," *Journal of Nanomaterials*, vol. 2014, Article ID 176426, 7 pages, 2014.
- [53] A. Groza, A. Surmeian, M. Ganciu, and I. I. Popescu, "Infrared spectral investigation of organosilicon compounds under corona charge injection in air at atmospheric pressure," *Journal of Optoelectronics and Advanced Materials*, vol. 7, no. 5, pp. 2545–2548, 2005.
- [54] M. Goldman and A. Goldman, "Corona discharges," in *Gaseous Electronics*, M. N. Hirsh and H. J. Oskam, Eds., vol. 1, pp. 219–290, Academic Press, New York, NY, USA, 1978.
- [55] K.-S. Koh, J. Chin, J. Chia, and C.-L. Chiang, "Quantitative studies on PDMS-PDMS interface bonding with piranha solution and its swelling effect," *Micromachines*, vol. 3, no. 2, pp. 427–441, 2012.
- [56] B.-D. Hahn, J.-M. Lee, D.-S. Park et al., "Aerosol deposition of silicon-substituted hydroxyapatite coatings for biomedical applications," *Thin Solid Films*, vol. 518, no. 8, pp. 2194–2199, 2010.
- [57] D. Marchat, M. Zymelka, C. Coelho et al., "Accurate characterization of pure silicon-substituted hydroxyapatite powders synthesized by a new precipitation route," *Acta Biomaterialia*, vol. 9, no. 6, pp. 6992–7004, 2013.
- [58] H. Aguiar, J. Serra, P. González, and B. León, "Structural study of sol-gel silicate glasses by IR and Raman spectroscopies," *Journal of Non-Crystalline Solids*, vol. 355, no. 8, pp. 475–480, 2009.
- [59] K. Shimizu, H. Habazaki, P. Skeldon, and G. E. Thompson, "Radiofrequency GDOES: a powerful technique for depth profiling analysis of thin films," *Surface and Interface Analysis*, vol. 35, no. 7, pp. 564–574, 2003.

Research Article

Comparison of the Effect of Sol-Gel and Coprecipitation Routes on the Properties and Behavior of Nanocomposite Chitosan-Bioactive Glass Membranes for Bone Tissue Engineering

Elke M. F. Lemos,¹ Sandhra M. Carvalho,¹ Patrícia S. O. Patrício,²
Claudio L. Donnici,³ and Marivalda M. Pereira¹

¹NDBio Research Group, Department of Metallurgical and Materials Engineering, Universidade Federal de Minas Gerais, 253 31270-901 Belo Horizonte, MG, Brazil

²Department of Chemistry, Centro Federal de Educação Tecnológica de Minas Gerais, 30 421-169 Belo Horizonte, MG, Brazil

³Department of Chemistry, Universidade Federal de Minas Gerais, 253 31270-901 Belo Horizonte, MG, Brazil

Correspondence should be addressed to Marivalda M. Pereira; mpereira@demet.ufmg.br

Received 13 April 2014; Revised 16 August 2014; Accepted 25 September 2014

Academic Editor: Sharmila M. Mukhopadhyay

Copyright © 2015 Elke M. F. Lemos et al. This is an open access article distributed under the Creative Commons Attribution License, which permits unrestricted use, distribution, and reproduction in any medium, provided the original work is properly cited.

Recent studies in tissue engineering have highlighted the importance of the development of composite materials based on biodegradable polymers containing bioactive glasses, in particular, composites for high load support and excellent cell viability for potential application in bone regeneration. In this work, hybrid composite films were obtained by combining chitosan with bioactive glass in solution form and in nanoparticle dispersion form obtained by the two different synthesis routes: the sol-gel method and coprecipitation. The bioactive glass served both as a mechanical reinforcing agent and as a triggering agent with high bioactivity. The results of *in vitro* assays with simulated body fluid demonstrated the formation of a significant layer of fibrils on the surface of the film, with a typical morphology of carbonated hydroxyapatite, reflecting induction of a favorable bioactivity. Maximum tensile stress increased from 42 to 80 MPa to the sample with 5% wt bioactive glass. In addition, samples containing 5% and 10% wt bioactive glass showed a significant increase in cell viability, 18 and 30% increase compared to the control group. The samples showed significant response, indicating that they could be a potential material for use in bone regeneration through tissue engineering.

1. Introduction

Nanoscale systems have generated promising results in bone tissue engineering; a growing consensus of the literature focuses on the development of nanostructured materials based on ceramics or bioactive glasses because of their high capacity for biomineralization [1–4]. The use of nanometer size particles is known to influence the increase in bioactivity of ceramic materials; in addition, the inorganic phase may act as a reinforcing agent for improving the mechanical properties of the material [5, 6]. The production of nanocomposites based on biodegradable polymers and

bioactive glasses has been the focus of extensive studies in the literature, which combines the ability of glass to form a strong bond with the bone tissue surface [7, 8]. Bioactive glasses in the system $\text{SiO}_2\text{-CaO-P}_2\text{O}_5$ have been investigated as biomaterials to be introduced into the organic phase due to their osteoconductivity properties. When a bioactive glass is implanted, a biological response is generated at the interface of the material, leading to a chemical bond between the tissue and the material [9, 10]. The biomineralization ability of bioactive glasses is related to their composition but is also influenced by their physical properties, such as particle size, porosity, surface area, and morphology [11–13].

The introduction of the bioactive phase in the polymeric composites has generally been produced by the sol-gel method, which is a versatile method that allows the incorporation of inorganic components into polymers at the molecular scale and at low temperatures, resulting in a hybrid material or nanocomposite material [7, 14].

Chitosan is a natural polymer that has shown promising performance in tissue engineering. This polymer has been extensively studied as a biomaterial because it has unique biomedical properties, mainly due to the ability to biodegrade [15, 16], the high biocompatibility [17] with immunogenicity, the ability to act as an antibacterial agent [18], and the antifungal properties [19] in wound healing, in addition to the benefit that the degradation products of chitosan do not generate toxic materials and are not carcinogenic [7, 20]. However, chitosan as a pure material is not ideal for bone regeneration because its osteoconductivity needs to be improved [21]. Because chitosan does not exhibit high bioactivity, it is necessary to combine it with another bioactive material to improve the osteoconductivity [22]. Furthermore, when a cross-linking agent, such as glutaraldehyde, is added to chitosan, it significantly increases its mechanical properties [23]. The mechanical properties are of crucial importance, especially in regard to regeneration of hard tissue such as bone, which requires load support. Therefore, the combination of chitosan and silica-based nanoparticles to form a hybrid nanocomposite is a strategy to address the demands of mechanical loading on bone grafts. There are a few studies demonstrating the interaction at the molecular level of chitosan with silica-based materials [2, 3, 6, 15, 19]. Chitosan has functional groups, such as hydroxyl groups and amines, which have high possibility of rapidly bonding to other functional groups. Hybrids formed from chitosan and silica exhibited an increase of the interfacial interaction with improved mechanical properties [3].

In this work, two strategies were used to produce bioactive nanocomposites: one strategy involves a solution (sol-gel) and the other strategy involves a nanoparticle dispersion obtained by combination of the sol-gel method and the coprecipitation method. These two synthesis routes were used to produce membranes, which were evaluated in terms of their mechanical properties, bioactivity, and biological synthesis for future use in scaffolds of bone tissue engineering.

2. Materials and Methods

Commercial chitosan (high molecular weight and degree of deacetylation 75–85%), tetraethylorthosilicate (TEOS, 98%), and triethyl phosphate (TEP-99%) were supplied by Sigma-Aldrich, and ammonia (NH_3) and $\text{Ca}(\text{NO}_3)_2 \cdot 4\text{H}_2\text{O}$ (99%) were supplied by Synth. The composition of the bioactive glass was 60%:SiO₂, 36%:CaO, and 4%:P₂O₅ (% mol). A solution of glutaraldehyde 2.0% w/v was obtained by dilution of a commercial solution (25% w/v, Sigma-Aldrich).

2.1. Bioactive Glass Solution Preparation. The bioactive glass precursor solution was obtained by acid hydrolysis and polycondensation of tetraethylorthosilicate (TEOS

($\text{Si}(\text{OC}_2\text{H}_5)_4$)), alkoxide precursor of SiO₂, triethyl phosphate (TEP ($(\text{C}_2\text{H}_5\text{O})_3\text{PO}_4$)), and alkoxide precursor P₂O₅. The hydrolysis occurred by adding deionized water and was catalyzed by nitric acid. Calcium nitrate ($\text{Ca}(\text{NO}_3)_2 \cdot 4\text{H}_2\text{O}$) was added as a precursor of CaO.

2.2. Bioactive Glass Nanoparticle Dispersion Preparation. The method of preparation of BGNPs was based on previous work [4, 5] consisting of combining the sol-gel coprecipitation method. In the first step, TEOS and TEP precursors were hydrolyzed under acidic conditions. The precursors were dispersed in methanol and water, and the pH was adjusted to 1-2 by nitric acid. The mixture was kept under magnetic stirring to obtain a transparent sol. In this second step, transparent sol (monodisperse) was condensed separately in alkaline solution. The sol was then dripped in deionized water with ammonium hydroxide under vigorous mechanical agitation. The pH of the solution was adjusted in the range of 10 to 12. After 12 h of mechanical stirring, the suspension was taken to the oven 50 °C to evaporate the ammonia (until pH < 8). Calcium nitrate was added and kept under mechanical stirring for 24 h. The dispersion obtained was filtered through Millipore filters of 0.22 μm and 0.11 μm; after passing the dispersion through each of the filters, the dispersion was collected and stored for later use. The final appearance of the dispersion was a colorless liquid.

2.3. Hybrid CS-BG Films Preparation. The hybrid films were obtained by mixing 1% w/v chitosan solution with the precursor solution bioactive glass of the following compositions: 10 wt%, 20 wt%, and 30 wt%; these materials were then cross-linked with glutaraldehyde corresponding to 3% of the total weight of chitosan. Films from pure chitosan were produced. The final solution was poured into polypropylene dishes and kept at room temperature for approximately 60 h. They were then placed in an oven (40 ± 2 °C) for 24 h for complete drying.

2.4. Nanocomposites CS-BGNP Films Preparation. The nanocomposite films were obtained by dissolving 1% w/v chitosan commercial powder in the previously prepared dispersion of BGNP (item 2.2), based on previous work under acidic conditions, to obtain the following concentrations of nanoparticles in the films compositions: 1 wt%, 3 wt%, 5 wt%, and 10 wt%. The dissolution procedure consists of the following steps. Deionized water was added to the dispersion BGNP under mechanical stirring; the dispersion was measured to have pH above 7. Nitric acid was added to obtain pH = 2.5. Chitosan powder was added slowly while maintaining the pH below approximately 4. After stabilization, the suspension was kept under mechanical stirring for 24 h. Glutaraldehyde, corresponding to 3 wt% of the total weight of chitosan (the same amount used to synthesize the hybrid films previously described), was added into the suspension, which was subsequently poured into a Petri dish and then kept at room temperature for 60 h. Finally, the suspension was completely dried in an oven (40 ± 2 °C) for 24 h.

2.5. In Vitro Bioactivity Tests. The synthesis conditions of the hybrids typically resulted in a product of polymeric character that is sensitive to high temperatures, which prevents the elimination of toxic substances by thermal treatment [24]. When in contact with the culture medium, the dissolution of hybrid products may change the pH of the medium and the cell growth, promoting lower cell viability. This change requires a neutralization step to reduce the acidity of the samples and to make them more biocompatible. Therefore, to assess the bioactivity, a pre-study of variation of pH and hybrid nanocomposites in a solution of SBF (kept at 37°C) was conducted. Samples containing 0 wt%, 10 wt%, 20 wt%, and 30 wt% of BG and samples containing 0 wt%, 1 wt%, 3 wt%, and 5 wt% of BGNP were immersed for zero days, one day, seven days, and 28 days, followed by the measurement of the pH.

The biomineralization tests were performed according to ISO/FDIS 23317:2007 (E) [25–28]. Films with 20 wt% of either BG or BGNP were used in these tests. The samples in triplicate that were cut to a size of 10 mm × 20 mm were immersed in SBF (simulated body fluid) and kept for one day, seven days, and 28 days. The quantity of 40 mL of SBF was used to obey the relationship between the surface area of the sample (S_a) in square millimeters and the volume of SBF solution (V_s) in milliliters given by $V_s = S_a/10$. The vials containing the samples were placed in a water bath at $37 \pm 2^\circ\text{C}$. After removing the samples from the SBF, they were washed and dried at room temperature. The level of mineralization of the films after immersion was evaluated by scanning electron microscopy (SEM). Fourier transform infrared (FTIR) spectroscopy was also used to confirm the presence of the components of carbonated hydroxyapatite (CHA) (Nicolet 380 of ThermoScientific). Moreover, the standard bioactivity ISO/FDIS 23317: 2007 (E) describes that SEM and FT-IR data must be accompanied by analysis of X-ray diffraction (XRD) data to confirm the formation of the CHA and therefore the formation of the CHA layer was also investigated by XRD [29].

2.6. Mechanical Tests. The selection of samples subjected to tensile tests was defined as the most homogeneous region of the films to obtain more representative results in the mechanical test. The samples of the films were subjected to the tensile test to evaluate the tensile strength and the strain at break. The films were subjected to the test with an initial spacing between the gauge lengths of 50 mm. To ensure accurate results, 6–8 samples of each film were submitted to testing. The tests were conducted on the Machine Model 3000 EMIC DL, using a 200 N load cell, a test speed of 25 mm min^{-1} , and a test temperature of $26 \pm 2^\circ\text{C}$. The tensile tests were performed according to ASTM D882-10 (Standard Test Method for Tensile Properties of Thin Plastic Sheeting) [30].

2.7. In Vitro Cytotoxicity Tests. The films synthesized were submitted to the first stage of *in vitro* evaluation by the cytotoxicity test following 10993-5:1999 (*Biological evaluation of medical devices; Part 5: tests for in vitro cytotoxicity*) [25–28].

TABLE 1: pH of the medium and the hybrid nanocomposite films as a function of immersion time in SBF.

Samples (wt%)	Immersion time in SBF			
	0 h	1 day	7 days	28 days
CS	7.40	7.45	7.35	7.40
CS—10% BG	7.40	7.34	7.49	7.25
CS—20% BG	7.40	7.33	7.45	7.35
CS—30% BG	7.40	7.32	7.50	7.22
CS—1% BGNP	7.40	7.37	7.31	7.36
CS—3% BGNP	7.40	7.35	7.32	7.24
CS—5% BGNP	7.40	7.31	7.29	7.28
CS—10% BGNP	7.40	7.39	7.34	7.30

The Resazurin cell viability assay was used. Human osteosarcoma cells (SAOS), a commercial line of immortalized cells, were kindly provided by Professor Alfredo Miranda Goes, the Department of Biochemistry and Immunology, UFMG. The cells were cultured in DMEM with 10% fetal bovine serum (Gibco BRL, NY), penicillin G sodium (10 IU/mL), streptomycin sulfate (10 mg/L), and 0.25 amphotericin B (Gibco BRL, NY, USA) in an incubator with 5% CO_2 at 37°C. Samples of the films CS-BG and CS-BGNP with 12 mm in diameter were placed in 24-well plates and cells were plated (1×10^4 cells) on each sample material. Cells with DMEM and 10% FBS were used as reference controls, as positive control PBS (2X), and as negative control chips of sterile polypropylene Eppendorf (0.1 mg/mL) from Eppendorf (Hamburg, Germany). The method of sterilization was ultraviolet radiation for 30 minutes on each side of the samples [31–33]. Tests were performed in triplicate ($n = 3$) for each sample type. After 72 h, all of the media were aspirated, and 900 μL of culture medium with serum was placed into each well. One hundred microliters of Resazurin (0.1 mg/mL, Sigma-Aldrich, USA) was added in each well, which was placed in an incubator for a period of 18 h with 5% CO_2 at 37°C. Then, 100 μL was removed from each well and transferred to 96-well flat plates, and the measurement was performed using a spectrophotometer (1.6 Adap, Anthos Labtec Instruments) with two filters of 570 nm and 590 nm.

3. Results and Discussion

3.1. Qualitative Assessment. Homogeneous films were produced by the technique of evaporation of the solvent and visually exhibited a yellowish transparent glossy surface. The films and hybrid nanocomposites containing higher levels of bioactive glass (30 wt% of BG) underwent a change in their physical appearance after drying: the structure retracted and exhibited a loss of flexibility, thereby making the surface appear opaque. This behavior is clearly observed in the films with 30 wt% of bioactive glass.

3.2. Tests of the In Vitro Bioactivity. Table 1 presents the pH values of the medium after immersion of the nanocomposite. The pH values obtained ranged from 7.22 to 7.50; therefore,

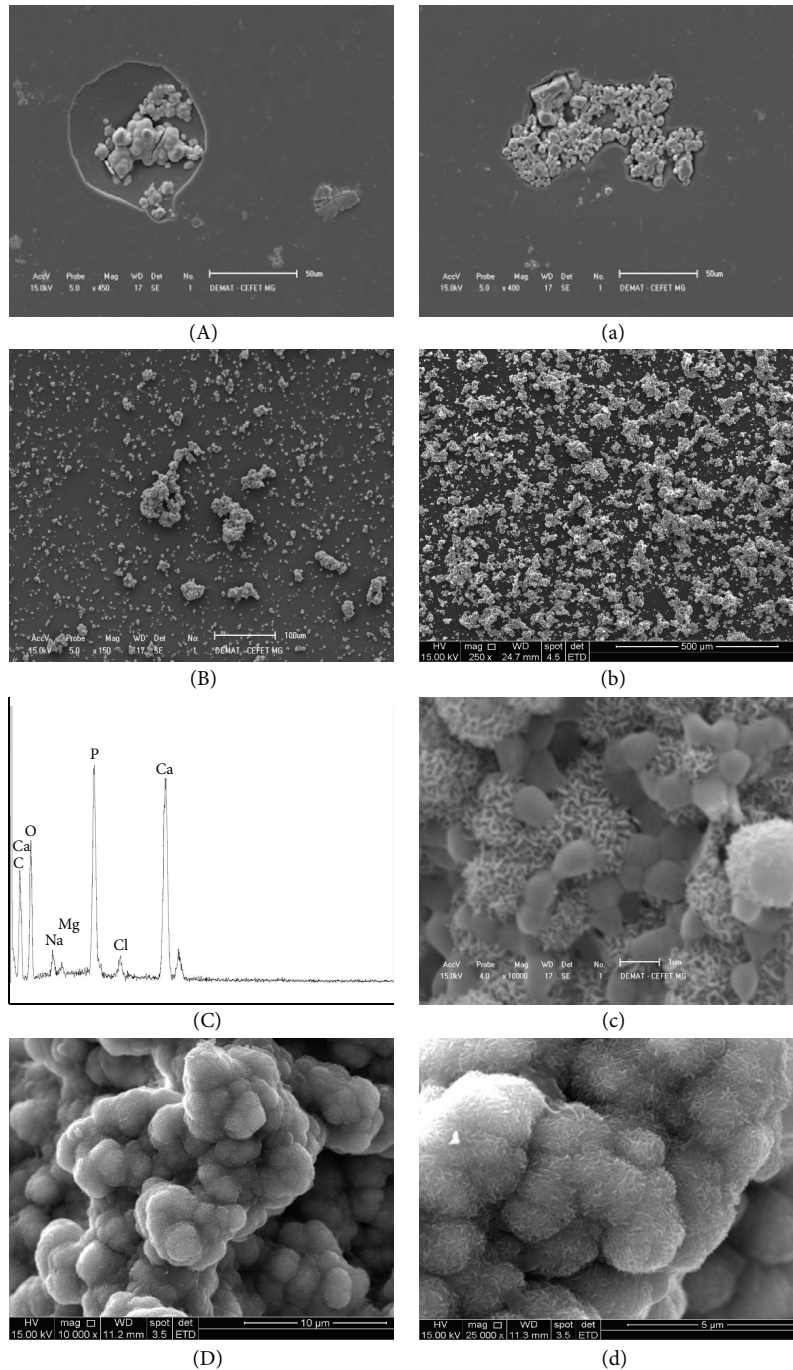


FIGURE 1: SEM images of the surface of the films with 20 wt% BG immersed in SBF for one day ((A), (a)), seven days ((B), (b)), or 28 days (c-D-d). EDS image of the film immersed in SBF for 28 days (C).

there was not a significant change of pH in the solution of PBS, indicating that the samples were stable in this aspect and indicating that a neutralization step was not required.

SEM images of the surface of the films with 20 wt% BG immersed in SBF for one day, seven days, or 28 days are shown in Figure 1. Gradual formation of CHA with increasing days of immersion in SBF was observed in the SEM images (Figure 1(A-d)).

On the surface of the hybrid films (20 wt% of BG), a homogeneous morphology was observed due to the dispersion of small crystals with sizes less than $5\ \mu\text{m}$, which characterizes the formation of the CHA layer. Initially, the apatite grains were more isolated (Figure 1(A-a)) and, after seven days, exhibited a uniform and thicker layer on the surface of the hybrid (Figure 1(B-b)). After 28 days the film surface was completely covered by CHA, exhibiting a more

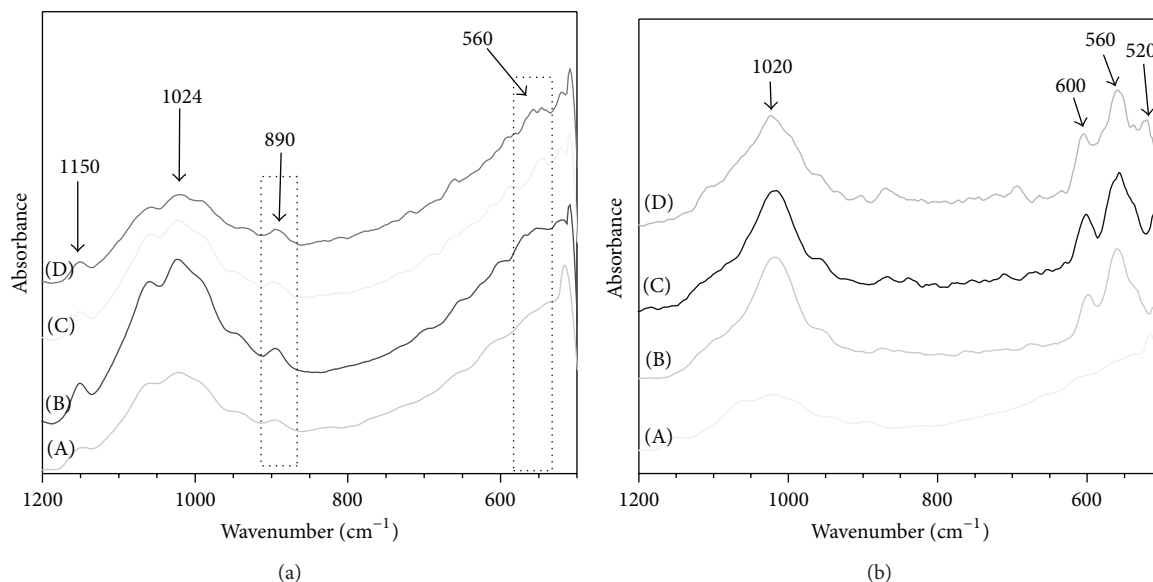


FIGURE 2: FTIR film after one day of immersion (a) and after 28 days of immersion in SBF (b): (A) CS, (B) 10, (C) 20, and (D) 30 wt% BG.

intense biological response, according to the increase of the immersion time (Figure 1(c-D-d)). The identification of the chemical composition of these crystals was performed by EDS, which indicated the presence of Ca (Calcium) and P (phosphorus), as shown in Figure 1(C). Although the analysis by EDS does not represent a quantitative analysis, the Ca and P peaks were very significant in the sample.

The FTIR spectra (Figure 2(a)) for pure chitosan films and for films containing 10, 20, and 30 wt% content of bioactive glass after immersion in SBF immersed for one day to 28 days showed vibration bands at 520 cm^{-1} , 560 cm^{-1} , and 600 cm^{-1} corresponding to the bending vibration of P-O. These results indicated the formation of a crystalline layer of calcium phosphate. The bands at 600 cm^{-1} are related to the PO_4^{2-} group, as shown in Figures 2(a) and 2(b). The band at 890 cm^{-1} that is related to the stretching vibration of the CO_3^{2-} group was more evident in the films with a 10, 20, and 30 wt% content of bioactive glass, as shown in Figure 2(a). The FTIR spectrum of films containing 30 wt% bioactive glass after 28 days of immersion, shown in Figure 2(b), reveals a band at 520 cm^{-1} related to the bending vibration of P-O. Bands at 1024 , 1020 , and 1150 cm^{-1} for films with one-day immersion, as shown in Figures 2(a) and 2(b), are indicative of the shift of the 1100 cm^{-1} band, which is attributed to the stretching P-O. The intensities of the bands increased after 28 days of immersion, indicating the formation of the CHA layer. Films of pure chitosan did not exhibit bands related to the formation of CHA [14, 34, 35].

CHA formation was also recorded by XRD (Figure 3). The XRD patterns of the films revealed a peak with a high intensity at $2\theta = 32^\circ$ and another peak with a low intensity at $2\theta = 26^\circ$, which are associated with the planes (211) and (002), respectively [4, 19, 36, 37]. These peaks are characteristic of the crystalline phase of CHA according to record 19-274 (JCPDS). However, these two peaks only appear in the hybrid

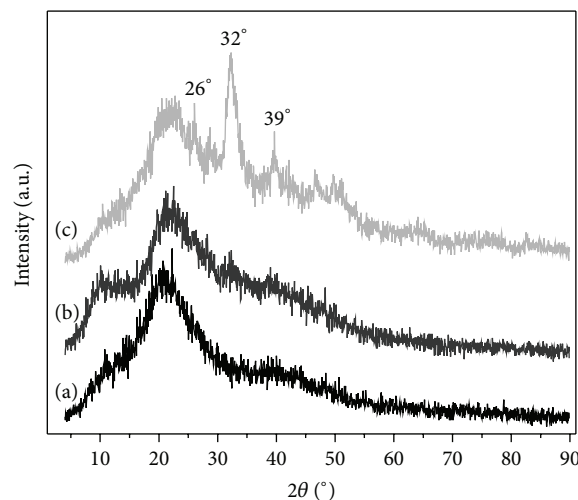


FIGURE 3: XRD film after seven days of immersion in SBF: (a) CS, (b) 10, and (c) 20 wt% BG.

with 20 wt% of BG. The XRD patterns of the films containing 0 and 10 wt% glass exhibited broad peaks, indicating that the analyzed area has little or no crystallinity and therefore exhibits low bioactive property. Both the pure chitosan and the film with 10 wt% BG exhibited no diffraction peaks, indicating that these were amorphous materials. The film with 30 wt% BG was not examined by XRD because it was not possible to investigate its surface, due to the irregularities caused by it containing high concentration of BG.

3.3. In Vitro Cytotoxicity Assay. The mitochondrial activity of osteoblasts cultured with and without the presence of materials produced in this work was evaluated by the Resazurin test. This test is used to specifically assess mitochondrial

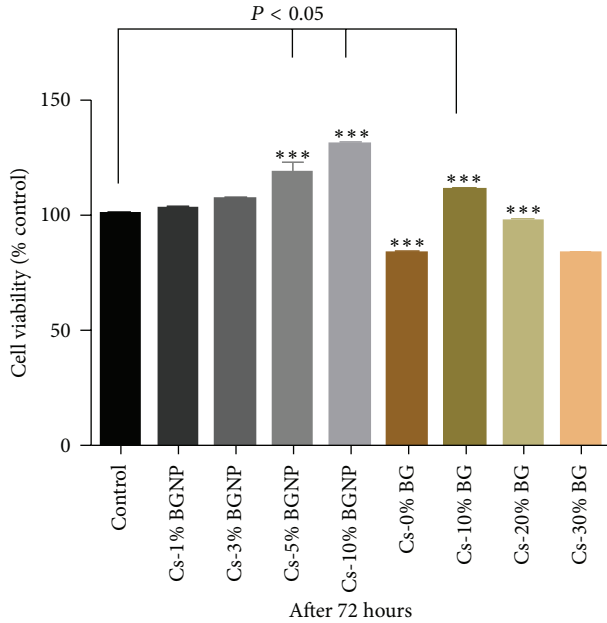


FIGURE 4: Cell viability of hybrid CS-BG and the CS-BGNP nanocomposites. *Statistically significant difference ($P < 0.05$). Statistical analysis performed by ANOVA/Bonferroni/GraphPad Prism.

function and cell viability. Figure 4 illustrates the hybrid cell viability of hybrids (CS-BG) and the nanocomposites (CS-BGNP). In the control group, the cells were seeded only by viable osteoblasts (no samples in the middle). In comparative groups, the cells were seeded on each film composition of the hybrid nanocomposites. Comparing the films analyzed with the control group after 72 h, it can be concluded that as the content of the material BGNP increased, the cell viability also increased, and this difference was statistically significant ($P < 0.05$) for films with 5 and 10 wt% BGNP. The results indicated that cells plated on 5% CS-BGNP exhibited an increase of $18 \pm 7.5\%$ cell viability and the cells plated on CS-BGNP 10% exhibited an increase of $30 \pm 2\%$ cell viability compared to the control group. The cells plated in 10% CS-BG exhibited a $10 \pm 1\%$ increase in the cell viability. Studies in the literature identified that the higher cell viability compared to control when using bioactive glasses with 60% silica can be attributed to the ability of the ionic products from these materials to stimulate osteoblast proliferation [38]. Cells plated on CS 1% BGNP and CS 3% BGNP after 72 h exhibited a cell viability similar to that of the control group which was significantly higher compared to the viability of pure chitosan (CS 0% BG). No significant differences in cell viability were found compared to the control group of cells plated on CS 20% BG. A decrease in cell viability was observed compared to the control group for cells plated on pure chitosan and 30 wt% CS-BG. The biological tests conducted with Resazurin in cells grown on the samples after 72 h indicated that samples containing nanoparticles of bioactive glass were more favorably increasing cell viability, but the results obtained by the hybrids CS-BG also induced

TABLE 2: Comparison of mean values of maximum stress and strain for the films CS-BGNP and CS-BG.

Sample (wt%)	Maximum tensile stress (MPa)	Maximum deformation (%)
CS	42 ± 5.5	12 ± 2.9
CS 1% BGNP	62 ± 4.3	14 ± 2.2
CS 3% BGNP	73 ± 5.2	22 ± 3.1
CS 5% BGNP	80 ± 5.0	21 ± 3.1
CS 10% BGNP	68 ± 4.6	11 ± 2.9
CS 10% BG	53 ± 7.0	5 ± 2.0
CS 20% BG	67 ± 4.9	4 ± 0.9
CS 30% BG*	X	X

*Films for which tensile tests could not be performed.

a significant response from the cells because cell death was not markedly observed.

3.4. Tensile Testing. Figure 5(a) shows the stress-strain behavior relative to pure chitosan and films with 10 and 20 wt% of bioactive glass, each cross-linked with glutaraldehyde. In general, the behavior of the stress-strain curves is typical of a plastic material. It was observed that the films with bioactive glass decrease their percentage of elongation at break while they gradually increase its tensile strength. The bioactive glass behaves as typical reinforcing filler. The chitosan film exhibited a strength value of 42 MPa and elongation at break of 11% (Table 2). The film with 10 wt% of bioactive glass increased its maximum strength to 53 MPa, while its elongation at break decreases to 5%. The film containing 20% glass undergoes a large increase in the maximum tensile strength reaching values of 67 MPa, although its elongation at break decreases to 4%. This behavior occurs due to interactions in the polymer network with the glass; the dispersion of the sol changes the chitosan matrix structure, leaving the hybrid with a less flexible structure, lessening its ductility compared to the films that did not undergo the addition of bioactive glass. Figure 5(b) illustrates the stress-strain curves for films of chitosan with 1, 3, 5, and 10% BGNP, all of which are cross-linked with glutaraldehyde.

Tasselli et al. [23] investigated the mechanical properties of chitosan cross-linked with different glutaraldehyde content. For low contents of glutaraldehyde added an increase of the mechanical properties compared to pure chitosan was observed, unlike what was observed with higher contents added, for which the tensile strength decreased dramatically. Similar results were observed in this work. Although cross-linked chitosan produced in this work presented slightly smaller tensile strength than those found by the authors, the mechanical properties were significantly improved after the addition of BGNP.

The behavior in the tensile tests of nanocomposite films with BGNP is fairly similar to the behavior of the hybrid films with BG. The films exhibited a flexible behavior, and their stress-strain curves are typical of a plastic. The nanocomposite films were strongly influenced by the BGNP

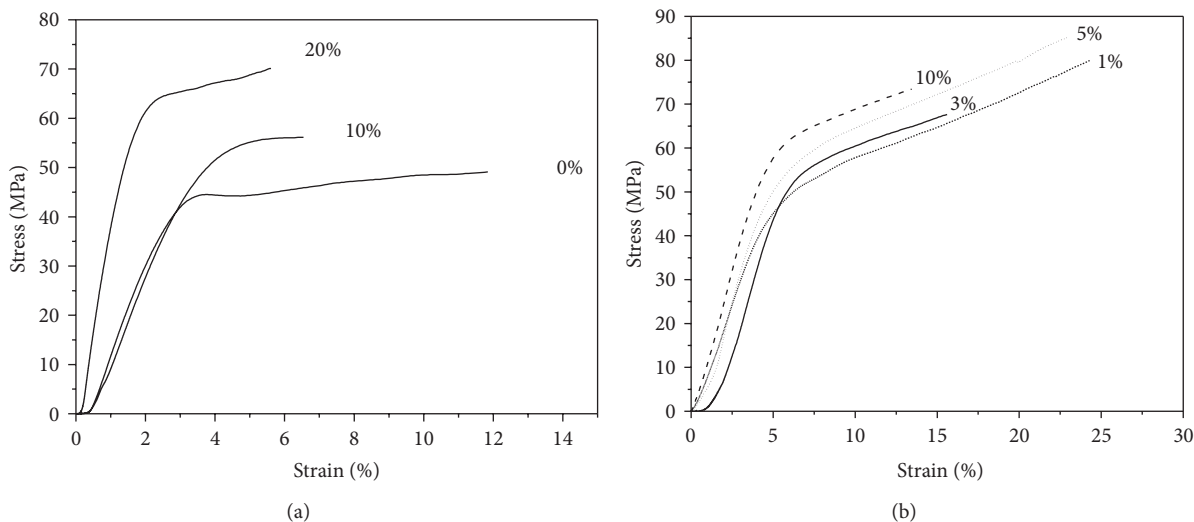


FIGURE 5: Stress-strain curves obtained from tensile testing of hybrid films with 0, 10, and 20 wt% in BG (a) and the nanocomposite films with 1, 3, 5, and 10 wt% of BGNP (b).

content and exhibited high performance in comparison with the other hybrid films tested. Films with 3 and 5 wt% BGNP reached maximum strength values of 73 MPa and 80 MPa, respectively. The elongation at break was also very significant, with percentages of 22% and 21% for films with 3 wt% and 5 wt% BGNP, respectively.

4. Conclusions

Hybrid composite films produced by homogeneous chitosan and bioactive glass have been successfully obtained using the two synthetic routes of sol-gel and coprecipitation, achieving adequate performance for the application as a guide to the cell growth of bone tissue. Both systems of CS-BG as CS-BGNP films exhibited high tensile strength and high bioactivity and cell viability. These results indicate that the use of bioactive glass successfully acted as an agent for loading and improved bioactivity, particularly in the form of nanoparticle dispersion (BGNP), whose results are the most promising.

Conflict of Interests

The authors declare that there is no conflict of interests regarding the publication of this paper.

Acknowledgments

The authors thank FAPEMIG, CAPES, and CNPq for the financial support of the work.

References

- [1] S. I. Roohani-Esfahani, S. Nouri-Khorasani, Z. F. Lu, R. C. Appleyard, and H. Zreiqat, "Effects of bioactive glass nanoparticles on the mechanical and biological behavior of composite coated scaffolds," *Acta Biomaterialia*, vol. 7, no. 3, pp. 1307–1318, 2011.
- [2] M. Peter, N. S. Binulal, S. Soumya et al., "Nanocomposite scaffolds of bioactive glass ceramic nanoparticles disseminated chitosan matrix for tissue engineering applications," *Carbohydrate Polymers*, vol. 79, no. 2, pp. 284–289, 2010.
- [3] F. Al-Sagheer and S. Muslim, "Thermal and mechanical properties of chitosan/SiO₂ hybrid composites," *Journal of Nanomaterials*, vol. 2010, Article ID 490679, 7 pages, 2010.
- [4] D. S. Couto, Z. Hong, and J. F. Mano, "Development of bioactive and biodegradable chitosan-based injectable systems containing bioactive glass nanoparticles," *Acta Biomaterialia*, vol. 5, no. 1, pp. 115–123, 2009.
- [5] A. R. Boccaccini, M. Erol, W. J. Stark, D. Mohn, Z. Hong, and J. F. Mano, "Polymer/bioactive glass nanocomposites for biomedical applications: a review," *Composites Science and Technology*, vol. 70, no. 13, pp. 1764–1776, 2010.
- [6] J. R. Jones, "New trends in bioactive scaffolds: the importance of nanostructure," *Journal of the European Ceramic Society*, vol. 29, no. 7, pp. 1275–1281, 2009.
- [7] J. Mota, N. Yu, S. G. Caridade et al., "Chitosan/bioactive glass nanoparticle composite membranes for periodontal regeneration," *Acta Biomaterialia*, vol. 8, no. 11, pp. 4173–4180, 2012.
- [8] K.-Y. Lee, M. Park, H.-M. Kim, Y.-J. Lim, H.-J. Chun, and S.-H. Moon, "Ceramic bioactivity: progresses, challenges and perspectives," *Biomedical Materials*, vol. 1, no. 2, pp. R31–R37, 2006.
- [9] S. M. Carvalho, A. A. R. Oliveira, E. M. F. Lemos, and M. M. Pereira, "Bioactive glass nanoparticles for periodontal regeneration and applications in dentistry," in *Nanobiomaterials in Clinical Dentistry*, vol. 1, chapter 15, pp. 299–322, Elsevier, Waltham, Mass, USA, 2012.
- [10] D. Lukito, J. M. Xue, and J. Wang, "In vitro bioactivity assessment of 70 (wt.%)SiO₂-30 (wt.%)CaO bioactive glasses in simulated body fluid," *Materials Letters*, vol. 59, no. 26, pp. 3267–3271, 2005.
- [11] T. J. Webster, R. W. Siegel, and R. Bizios, "Osteoblast adhesion on nanophase ceramics," *Biomaterials*, vol. 20, no. 13, pp. 1221–1227, 1999.
- [12] T. J. Webster, R. W. Siegel, and R. Bizios, "Nanoceramic surface roughness enhances osteoblast and osteoclast functions for

- improved orthopaedic/dental implant efficacy," *Scripta Materialia*, vol. 44, no. 8-9, pp. 1639-1642, 2001.
- [13] M. N. V. R. Kumar, R. A. A. Muzzarelli, C. Muzzarelli, H. Sashiwa, and A. J. Domb, "Chitosan chemistry and pharmaceutical perspectives," *Chemical Reviews*, vol. 104, no. 12, pp. 6017-6084, 2004.
- [14] M. M. Pereira, J. R. Jones, and L. L. Hench, "Bioactive glass and hybrid scaffolds prepared by sol-gel method for bone tissue engineering," *Advances in Applied Ceramics*, vol. 104, no. 1, pp. 35-42, 2005.
- [15] E.-J. Lee, D.-S. Shin, H.-E. Kim, H.-W. Kim, Y.-H. Koh, and J.-H. Jang, "Membrane of hybrid chitosan-silica xerogel for guided bone regeneration," *Biomaterials*, vol. 30, no. 5, pp. 743-750, 2009.
- [16] L. Dupoirieux, D. Pourquier, M. C. Picot, and M. Neves, "Comparative study of three different membranes for guided bone regeneration of rat cranial defects," *International Journal of Oral and Maxillofacial Surgery*, vol. 30, no. 1, pp. 58-62, 2001.
- [17] N. M. Alves and J. F. Mano, "Chitosan derivatives obtained by chemical modifications for biomedical and environmental applications," *International Journal of Biological Macromolecules*, vol. 43, no. 5, pp. 401-414, 2008.
- [18] C. Chatelet, O. Damour, and A. Domard, "Influence of the degree of acetylation on some biological properties of chitosan films," *Biomaterials*, vol. 22, no. 3, pp. 261-268, 2001.
- [19] M. Peter, P. T. Sudheesh Kumar, N. S. Binulal, S. V. Nair, H. Tamura, and R. Jayakumar, "Development of novel α -chitin/nanobioactive glass ceramic composite scaffolds for tissue engineering applications," *Carbohydrate Polymers*, vol. 78, no. 4, pp. 926-931, 2009.
- [20] A. Lahiji, A. Sohrabi, D. S. Hungerford, and C. G. Frondoza, "Chitosan supports the expression of extracellular matrix proteins in human osteoblasts and chondrocytes," *Journal of Biomedical Materials Research Part A*, vol. 51, pp. 586-595, 2000.
- [21] Y. Zhang and M. Zhang, "Synthesis and characterization of macroporous chitosan/calcium phosphate composite scaffolds for tissue engineering," *Journal of Biomedical Materials Research Part A*, vol. 55, pp. 304-312, 2001.
- [22] L. Kong, Y. Gao, G. Lu, Y. Gong, N. Zhao, and X. Zhang, "A study on the bioactivity of chitosan/nano-hydroxyapatite composite scaffolds for bone tissue engineering," *European Polymer Journal*, vol. 42, no. 12, pp. 3171-3179, 2006.
- [23] F. Tasselli, A. Mirmohseni, M. S. Seyed Dorraji, and A. Figoli, "Mechanical, swelling and adsorptive properties of dry-wet spun chitosan hollow fibers crosslinked with glutaraldehyde," *Reactive and Functional Polymers*, vol. 73, no. 1, pp. 218-223, 2013.
- [24] A. A. R. de Oliveira, V. S. Gomide, M. de Fátima Leite, H. S. Mansur, and M. de Magalhães Pereira, "Effect of polyvinyl alcohol content and after synthesis neutralization on structure, mechanical properties and cytotoxicity of sol-gel derived hybrid foams," *Materials Research*, vol. 12, no. 2, pp. 239-244, 2009.
- [25] M. Rolón, C. Vega, J. A. Escario, and A. Gómez-Barrio, "Development of resazurin microtiter assay for drug sensibility testing of *Trypanosoma cruzi* epimastigotes," *Parasitology Research*, vol. 99, no. 2, pp. 103-107, 2006.
- [26] D. Liu, "A rapid biochemical test for measuring chemical toxicity," *Bulletin of Environmental Contamination and Toxicology*, vol. 26, no. 2, pp. 145-149, 1981.
- [27] R. K. Pettit, C. A. Weber, M. J. Kean et al., "Microplate alamar blue assay for *Staphylococcus epidermidis* biofilm susceptibility testing," *Antimicrobial Agents and Chemotherapy*, vol. 49, no. 7, pp. 2612-2617, 2005.
- [28] J. O'Brien, O. Wilson, T. Orton, and F. Pognan, "Investigation of the Alamar blue (resazurin) fluorescent dye for the assessment of mammalian cell cytotoxicity," *European Journal of Biochemistry*, vol. 267, no. 17, pp. 5421-5426, 2000.
- [29] International Organization for Standardization, "Implants for surgery—in vitro evaluation for apatite-forming ability of implant materials," ISO 23317, 2007.
- [30] ASTM D882-12, *Standard Test Method for Tensile Properties of Thin Plastic Sheeting*, American Society for testing and Materials International, West Conshohocken, Pa, USA.
- [31] C. E. Bayliss and W. M. Waites, "The combined effect of hydrogen peroxide and ultraviolet irradiation on bacterial spores," *Journal of Applied Bacteriology*, vol. 47, no. 2, pp. 263-269, 1979.
- [32] C. J. Stannard, J. S. Abbiss, and J. M. Wood, "Combined treatment with hydrogen peroxide and ultra-violet irradiation to reduce microbial contamination levels in pre-formed food packaging cartons," *Journal of Food Protection*, vol. 46, no. 12, pp. 1060-1064, 1983.
- [33] W. M. Waites, S. E. Harding, D. R. Fowler, S. H. Jones, D. Shaw, and M. Martin, "The destruction of spores of *Bacillus subtilis* by the combined effects of hydrogen peroxide and ultraviolet light," *Letters in Applied Microbiology*, vol. 7, no. 5, pp. 139-140, 1988.
- [34] O. Peitl, E. Dutra Zanotto, and L. L. Hench, "Highly bioactive P_2O_5 - Na_2O - CaO - SiO_2 glass-ceramics," *Journal of Non-Crystalline Solids*, vol. 292, no. 1-3, pp. 115-126, 2001.
- [35] P. Sepulveda, J. R. Jones, and L. L. Hench, "In vitro dissolution of melt-derived 45S5 and sol-gel derived 58S bioactive glasses," *Journal of Biomedical Materials Research*, vol. 61, no. 2, pp. 301-311, 2002.
- [36] R. Jayakumar, D. Menon, K. Manzoor, S. V. Nair, and H. Tamura, "Biomedical applications of chitin and chitosan based nanomaterials—a short review," *Carbohydrate Polymers*, vol. 82, no. 2, pp. 227-232, 2010.
- [37] X. Cai, H. Tong, X. Shen, W. Chen, J. Yan, and J. Hu, "Preparation and characterization of homogeneous chitosan-poly(lactic acid)/hydroxyapatite nanocomposite for bone tissue engineering and evaluation of its mechanical properties," *Acta Biomaterialia*, vol. 5, no. 7, pp. 2693-2703, 2009.
- [38] P. Valerio, M. H. R. Guimarães, M. M. Pereira, M. F. Leite, and A. M. Goes, "Primary osteoblast cell response to sol-gel derived bioactive glass foams," *Journal of Materials Science: Materials in Medicine*, vol. 16, no. 9, pp. 851-856, 2005.

Research Article

Effectiveness of Two Self-Etchings Bonded Clinically in Caries Affected Dentin with Homogeneous Smear Layer

Roberto Pinna, Paolo Usai, Mariantonietta Arrica, and Egle Milia

Department of Biomedical Sciences, University of Sassari, Viale San Pietro 43/c, 07100 Sassari, Italy

Correspondence should be addressed to Egle Milia; emilia@uniss.it

Received 22 August 2014; Accepted 5 November 2014

Academic Editor: Jen-Jie Chieh

Copyright © 2015 Roberto Pinna et al. This is an open access article distributed under the Creative Commons Attribution License, which permits unrestricted use, distribution, and reproduction in any medium, provided the original work is properly cited.

Aim. To examine the interface of two self-etchings in carious affected dentin (CAD), under clinical conditions. *Materials and Methods.* Class I cavities were prepared in 21 carious premolars, refining them by the use of a fine diamond bur in order to create similar smear layer interference. The mild self-etching Clearfil SE Bond (CSE), pH = 2.0, and the strong Tyrian SPE-One Step Plus (TSO), pH = 0.5, were applied followed by a composite. Teeth were extracted and processed for TEM. The primer's osmolarity of the self-etchings was also calculated using a microosmometer. *Results.* CSE hybrid layer retained smear layer residues and scattered crystallites as an effect of the mild acidity. A high presence of hydroxyapatite still protected the affected fibres within the hybrid layer. CSE primer demonstrated values of 3220 mOsm/kg. TSO interdiffusion showed strong demineralization. Resin tags were not formed in the dentinal tubules which remained obstructed by crystals. However, dissolution of peritubular dentin and porosities were observed in the intertubular regions. The osmolarity of TSO was 8200 mOsm/kg. *Conclusion.* Increasing the acidity and osmolarity of the self-etchings increases interference in the homogeneous reinforcement of CAD, which may predispose the hybrid layer to instability and hydrolytic degradation overtime.

1. Introduction

In adhesive dentistry, carious affected dentin (CAD) represents a very common substrate. This is a result of “minimal invasion therapy” [1], which tends to fulfil the main requirements of a more conservative and aesthetic treatment with maximum conservation of tooth structure, already compromised by the bacterial infection.

Although CAD is able to interact with adhesive monomers [2], the hybrid layer may become unstable over time due to the complex tissue changes by the bacterial attack that lower the tensile strength and Knoop hardness in respect to normal dentin [3, 4]. This has been linked to the loss of minerals in intertubular dentin [5] that, at the same time, increases wetness with interference to infiltration of the monomers [6, 7].

When self-etching systems are used, bond strength has been related to the homogeneity of interdiffusion proceeding from the top smear layer toward the underlying features of the affected tissue [8, 9]. From this point of view, the maintenance

of acid resistant mineral occlusions in the affected tubules [4] with prevention of resin tags is not an important reason for lower strength than sound dentin, but a nonhomogeneous, poor infiltration of CAD would be the main reason [10].

Poor infiltration may be caused by the incapacity of self-etchings to completely infiltrate a thick and irregular smear layer, particularly when mild self-etching adhesives (pH = 2.0) are used [8]. This interference may cause a significant decrease in effectiveness of the hybrid layer after water exposure, with nanoleakage and degradation [11]. By lowering the pH of the primer by using strong self-etchings (pH ≤ 1) infiltration of the smear layer may be ensured; however more calcium-phosphate is dissolved, increasing wetness and porosities in clinical conditions [12, 13]. In fact, wetness may be already influenced by the clinical situation of pulpal pressure [14, 15] and the osmolarity of acidic primers [16], which favour the outward movement of dentinal fluids towards the surfaces of bonding.

To allow homogeneous infiltration of the smear in sound dentin, it was suggested that a thin smear layer of particles

TABLE 1: Adhesive agents used in the study (components and ingredients by manufacturer information).

Product	Components	Main ingredients
Clearfil SE Bond (Kuraray, Japan)	Self-etching primer	10-MDP, HEMA, hydrophilic dimethacrylate, photoinitiator, and water
	Bond	10-MDP, HEMA, Bis-GMA, hydrophobic dimethacrylate, photoinitiators, and silanated colloidal silica
Tyrian SPE/One-Step Plus (Bisco, IL, USA)	Self-etching primer	2-Acrylamido-2-methylpropanesulfonic acid, bis(2-(methacryloyloxy)ethyl) phosphate, and ethanol
	Bond	Biphenyl dimethacrylate, hydroxyethyl methacrylate, acetone, and glass frit

be produced in the surface by refining cavities with fine grit diamond burs [17]. However, this clinical procedure has not been evaluated in CAD, in which the morphology and chemical composition of the smear are different from those of unaltered dentin because of the diverse mineral/organic composition. The smear layer in CAD is richer in organic components and appears thicker than in sound dentin. The collagen component is a highly disorganized trapping mineral and cannot be easily removed even when strong acids are used [18]. A greater amount of “collagen smear layer,” compared with sound dentin, may be present on the surface of CAD because acids only solubilize the mineral component of the smear layer [12]. This collagen smear layer is impermeable to the monomers which inhibits uniform infiltration and will affect the quality of the bonding. Thus, the CAD smear layer may interfere with the infiltration of self-etching adhesives regardless of the manner in which it is created.

Although many studies have investigated the influence of dentin characteristics on bonding, little research has attempted to correlate self-etchings with the heterogeneous aspects of vital CAD in daily practice under clinical conditions. By carrying out clinical studies it is possible to evaluate the morphological expression of the bonding procedure as a result of the simultaneous interaction of tooth-adhesives in clinical conditions.

The object of this study was to evaluate the characteristics of interdiffusion of two types of two-step self-etching systems with differing pH values, bonded clinically in CAD cavities covered with a homogeneous smear layer of debris. The osmolarity of the primer components was also calculated.

2. Methods and Materials

In this study we used two types of two-step self-etching systems:

- (i) Clearfil SE Bond (CSE) (Kuraray, Osaka, Japan),
- (ii) Tyrian SPE/One-Step Plus (TOS) (Bisco, IL, USA).

Table 1 shows the ingredients and pH of the adhesives tested.

2.1. Experimental Design. This study was performed under a protocol approved by the Ethical Committee at the University of Sassari, Italy.

Fifteen subjects (mean age 47 ± 3 years), with a total of 21 carious premolars scheduled for extraction for periodontal reasons, were included in the study. The nature and scope of the study were explained to the participants, and informed

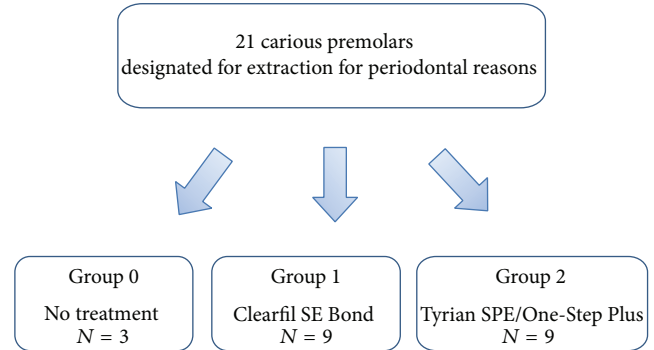


FIGURE 1: Flowchart of study methodology.

consent was obtained. The participants consented to the restoration of the carious teeth prior to extraction. Local anaesthetic without vasoconstrictor was administered to each participant and a rubber dam placed.

In the carious premolar teeth, cavities were performed by the same operator using the same equipment for both groups.

The soft caries-infected dentin was carefully removed by means of sharp spoon excavators and number 6 low speed round burs under water spray until the hard, discolored CAD was reached. Then, the cavities were finished using a fine diamond bur (number 8882.314.014 Komet, Lemgo, Germany) in order to create a homogeneous layer of smear debris.

After that, teeth were allocated to three groups (Figure 1), one of which ($N = 3$) received no treatment and served as a control of the created smear layer (Group 0); the other two ($N = 9$) received treatment using CSE bond (Group 1) and TOS (Group 2).

Both of the self-etching approaches were carried out according to the manufacturers' instructions (Table 2). The cavities were then bulk-filled with a flowable resin-based composite (Enamel Flow, Micerium, Avegno, Genova, Italy). Extractions were performed about 20 minutes after the polymerization of the adhesive materials.

Adhesive systems and the resin-based composite were cured using a halogen curing light (Optilux 501, Kerr Corporation, Orange, CA, USA; 11 mm exit window) under the standard curing mode (output wavelength range: 400–505 nm; output irradiance: 580–700 mW/cm²) at the standardized distance of 5 mm from the bonding surface.

Immediately after extraction teeth were prepared for TEM processing [19]. Specimens were rinsed in distilled

TABLE 2: pH values and application mode of the adhesive agents used in the study by manufacturer information.

Product	Adhesive classification	pH	Mode of application
Clearfil SE Bond (Kuraray, Japan)	Mild two-step self-etching system	2.0	Primer: apply primer to dentin for 20 seconds and gently air-blow for 5 seconds Bond: apply adhesive in a thin layer for 10 seconds, gently air-blow, and light-cure for 10 seconds
Tyrian SPE/One-Step Plus (Bisco, IL, USA)	Strong two-step self-etching system	0.5	Primer: mix 1-2 drops of Part A with 1-2 drops of Part B, apply primer to dentin for 20 seconds, and use a foam pellet to blot excess from preparation, leaving surface shiny Bond: apply 2 coats to the dentin for 10 seconds, gently air-blow, and light-cure for 10 seconds

water at 37°C and fixed in a solution of 2.5% glutaraldehyde with 0.1M PBS buffer, pH 7.2, for 72 hours. The specimens were then sectioned into two halves along their longitudinal axes, and each crown was sectioned from the root using a water-cooled saw (Isomet). Small rectangular fragments of tissue perpendicular to the center of each cavity were also obtained from the occlusal surface to produce 2 × 2 × ~8 mm sticks. Fragments were immersed in an aqueous solution of ethylenediaminetetraacetic acid (EDTA) for 36 hours. Subsequently, samples were washed in cacodylate buffer, pH 7.4; postfixed in 1% osmium tetroxide; and washed twice in cacodylate buffer. They were dehydrated using ethanol in increasing concentrations (25–100%), embedded in epoxy resin, cut into ultrathin sections 80 nm in thickness using a Diatome diamond knife, and stained with lead citrate and uranyl acetate. They were then placed on 50 mesh copper grids and observed under TEM (Zeiss 109 EM Turbo).

Osmolarity of each self-etching primer was performed using a microsmometer (The Advanced Micro-Osmometer, Model 3300, Advanced Instrument Inc., Norwood, Massachusetts, USA). For this purpose, 20 µL of CSE and TSO primers was dosed, and osmolarity was analysed in duplicate with the microsmometer, which utilizes freezing point depression thermodynamics. Measurement of the freezing point allows concentrations to be determined with greatest precision owing to the inherent isolation of the sample from the environment by the iced blanket generated when the sample freezes. Each sample was analysed five times in a single batch along the same day.

3. Results and Discussion

3.1. TEM Observations

Group 0. A porous, homogeneous layer of debris formed by degenerated fibrils trapping residual crystallites covered the surface of CAD. Tubules within the surface appeared obstructed by dense smear plugs rich in minerals, while others below the surface of the bur-cut dentin seemed occluded by crystals of different electron densities (Figure 2).

Group 1: CSE. The hybrid layer of about 0.5 µm depth exhibited different sublayers, clearly dissimilar in micromorphology and electron densities (Figure 3).

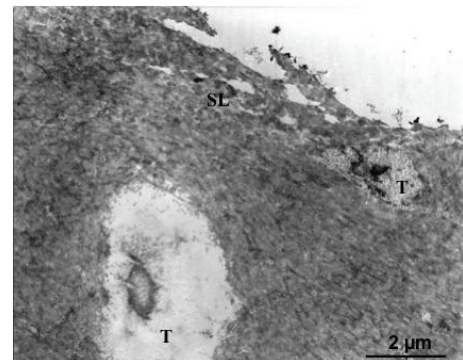


FIGURE 2: TEM photomicrographs of the control group showing the surface of affected dentin homogeneously covered by a porous layer of smear debris (SL) formed by degenerated collagen fibril and minerals. Tubules (T) of the bur-cut dentin are smear plugged while the others below are occluded by large crystallites of different electron densities.

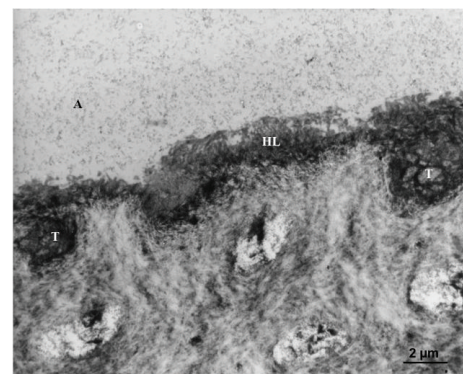


FIGURE 3: The mild self-etching Clearfil SE Bond creates a hybrid layer (HL) of about 0.1 µm depth showing different sublayers of micromorphology and electron densities that can be ascribed to the interaction of the self-etching within the features of affected dentin.

The top layer exhibited an irregular and ruffled border of retained, hybridized smear layer of denatured collagen and scattered mineralized debris. Smear layer material was also seen within the dentin front retained in areas formed by partial dissolution of the peritubular affected dentin (Figure 4).

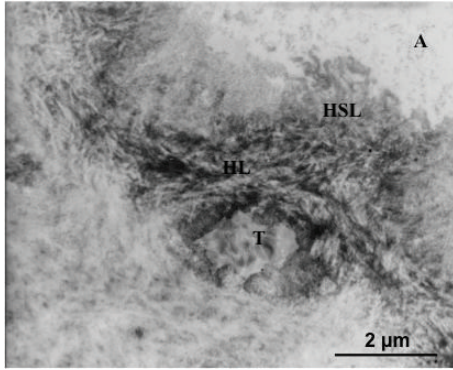


FIGURE 4: An irregular and ruffled border of hybridized smear layer residue is evident at the top of interdiffusion. The dentin front shows voids formed by the partial dissolution of the peritubular dentin, which retain hypermineralized debris.

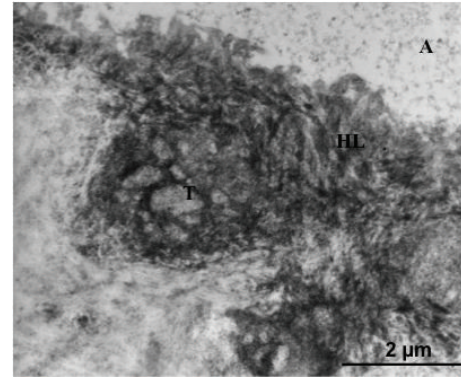


FIGURE 6: Tubules within the interface of Clearfil SE Bond exhibited extreme electron refraction due to the dense infiltration of the peritubular dentine. This hybridization generates a "ring-shaped" reinforcement extended towards the intertubular dentin, which may be interpreted as a morphological aspect of high chemical bonding.

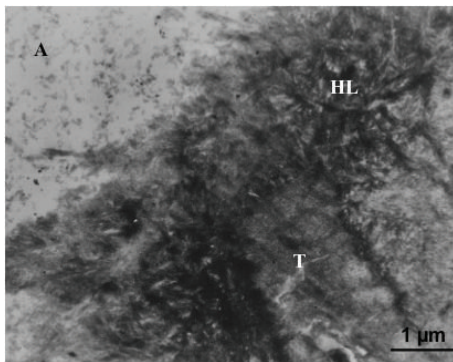


FIGURE 5: Infiltration of affected collagen shows dense crystallites still protecting the affected fibres within the submicron hybrid layer that is attributed to the proper mode of interaction of the mild functional monomer 10-MDP contained in Clearfil SE Bond.

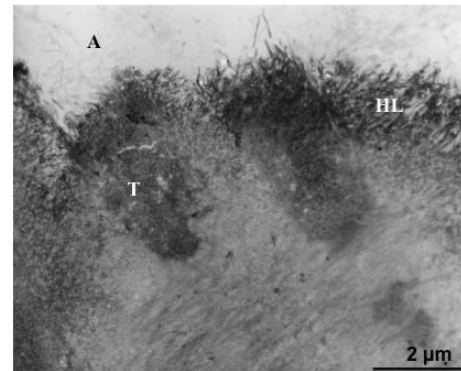


FIGURE 7: The strong self-etching system Tyrian SPE/One-Step Plus forms a 0.2 μm thick hybrid layer (HL) completely devoid of smear layer and HAP as an effect of the modality of interaction of the low pH of the primer within the affected dentin surface.

Below this resin infiltrated smear layer, the intertubular and peritubular affected dentin appeared tightly infiltrated (Figure 5). It was possible to recognize hydroxyapatite (HAP) crystals mostly retained within the affected collagen fibrils. A reinforcement of clearly banded collagen fibrils was seen in the deepest zone of the interdiffusion making a sharply demarked reinforcement to the hybrid base.

Resin tags were not observed in the tubules which retained crystals occasionally associated with mineralized bacterial fragments. Nevertheless, tubules within the interface exhibited extreme electron refraction due to the densely infiltrated peritubular dentine, which formed a "ring-shaped" reinforcement around the orifices extended in the intertubular areas (Figure 6).

Group 2: TSO. A 0.2 μm thick hybrid layer was discerned in TSO interdiffusion. No smear layer was detected but a strongly demineralized front of denatured and ragged fibrils formed the uppermost infiltrated layer. Collagen fibres, associated with detached crystals, were seen arising from the top and projected into the adhesive layer (Figure 7).

Below this smear layer deprived front, the subsurface was characterized by a band of strongly demineralized collagen, separated by large interfibrillar spaces, and porosities. Electron-dense deposits were also seen probably due to reprecipitation of amorphous calcium-phosphates released by the diffusion of the acidic monomer (Figure 8).

At the base of the interdiffusion, a porous band of partially demineralized collagen was seen forming an irregular deeper layer of weak electron densities.

Resin tags were not formed in the dentinal tubules which remained obstructed by crystals. However, dissolution of peritubular dentin and porosities were observed extending toward the intertubular regions (Figure 9).

3.2. Osmolarity Analyses of the Primers. Figure 10 shows that the osmolarity of CSE primer was 3220 mOsm/kg and the osmolarity of TSO primer demonstrated values of 8200 mOsm/kg.

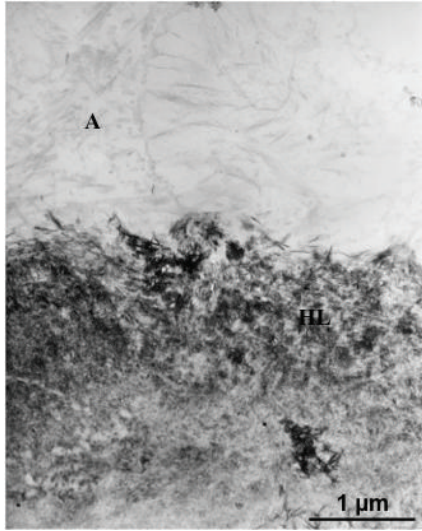


FIGURE 8: The top front of interdiffusion is formed by a band of hydroxyapatite deplete fibres with large interfibrillar spaces. Porosities are crossing the interdiffusion of Tyrian SPE/One-Step Plus. The pickup of the heavy metal stains which characterize the ultrathin TEM section most likely represents the dissolved calcium-phosphates which are included in the interdiffusion. Such resin-encapsulated calcium-phosphates within the exposed collagen fibrils are rather soluble and may result in instability of the interdiffusion and hydrolytic degradation over time.

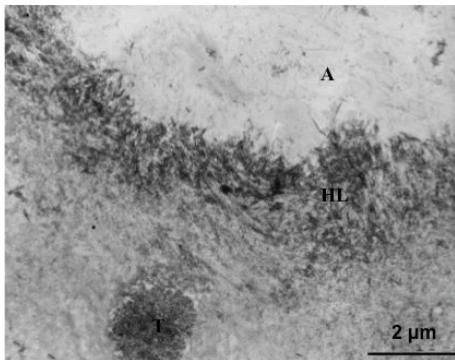


FIGURE 9: The dentinal tubules appeared obstructed by crystals, which were not affected by the low pH of Tyrian SPE/One-Step Plus. Also, the dissolution of peritubular dentin may be related to the acidity of the primer that was not buffered by the tubular crystals. This results in an increase of intertubular demineralization and wetness, which adversely affects the infiltration of the resins.

4. Discussion

Despite the important developments in adhesion in the last decades, bonding in CAD requires further understanding and improvement. Several aspects of enhancing strength and durability of CAD bonding have to be clarified, including understanding the complex heterogeneity and composition of affected dentin, an understanding of the features of the surfaces exposed after cavity preparation and the influence of the characteristics of the adhesives. This increased understanding would be helpful in obtaining a tight resin/dentin

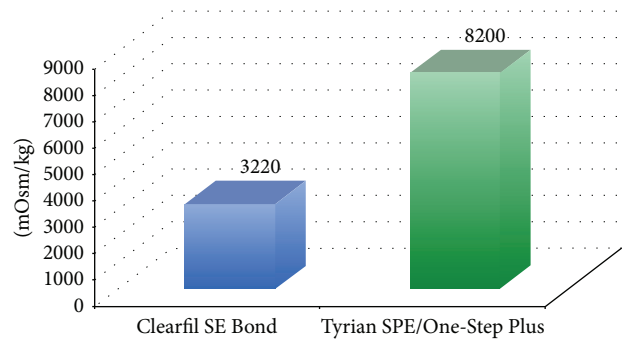


FIGURE 10: Mean values of the osmolarity of the tested materials.

interdiffusion, which is compatible with a stable bond as opposed to nanoleakage and hydrolysis by the host derived matrix metalloproteinase.

In this study, in order to evaluate the capacity of interaction of the two self-etchings in CAD, we standardized the smear by finishing the cavity with an extra-fine diamond bur. This resulted in a thinner layer of smear debris, allowing infiltration of the affected dentin regardless of the pH of the acidic monomers [17]. At the same time, we studied the TEM appearance of the bonding obtained under clinical conditions of pulpal pressure, from the point of view of the pH and osmolarity of the adhesives used.

In the case of the CSE, mild self-etching system, the interdiffusion occurred with the inclusion of the top smear layer and the different features of CAD. Acidification occurred only partially, in comparison to the strong self-etching system TSO, keeping the demineralized HAP crystallites still attached to the fibrils.

The hybrid layer was characterized by retained smear layer residues and scattered needle shape crystallites as an effect of the mild acidity of CSE. No effects attributed to the movement of fluids were observed within the interdiffusion, which appeared tightly sealed by the adhesive resin of CSE. The prevention of movement of fluids through the interface could be attributed to the mild demineralization of intertubular affected dentin and the low osmolarity of the primer, rather than to the presence of mineral occlusion in the dentinal tubules, even in the presence of pulpal pressure. Under clinical conditions of pulpal pressure, water movement may occur by way of the channels of least resistance, that is, the intratubular minerals and the thin peritubular dentin, towards the porous intertubular collagen of CAD, producing interference in the reinforcement and voids of resin [15]. Although the mineral deposits were retained in the tubules, peritubular dentin appeared densely infiltrated and hybridized toward the intertubular regions without evidence of porosities. Also, the hybridization of the peritubular dentin generated a “ring-shaped” reinforcement which has been claimed to be a source of calcium ions that strongly contribute to the high chemical bonding of self-etchings [20].

The high presence of HAP, still protecting the affected fibres within the submicron hybrid layer, is attributed to the proper mode of interaction of the mild functional monomer 10-MDP in CSE. The 10-MDP has the capacity to interact

with the residual HAP establishing primary ionic binding [11, 15, 21–24]. This chemical interaction causes the formation of a regularly layered structure on the surface, within which highly insoluble calcium salts are deposited. Also, the TEM observations show that CLE adequately infiltrates HAP and the partially demineralized collagen matrix, protecting fibrils from being exposed and degraded in environmental fluids [24–27].

The strong self-etching system exhibited different characteristics in CAD. The low pH and high osmolarity of TSO primer played an important role in the morphological aspect of this hybrid layer.

The dentinal front was characterized by deep dissolution of the smear layer and HAP crystallites due to the effect of the strong pH on the affected surface. This produced a hybrid layer whose formation might be similar to that created by the etch and rinse adhesives [28]. Within the calcium-depleted surface the monomer infiltration occurred due to a primary diffusion-based mechanism, creating a bond which is thought to be lower in bond strength than the chemical bonded hybrid layer [22]. The strong pickup of the heavy metal stains which characterized the TEM photomicrographs of this strongly demineralized hybrid layer most likely represents dissolved calcium-phosphates. Such resin-encapsulated calcium-phosphates within the exposed collagen fibrils are somewhat soluble [22, 29] and may result in instability of the interdiffusion, with hydrolytic degradation over time [30].

Also the acidity of TSO and the lower buffer capacity of the tubular crystallites may explain the dissolution of peritubular dentin [12, 13]. These factors resulted in an increase of intertubular demineralization. As a result, demineralization channels were observed extending from both peritubular and intertubular areas and they consisted of small, close-knit aqueous porosities forming a chelation slot, low in infiltrated monomers.

The strong demineralization and the high osmolarity of the primer may have also caused movement of dentinal fluids toward the surface explaining the observation of ragged fibres and detached dentin chips within the adhesive front. Another explanation of the evidence of fluid movements may be the high content of water in self-etching. TSO contains a high concentration of water, which is required to dissociate acidic monomers into ionized forms able to permeate the surface. Water content increases as the acidity of the primer lowers [31]. Mixtures with a high concentration of water and ethanol, such as TSO, may impair polymerization of the monomers within the infiltrated surface [32] allowing the passage of fluids. Furthermore, TSO uses a solvent-rich, hydrophilic adhesive coating rather than a hydrophobic one, such as in CLE. This hydrophilic adhesive was not able to prevent the formation of a permeable membrane after the polymerization, explaining the evidence of water movement within the interface and water porosity in the hybrid layer.

Moreover, the high concentration of solvent in TSO may have an influence on the low bonding demonstrated in clinical studies over 18 months of oral exposure [31]. The low effectiveness of TSO has been explained by an incomplete evaporation of the solvent within the interface, preventing an adequate monomer conversion, which may affect

the mechanical properties, bond strength, and retention rates of the bonding when in an oral environment.

The poor infiltration related to the overaggressive effect of the demineralization, together with the presence of a hydrophilic coating and an incomplete evaporation of the solvent in TSO, may cause a passage of fluids within the hybrid layer, which leads to the degradation of the interdiffusion of TSO in CAD over time.

5. Conclusions

Under clinical conditions, the effectiveness of bonding in CAD with a homogeneous smear layer is strongly influenced by the chemistry of self-etchings.

The mild CSE self-etching produces a dense and homogeneous infiltration of the CAD smear layer, the peritubular dentin, and the affected collagen fibrils. The presence of HAP in the fibrils seems to ensure a tight bonding which is able to resist degradation over time.

Conversely, the strong TSO completely dissolved the smear layer, producing, at the same time, a poor infiltration of the CAD interface. This poor infiltration may be related to the overaggressive effect of the demineralization that, together with a hydrophilic coating and the incomplete evaporation of the solvent in TSO, may be the cause of a passage of fluids within the hybrid layer.

Far from helping the homogeneity of interdiffusion, increasing the pH and osmolarity of self-etchings in CAD may cause nonhomogeneous reinforcement with infiltration of oral fluids and the failure of the bonding over time.

Conflict of Interests

The authors declare that there is no conflict of interests regarding the publication of this paper.

References

- [1] M. Degrange and J. F. Roulet, *Minimally Invasive Restorations with Bonding*, Quintessence, Chicago, Ill, USA, 1997.
- [2] M. Nakajima, H. Sano, M. F. Burrow et al., “Tensile bond strength and SEM evaluation of caries-affected dentin using dentin adhesives,” *Journal of dental research*, vol. 74, no. 10, pp. 1679–1688, 1995.
- [3] K. Ogawa, Y. Yamashita, T. Ichijo, and T. Fusayama, “The ultrastructure and hardness of the transparent layer of human carious dentin,” *Journal of Dental Research*, vol. 62, no. 1, pp. 7–10, 1983.
- [4] G. W. Marshall, S. Habelitz, R. Gallagher, M. Balooch, G. Balooch, and S. J. Marshall, “Nanomechanical properties of hydrated carious human dentin,” *Journal of Dental Research*, vol. 80, no. 8, pp. 1768–1771, 2001.
- [5] M. Nakajima, H. Sano, M. F. Burrow et al., “Tensile bond strength and SEM evaluation of caries-affected dentin using dentin adhesives,” *Journal of Dental Research*, vol. 74, no. 10, pp. 1679–1688, 1995.
- [6] S. Ito, T. Saito, F. R. Tay, R. M. Carvalho, M. Yoshiyama, and D. H. Pashley, “Water content and apparent stiffness of non-caries versus caries-affected human dentin,” *Journal of Biomedical*

- Materials Research Part B: Applied Biomaterials*, vol. 72, no. 1, pp. 109–116, 2005.
- [7] Y. Wang, P. Spencer, and M. P. Walker, “Chemical profile of adhesive/caries-affected dentin interfaces using Raman microspectroscopy,” *Journal of Biomedical Materials Research Part A*, vol. 81, no. 2, pp. 279–286, 2007.
- [8] C. Kaaden, J. M. Powers, K.-H. Friedl, and G. Schmalz, “Bond strength of self-etching adhesives to dental hard tissues,” *Clinical Oral Investigations*, vol. 6, no. 3, pp. 155–160, 2002.
- [9] M. Toledano, R. Osorio, L. Ceballos et al., “Microtensile bond strength of several adhesive systems to different dentin depths,” *American Journal of Dentistry*, vol. 16, no. 5, pp. 292–298, 2003.
- [10] D. H. Pashley, B. Ciucchi, H. Sano, and J. A. Horner, “Permeability of dentin to adhesive agents,” *Quintessence International*, vol. 24, no. 9, pp. 618–631, 1993.
- [11] A. Santini, V. Ivanovic, R. Ibbetson, and E. Milia, “Influence of marginal bevels on microleakage around Class V cavities bonded with seven self-etching agents,” *American Journal of Dentistry*, vol. 17, no. 4, pp. 257–261, 2004.
- [12] D. H. Pashley and R. M. Carvalho, “Dentine permeability and dentine adhesion,” *Journal of Dentistry*, vol. 25, no. 5, pp. 355–372, 1997.
- [13] S.-M. Kwong, F. R. Tay, H.-K. Yip, L.-H. Kei, and D. H. Pashley, “An ultrastructural study of the application of dentine adhesives to acid-conditioned sclerotic dentine,” *Journal of Dentistry*, vol. 28, no. 7, pp. 515–528, 2000.
- [14] S. Sauro, D. H. Pashley, M. Montanari et al., “Effect of simulated pulpal pressure on dentin permeability and adhesion of self-etch adhesives,” *Dental Materials*, vol. 23, no. 6, pp. 705–713, 2007.
- [15] E. Milia, R. Pinna, G. Castelli et al., “TEM morphological characterization of a one-step self-etching system applied clinically to human caries-affected dentin and deep sound dentin,” *American Journal of Dentistry*, vol. 25, no. 6, pp. 321–326, 2012.
- [16] D. H. Pashley, “Smear layer: overview of structure and function,” *Proceedings of the Finnish Dental Society*, vol. 88, pp. 215–224, 1992.
- [17] R. B. Ermis, J. de Munck, M. V. Cardoso et al., “Bond strength of self-etch adhesives to dentin prepared with three different diamond burs,” *Dental Materials*, vol. 24, no. 7, pp. 978–985, 2008.
- [18] P. Spencer, Y. Wang, M. P. Walker, and J. R. Swafford, “Molecular structure of acid-etched dentin smear layers—in situ study,” *Journal of Dental Research*, vol. 80, no. 9, pp. 1802–1807, 2001.
- [19] E. Milia, M. R. Lallai, and F. García-Godoy, “In vivo effect of a self-etching primer on dentin,” *American Journal of Dentistry*, vol. 12, no. 4, pp. 167–171, 1999.
- [20] E. Milia, E. Cumbo, R. J. A. Cardoso, and G. Gallina, “Current dental adhesives systems. A narrative review,” *Current Pharmaceutical Design*, vol. 18, no. 34, pp. 5542–5552, 2012.
- [21] M. C. G. Erhardt, M. Toledano, R. Osorio, and L. A. Pimenta, “Histomorphologic characterization and bond strength evaluation of caries-affected dentin/resin interfaces: effects of long-term water exposure,” *Dental Materials*, vol. 24, no. 6, pp. 786–798, 2008.
- [22] Y. Yoshida, K. Nagakane, R. Fukuda et al., “Comparative study on adhesive performance of functional monomers,” *Journal of Dental Research*, vol. 83, no. 6, pp. 454–458, 2004.
- [23] M. Yoshiyama, A. Urayama, T. Kimochi, T. Matsuo, and D. H. Pashley, “Comparison of conventional vs. self-etching adhesive bonds to caries-affected dentin,” *Operative Dentistry*, vol. 25, no. 3, pp. 163–169, 2002.
- [24] S. Inoue, K. Koshiro, Y. Yoshida et al., “Hydrolytic stability of self-etch adhesives bonded to dentin,” *Journal of Dental Research*, vol. 84, no. 12, pp. 1160–1164, 2005.
- [25] U. Salz, J. Zimmermann, F. Zeuner, and N. Moszner, “Hydrolytic stability of self-etching adhesive systems,” *Journal of Adhesive Dentistry*, vol. 7, no. 2, pp. 107–116, 2005.
- [26] P. Farge, L. Alderete, and S. M. M. Ramos, “Dentin wetting by three adhesive systems: influence of etching time, temperature and relative humidity,” *Journal of Dentistry*, vol. 38, no. 9, pp. 698–706, 2010.
- [27] E. Milia, G. Castelli, A. Bortone et al., “Short-term response of three resin-based materials as desensitizing agents under oral environmental exposure,” *Acta Odontologica Scandinavica*, vol. 71, no. 3-4, pp. 599–609, 2013.
- [28] E. Milia and A. Santini, “Ultrastructural transmission electron microscopy (TEM) study of hybrid layers formed beneath a one-bottle adhesive system using the total-etch technique and a self-etching system,” *Quintessence International*, vol. 34, no. 6, pp. 447–452, 2003.
- [29] B. van Meerbeek, K. Yoshihara, Y. Yoshida, A. Mine, J. de Munck, and K. L. van Landuyt, “State of the art of self-etch adhesives,” *Dental Materials*, vol. 27, no. 1, pp. 17–28, 2011.
- [30] W. W. Brackett, D. A. Covey, and H. A. St. Germain Jr., “One-year clinical performance of a self-etching adhesive in class V resin composites cured by two methods,” *Operative Dentistry*, vol. 27, no. 3, pp. 218–222, 2002.
- [31] A. D. Loguercio and A. Reis, “Application of a dental adhesive using the self-etch and etch-and-rinse approaches: an 18-month clinical evaluation,” *The Journal of the American Dental Association*, vol. 139, no. 1, pp. 53–61, 2008.
- [32] E. L. Pashley, Y. Zhang, P. E. Lockwood, F. A. Rueggeberg, and D. H. Pashley, “Effects of HEMA on water evaporation from water-HEMA mixtures,” *Dental Materials*, vol. 14, no. 1, pp. 6–10, 1998.

Research Article

Assaying Biomarkers via Real-Time Measurements of the Effective Relaxation Time of Biofunctionalized Magnetic Nanoparticles Associated with Biotargets

Shu-Hsien Liao,¹ Jean-Hong Chen,² Yu-Kai Su,¹ Kuen-Lin Chen,³
Herng-Er Horng,¹ and Hong-Chang Yang⁴

¹Institute of Electro-Optical Science and Technology, National Taiwan Normal University, Taipei 116, Taiwan

²Department of Materials Engineering, Kun Shan University, Tainan 710, Taiwan

³Department of Physics, National Chung Hsing University, Taichung 402, Taiwan

⁴Department of Electro-Optical Engineering, Kun Shan University, Tainan 710, Taiwan

Correspondence should be addressed to Shu-Hsien Liao; shliao@ntnu.edu.tw

Received 12 September 2014; Accepted 9 February 2015

Academic Editor: Yali Cui

Copyright © 2015 Shu-Hsien Liao et al. This is an open access article distributed under the Creative Commons Attribution License, which permits unrestricted use, distribution, and reproduction in any medium, provided the original work is properly cited.

An assay of biomarkers consisting of alpha-fetoprotein (AFP) is reported. Real-time measurements of the effective relaxation time τ_{eff} , when the biofunctionalized magnetic nanoparticles (BMNs) were conjugating with biotargets, were made. The BMNs are anti-alpha-fetoprotein (antiAFP) coated onto dextran-coated iron oxide nanoparticles labeled as Fe_3O_4 -antiAFP. It was found that the effective relaxation time, τ_{eff} , increases as the association of AFP and Fe_3O_4 -antiAFP evolves. We attribute this to the enhanced Brownian motion of BMNs when magnetic clusters are present during the conjugation. We found that saturation magnetization, M_s , increases when the concentration of AFP increases. This is due to the fact that more magnetic clusters are associated in the reagent, and therefore the M_s increases when the concentration of AFP increases. The change of effective relaxation time and saturation magnetization shows a behavior of logistic function, which provides a foundation for assaying an unknown amount of biomolecules. Thus, we demonstrate sensitive platforms for detecting AFP by characterizing τ_{eff} . The detection platform is robust and easy to use and shows promise for further use in assaying a broad number of biomarkers.

1. Introduction

Assaying biomarkers based on electrical [1], optical [2, 3], and magnetic technologies [4, 5], and so forth, has been reported, in which, immuomagnetic assays based on magnetic detection using biofunctionalized magnetic nanoparticles (BMNs) have received considerable attention. Magnetic detection has a negligible magnetic background, and thus high detection sensitivity and specificity can be achieved. Magnetic detection can be done through the measurements of magnetic relaxation [6, 7], magnetic remanence [8], immunomagnetic alternating current (ac) susceptibility reduction [9], saturated magnetization [10], spin-spin relaxation [11], and so forth. Detection sensors include SQUIDs [12], magnetoresistive sensors [13], Hall sensors [14], and on-chip magnetic

resonance sensors [15]. Many of these techniques, however, have a time-consuming stage of sample preparation. On the contrary, detecting biomarkers using the immunomagnetic reduction (IMR) assay [9], which detects the change of the amplitude at the mixed-frequency. The method shows high sensitivity and specificity. Additionally, sample preparation is simple and easy to operate. Some studies involving this approach include the detecting of cytokines [16] and alpha-fetoprotein (AFP) for human expressing tumors in clinical research [17].

In contrast to direct detection of magnetic susceptibility reduction at the mixed-frequency, we have recently developed a new magnetic sensing platform, single-frequency ac susceptometer for biodetection [18]. The ac susceptometer detects the phase lag of the magnetization, $M(t)$, of BMNs

with respect to the applied field, $\mathbf{H}(t)$, as the detection mechanism. During the association of BMNs with biomarkers the magnetic clusters are conjugated, which changes the phase lag and in turn changes the time-dependent relaxation rate. In this work, the detection platform was used to assay the biomolecule abundance of alpha-fetoprotein (AFP) by measuring the time-dependent effective relaxation time and saturation magnetization of reagents conjugating with the AFP. Reagents consisted of antiAFP coated onto the Fe_3O_4 magnetic oxides and labeled as Fe_3O_4 -antiAFP. AFP can be used as a biomarker to detect liver tumors. A level above 500 ng/mL of AFP in adults can be indicative of hepatocellular carcinoma, germ cell tumors, and metastatic cancers of the liver. Biomarkers of AFP are first characterized by measuring the phase lag $\theta(t)$, which is between the applied magnetic field $\mathbf{H}(t)$ and magnetization $\mathbf{M}(t)$. Then the dynamic effective relaxation time τ_{eff} was estimated through the following formula: $\tan \theta = \omega \tau_{\text{eff}}$, where ω is the exciting angular frequency. It was found that the change of effective relaxation time, $\Delta \tau_{\text{eff}}$, increases when the AFP completed the association with Fe_3O_4 -antiAFP. Additionally, the saturation magnetization increases as the concentration of AFP increases. We attribute this to the presence of magnetic clusters during the conjugation. A detection sensitivity better than 100 ng/mL of AFP is demonstrated. The detection platform is robust and easy to use, showing promise for further use in a broad number of biomedical applications, such as viruses, proteins, and tumor markers.

The reagent for assaying AFP consists of magnetic nanoparticles (MF-DEX-0060, MagQu, New Taipei, Taiwan) functionalized with antibodies (ab40942; Abcam, Cambridge, MA), against AFP (EA502-Q1053; EastCoast Bio, North Berwick, ME). These magnetic nanoparticles are dispersed in phosphoryl buffer solution with pH = 7.4. Measured with a vibration sample magnetometer, the concentration of magnetic reagents containing Fe_3O_4 -antiAFP was 0.3 emu/g which corresponds to a concentration of 1.2 mg-Fe/mL.

2. Experiments

2.1. Biodetection System. Figure 1 shows the unique design of the sensitive ac magnetic susceptometer. The sensing coils consist of an input coil, pick-up coil, and compensation coil. The input coil, pick-up coil, and compensation coil are, respectively, 4800 turns (4.9 Ω), 1260 turns (1.2 Ω), and 2 turns of wound copper coils. The pick-up coil consisted of two coils wound in opposite directions. The excitation frequency was 9 kHz. The signal from the function generator is first attenuated with a variable resistor ($\sim 1 \text{ M}\Omega$). A compensation coil was applied to improve the balance of the detection coil. A balance of 30 parts per trillion (ppt) is achieved in such a sensing unit. Due to the nonlinear magnetic characteristics of magnetic nanoparticles, when the excitation frequency $f_1(t)$ is applied to the input coil, an excited signal with $nf_1(t)$ components will be generated in the pick-up coil. In the present study, the dynamic $\theta(t)$ and amplitude, χ_{amp} , of the fundamental component, $f_1(t)$, are detected through lock-in detection.

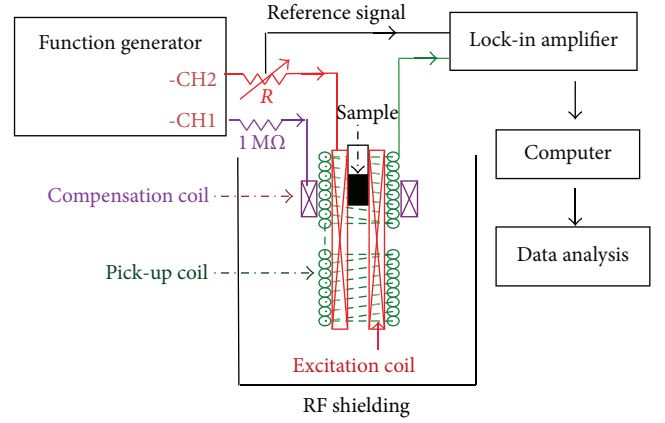


FIGURE 1: The detection scheme of an ac magnetic susceptometer with a lock-in detection technique.

2.2. Detection Mechanism. Due to the molecular interaction, BMNs are associated with biomarkers and the magnetic clusters are conjugated. The magnetization from magnetic clusters will affect the physical properties of the BMNs during the association of BMNs with the biomarkers, for instance, the dynamic phase lag $\theta(t)$ of $\mathbf{M}(t)$ with respect to $\mathbf{H}(t)$ in ac susceptibility and the saturation magnetization, M_s , and so forth. By characterizing the dynamic $\theta(t)$ or M_s , we can therefore determine the unknown amount of biomarkers.

We consider the ac magnetic susceptibility of BMNs, $\chi(\omega)$, in an applied ac magnetic field. $\chi(\omega)$ is a function of τ_{eff} and exciting angular frequency ω . The $\chi(\omega)$ can be expressed as follows [19]:

$$\chi_{\text{ac}} = \chi' + i\chi'' \quad (1)$$

$$= \chi_0 \left\{ \left[\frac{1}{1 + (\omega\tau_{\text{eff}})^2} \right]^2 + \left[\frac{(\omega\tau_{\text{eff}})}{1 + (\omega\tau_{\text{eff}})^2} \right]^2 \right\}^{1/2} e^{-i\theta}, \quad (2)$$

where χ_0 is the component of χ_{ac} at $\omega = 0$, $i = (-1)^{1/2}$, $\chi' = \chi_0 \{1/[1 + (\omega\tau_{\text{eff}})^2]\}$, $\chi'' = \chi_0 \{(\omega\tau_{\text{eff}})/[1 + (\omega\tau_{\text{eff}})^2]\}$, and $\chi''/\chi' = \tan \theta$. θ is the phase lag of the time-varying magnetization \mathbf{M} with respect to the applied ac magnetic field \mathbf{H} , and τ_{eff} is the effective relaxation rate. Using (1) and (2), we obtained $\tan \theta = \omega\tau_{\text{eff}}$ with $\chi''/\chi' = \tan \theta$. The τ_{eff} of BMNs can be written as

$$\frac{1}{\tau_{\text{eff}}} = \frac{1}{\tau_{\text{B,eff}}} + \frac{1}{\tau_{\text{N,eff}}}, \quad (3)$$

where $1/\tau_{\text{B,eff}}$ is the effective relaxation rate due to Brownian relaxation and $1/\tau_{\text{N,eff}}$ is the effective relaxation rate due to Brownian relaxation due to Néel relaxation. We note that τ_{eff} characterizes the ability to retain the magnetization after the applied dc field is removed and it reflects the influences of clustered magnetic nanoparticles on Brownian and Néel relaxation.

Since θ is related to the effective relaxation time, τ_{eff} , by the relation $\tan \theta = \omega\tau_{\text{eff}}$, where ω is the excitation

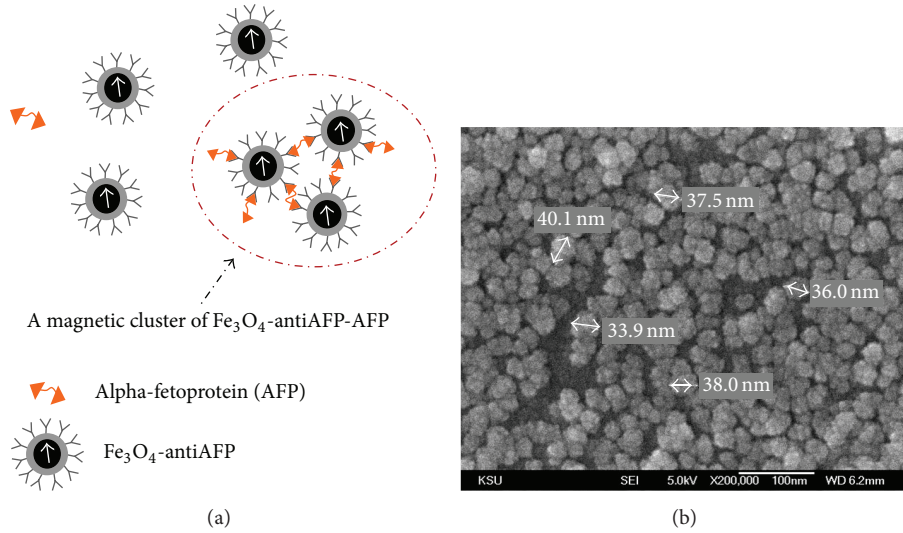


FIGURE 2: A cartoon drawing of AFP, Fe₃O₄-antiAFP, and magnetic clusters of Fe₃O₄-antiAFP-AFP.

frequency, we can understand the dynamic characteristics of $\tau_{\text{eff}}(t)$ by measuring the time-dependency of $\theta(t)$ with a lock-in amplifier. Furthermore, the formation of the magnetic clusters during conjugation affects the relaxation and therefore changes the $\tau_{\text{eff}}(t)$. To quantitatively describe this assay we define $\Delta\tau_{\text{eff}}/\tau_0 = [\tau_{\text{eff}}(t=0) - \tau_{\text{eff}}(t=\infty)]/\tau_{\text{eff}}(t=0)$, where $\Delta\tau_{\text{eff}} = [\tau_{\text{eff}}(t=0) - \tau_{\text{eff}}(t=\infty)]$ and $\tau_{\text{eff}}(t=0) = \tau_0$. We will analyze $\Delta\tau_{\text{eff}}/\tau_0$ to determine amount of biomarkers.

2.3. Reagents. The reagent for assaying AFP consists of magnetic nanoparticles (MF-DEX-0060, MagQu, New Taipei, Taiwan) functionalized with antibodies (ab40942; Abcam, Cambridge, MA) against AFP (EA502-Q1053; EastCoast Bio, North Berwick, ME). These magnetic nanoparticles are dispersed in phosphoryl buffer solution (PBS). The BMNs for assaying AFP are Fe₃O₄-antiAFP dispersed in phosphate buffered saline solution with a pH value of 7.4. The magnetic core is Fe₃O₄, which is coated with dextran. Cartoons of the AFP, Fe₃O₄-antiAFP, and conjugated magnetic clusters of Fe₃O₄-antiAFP-AFP are represented in Figure 2(a) while the SEM picture of the reagent Fe₃O₄-antiAFP is shown in Figure 2(b). The size of the Fe₃O₄-antiAFP is ~ 37 nm, which is close to the average hydrodynamic diameter of ~ 45 nm detected with the dynamic light scattering. To achieve the association between AFP and Fe₃O₄-antiAFP, we used the saturated magnetization of a 0.3 emu/g magnetic reagent. To assay AFP, 60 μL magnetic reagents consisting of Fe₃O₄-antiAFP are mixed with 60- μL AFP of different concentrations, varied from 10 ng/mL to 10000 ng/mL.

3. Results and Discussion

3.1. Time Dependence of Phase Lag θ . Figure 3 shows the time dependence of $\theta(t)$ after mixing the reagents with AFP at 300 K. It was found that $\theta(t)$ is independent of time before the reagent is mixed with the to-be-detected AFP. After mixing the reagent with AFP, the $\theta(t)$ increases

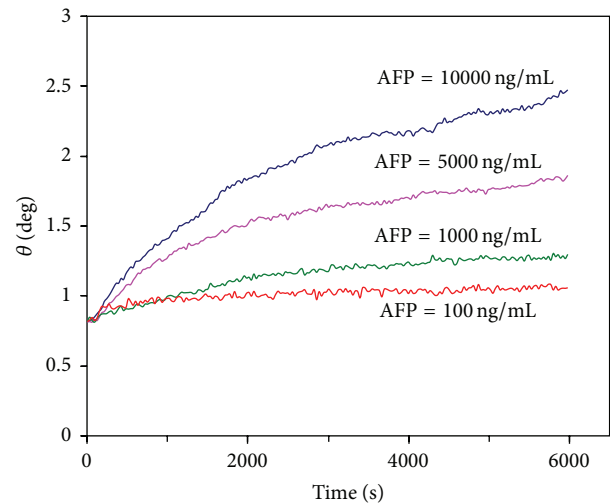


FIGURE 3: Time-dependent θ for assaying 10000 ng/mL, 5000 ng/mL, 1000 ng/mL, and 100 ng/mL of AFP.

monotonically and reaches saturated behavior when the association is completed. The $\theta(t=0) = 0.8$ degrees was observed at $t = 0$ and $\theta(t = 6000 \text{ s})$ increases monotonically to 1.3 degrees at $t = 6000 \text{ s}$ when we assay 1000 ng/mL of AFP, and a change of the phase lag $\Delta\theta = 0.5$ degrees was detected. The $\theta(t=0) = 0.8$ degrees at $t = 0$ and $\theta(t = 6000 \text{ s})$ increases to 1.05 degrees at $t = 6000 \text{ s}$ when we assay 100 ng/mL of AFP, and a change of the phase lag $\Delta\theta = 0.25$ degrees was observed.

Figure 4 shows $\Delta\theta/\theta_0(t=0)$ as a function of AFP concentration in a semilog plot, where $\Delta\theta = \theta(t = 6000) - \theta(t = 0)$. The $\Delta\theta/\theta_0 = 1.76$ ($\Delta\theta = 1.44$) degrees when the concentration of AFP is 10000 ng/mL. The $\Delta\theta$ decreases systematically when the concentration of AFP decreases and $\Delta\theta/\theta_0 = 0.32$ ($\Delta\theta = 0.26$) degrees when the concentration of AFP = 100 ng/mL. If we further decrease the concentration of AFP to 10 ng/mL, the $\Delta\theta/\theta_0$ is saturated to = 0.37. The lowest

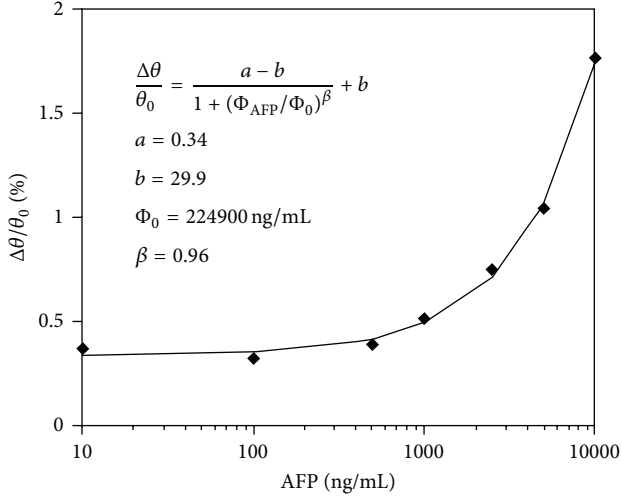


FIGURE 4: $\Delta\theta/\theta_0$ as a function of the AFP concentration in a semilog plot.

detection limit is about 100 ng/mL of AFP in this work. The detection sensitivity can further be improved if we further reduce the noises of the detection system or if SQUID sensors are used [20].

3.2. Dynamic Effective Relaxation Time τ_{eff} . Figure 5 shows the time dependence of τ_{eff} after mixing the reagents with AFP at 300 K. For instance, after mixing the reagent with 5000 ng/mL AFP, τ_{eff} increases from $\tau_{\text{eff}} = 0.26 \mu\text{s}$ at $t = 0$ to $\tau_{\text{eff}} = 0.55 \mu\text{s}$ at $t = 6000$ s. When assaying 1000 ng/mL AFP, we found that $\tau_{\text{eff}} = 0.26 \mu\text{s}$ and $\tau_{\text{eff}} = 0.38 \mu\text{s}$ at $t = 6000$ s. When assaying 100 ng/mL AFP, we found that $\tau_{\text{eff}} = 0.26 \mu\text{s}$ at $t = 0$ and $\tau_{\text{eff}} = 0.32 \mu\text{s}$ at $t = 6000$ s. It takes ~ 1.0 hour to complete the association between 1000 ng/mL AFP and the reagent. However, the association time is reduced to 0.5 hours when we assay 100 ng/mL AFP. Consequently, there is a systematic decrease in assaying time when the AFP concentration is reduced. The $\Delta\tau_{\text{eff}} = 0.41 \mu\text{s}$ when the concentration of AFP is 10000 ng/mL and $\Delta\tau_{\text{eff}} = 0.06 \mu\text{s}$ when the AFP concentration decreases to 100 ng/mL. If we further reduce the AFP concentration to 10 ng/mL, then $\Delta\tau_{\text{eff}}$ remains as $0.08 \mu\text{s}$. This is the system noise which limits the detection sensitivity. When AFP is conjugated with the reagents which consisted of Fe_3O_4 -antiAFP, AFP and Fe_3O_4 -antiAFP will form magnetic clusters. There is an increase in τ_{eff} during the association because of the formation of magnetic clusters, which depresses the Brownian relaxation and therefore increases τ_{eff} .

Molecule-assisted nanoparticle clustering effect in immunomagnetic reduction assay was reported [21]. In that study, the clustering association was manipulated by controlling the concentrations of BMNs in the reagent. It was found that particle clustering is enhanced by an increase in the concentration of BMNs. As the reagents conjugate with biomarkers, magnetic clusters are formed, which depress the Brownian motion. In this work, we show the phase lag of \mathbf{M} with respect to \mathbf{H} , which was characterized to estimate

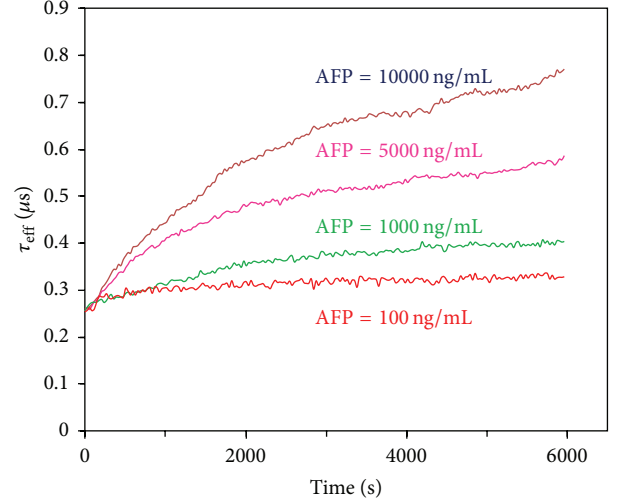


FIGURE 5: Time-dependent τ_{eff} for assaying 10000 ng/mL, 5000 ng/mL, 1000 ng/mL, and 100 ng/mL of AFP.

the time-dependency of τ_{eff} through the following relation: $\tan \theta = \omega\tau_{\text{eff}}$.

A detection scheme for real-time Brownian relaxation of magnetic nanoparticles was also investigated by using a mixed frequency method [22], in which a low frequency of $f_2 = 10$ Hz with a large amplitude and a higher frequency of 20 kHz with a lower amplitude were applied. Instead of detecting the change of amplitudes, the phase delays of the mixed-frequency signals are investigated during the binding process between proteins on BMNs' surface and their respective antibodies. In the present work, instead of using two excitation frequencies, only one exciting frequency was applied with a compensation current to the sensing coil to achieve a high balance. Additionally, the real-time θ is measured to characterize real-time τ_{eff} . By analyzing the changes of real-time τ_{eff} , a detection sensitivity of human AFP better than 100 ng/mL is demonstrated.

3.3. Universal Logistic Function in $\Delta\tau_{\text{eff}}/\tau_0$. Figure 6 shows the normalized effective relaxation time reduction $\Delta\tau_{\text{eff}}/\tau_0$ as a function of AFP concentration in a semilog plot at 300 K, where $\tau_0 = 0.26 \mu\text{s}$ is the effective relaxation time at $t = 0$. The $\Delta\tau_{\text{eff}}/\tau_0 = 1.9$ for assaying 10000 ng/mL of AFP, and then the $\Delta\tau_{\text{eff}}/\tau_0$ decreases to 0.61 when we assay 1000 ng/mL of AFP and the $\Delta\tau_{\text{eff}}/\tau_0$ is further saturated to 0.35 when we assay 10 ng/mL.

The $\Delta\tau_{\text{eff}}/\tau_0$ as a function of AFP concentration will follow a universal characteristic logistic function as follows [16]:

$$\frac{\Delta\tau_{\text{eff}}}{\tau_0} = \frac{(a - b)}{\left\{1 + [(\Phi_{\text{AFP}}) / (\Phi_0)]^\beta\right\}} + b, \quad (4)$$

where τ_0 is the effective relaxation time at $t = 0$. a , b , and γ are dimensionless parameters. Φ_{AFP} and Φ_0 are in units of ng/mL. The solid line is the fitting curve with parameters $a = 0.34$, $b = 29.9$, $\Phi_0 = 224900$ ng/mL, and $\beta = 0.961$. Due

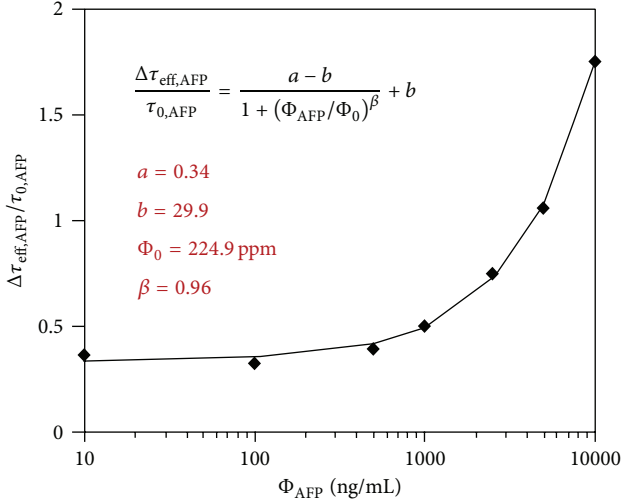


FIGURE 6: $\Delta\tau_{\text{eff}}/\tau_0$ as a function of the AFP concentration in a semilog plot. The solid line is the fitting curve to (4).

to the presence of noises, the $\Delta\tau_{\text{eff}}/\tau_0$ signal shows a nonzero value of $\Phi_{\text{AFP}} = 0$. This universal logistic function provides a basis for estimating the unknown amount of biomolecules [16]. Versatile categories of bioentities, for example, proteins, viruses, small-molecule chemicals, and cytokines, despite being different from each other, have all shown to behave similarly, resulting in a general logistic function for all biotargets. The present concentration-dependent $\Delta\tau_{\text{eff}}/\tau_0$ also shows this behavior of logistic function, which provides a foundation for assaying an unknown amount of biomolecules. The detection threshold of the detected signal is defined as that higher than the noise level of the detected signal at low concentrations. In this work, the lowest noise level of $\Delta\tau_{\text{eff}}/\tau_0$ is about 0.35. Therefore, the detection threshold of AFP concentration can be determined via (4), which results in 55 ng/mL.

Figure 7(a) shows the magnetization as a function of the applied magnetic field for different concentrations of AFP when the association of Fe_3O_4 -antiAFP with AFP is complete. The magnetization was measured with a vibrating sample magnetometer. The concentrations of AFP varied from 10 ng/mL to 10000 ng/mL. It was found that the M_s increases when the concentration of AFP increases. The increased M_s is due to the fact that more magnetic clusters of Fe_3O_4 -antiAFP-AFP are formed during the association. The ΔM_s is 0.32 emu/g when the concentration of AFP is 10000 ng/mL and ΔM_s decreases to 0.06 emu/g when the concentration is 10 ng/mL, where ΔM_s is the change M_s at $H = 1$ T in the reagent with and without AFP. The $\Delta M_{s,\text{AFP}}/M_{s,0}$ as a function of AFP concentration is shown in Figure 7(b). As the concentration of AFP decreases, less magnetic clusters are formed. Therefore the ΔM_s decreases monotonically when the concentration of AFP decreases. The ΔM_s reaches a saturated behavior when the concentration of AFP is 10 ng/mL. Hence, a detection sensitivity of 10 ng/mL of AFP by measuring the variation of saturated magnetization is demonstrated.

The $\Delta M_{s,\text{AFP}}/M_{s,0}$ data are fitted to the universal logistic function:

$$\frac{\Delta M_{s,\text{AFP}}}{M_{s,0}} = \frac{(A - B)}{\left\{1 + \left[\frac{\Phi_{\text{AFP}}}{\Phi_0}\right]^\beta\right\}} + B, \quad (5)$$

where $M_{s,0}$ is the saturated magnetization of Fe_3O_4 -antiAFP. The fitting parameters A and B are in units of emu/g, while Φ_0 is in units of ng/mL, and β is dimensionless. The solid curve is the fitted line with parameters $A = 0.62$ emu/g, $B = 4.3$ emu/g, $\Phi_0 = 5430$ ng/mL, and $\beta = 0.88$. This solid curve provides a foundation for assaying unknown amounts of AFP.

The molecule-assisted nanoparticle clustering effect was reported in immunomagnetic reduction assay [21]. In that study, magnetic particle clustering was manipulated by controlling the concentrations of antibody-functionalized magnetic nanoparticles in the reagent. The results show that particle clustering is enhanced by an increase in the concentration of the to-be-detected biotargets. In the present study, we found that M_s increases when the concentration of AFP increases. This is due to the fact that more magnetic clusters are associated in the reagent, and therefore the M_s increases when the concentration of AFP increases.

Figure 8 shows the representative time-dependent amplitude, χ_{amp} , for assaying 10000 ng/mL AFP (Figure 8(a)) and 50 ng/mL AFP (Figure 8(b)). For assaying 10000 ng/mL AFP, $\chi_{\text{amp}} = 13.4 \mu\text{V}$ at $t = 0$ and decreases to $12.06 \mu\text{V}$ at $t = 6000$ s. Therefore, we obtain $\Delta\chi_{\text{amp}}/\chi_{\text{amp}}(t = 0) = 10\%$ for assaying 10000 ng/mL AFP. For assaying 100 ng/mL AFP, $\chi_{\text{amp}} = 12.33 \mu\text{V}$ at $t = 0$ and decreases to $12.22 \mu\text{V}$ at $t = 6000$ s. Therefore, $\Delta\chi_{\text{amp}}/\chi_{\text{amp}}(t = 0) = 0.9\%$ for assaying 100 ng/mL AFP. It was observed that the amplitude reduction decreases when the concentration of AFP decreases. The amplitude of (1) is $\chi_{\text{amp}} = \chi_0 \left\{ \left[\frac{1}{1 + (\omega\tau_{\text{eff}})^2} \right]^2 + \left[\frac{\omega\tau_{\text{eff}}}{1 + (\omega\tau_{\text{eff}})^2} \right]^2 \right\}^{1/2} = \chi_0 \left\{ \frac{1}{1 + (\omega\tau_{\text{eff}})^2} \right\}^{1/2}$. Therefore an increase in τ_{eff} during the association will cause a reduction in χ_{amp} . We have shown that the magnetic clustering effect is enhanced by increasing the concentration of the AFP. Furthermore, the amplitude reduction shows characteristics similar to that observed in a mixed-frequency IMR [21].

A method of wash-free IMR assay using mixed excitation frequencies was previously proposed [9]. In such detection, the sensing coils consist of two excitation coils and one pick-up coil. Two excitation currents at frequencies $f_1(t)$ and $f_2(t)$ were applied to the excitation coils. The reduction of χ_{ac} for the BMNs conjugated with the target biomarkers is analyzed at a target frequency of $f_1(t) + 2f_2(t)$ to qualitatively determine the amount of biomarkers, where $f_1(t)$ and $f_2(t)$ are the excitation frequencies of the input coils. This mixed-frequency ac susceptibility reduction has been successfully used to assay AFP [17], which shows a high sensitivity and specificity. In the present work a detection threshold better than 100 ng/mL is demonstrated by characterizing the change in the effective relaxation time. The present biosystem has been applied to detect the C-reactive protein via the characterization of $\Delta\theta_{\text{eff}}/\theta_0$ [18]. In practice, the reference criteria of the AFP serum level for the diagnosis of hepatocellular carcinoma (HCC) are above 20 ng/mL. To achieve a higher

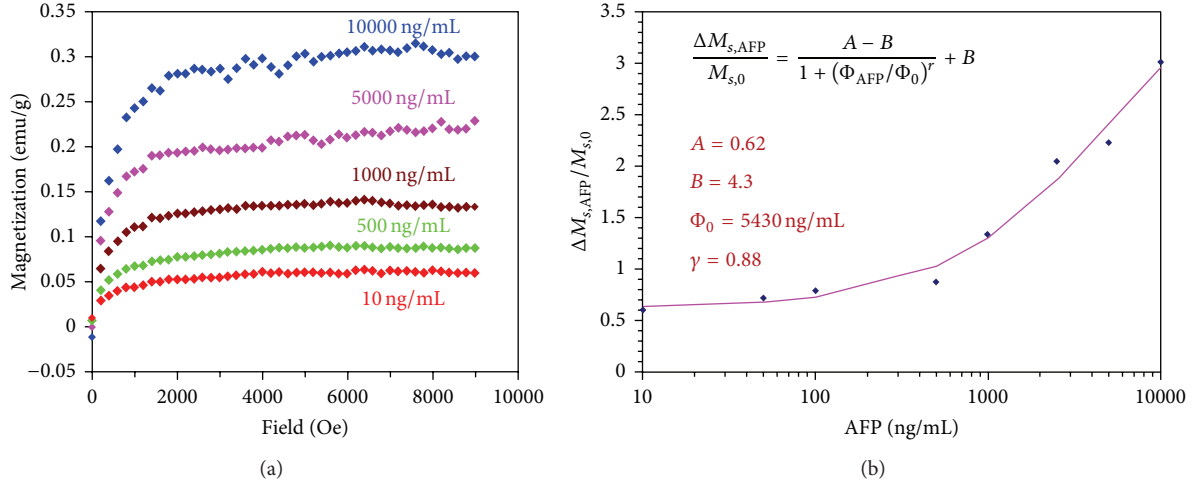


FIGURE 7: (a) Magnetization as a function of applied magnetic field for different concentrations of AFP when the association of Fe_3O_4 -antiAFP with AFP is complete and (b) ΔM_s as a function of AFP concentration.

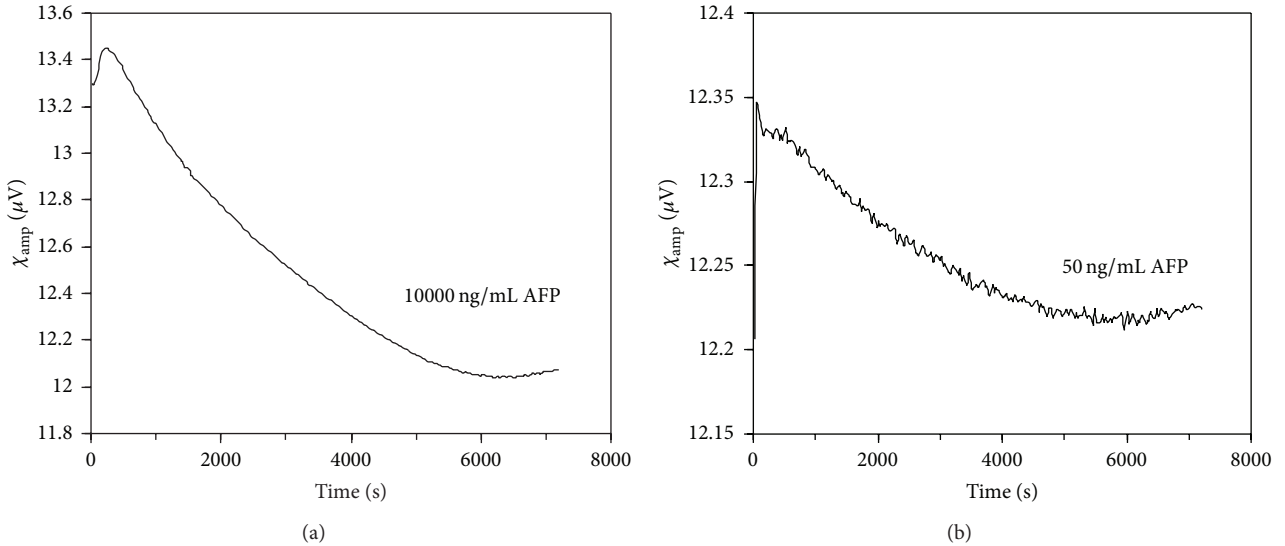


FIGURE 8: Representative time-dependent ac susceptibility for assaying (a) 10000 ng/mL AFP and (b) 50 ng/mL AFP.

detection sensitivity, we can couple the sensing coil to high- T_c SQUID via a flux transformer [20].

4. Conclusion

In this work, we report a platform for assaying biomarkers of AFP by using reagents that consisted of Fe_3O_4 -antiAFP and a highly sensitive ac susceptometer. By monitoring θ , we found that the effective relaxation time increases monotonically and becomes saturated when the association between AFP and Fe_3O_4 -antiAFP is complete. Additionally, the change of τ_{eff} and M_s increases when the concentration of AFP increases after the association. This is due to the fact that more and larger magnetic clusters consisting of Fe_3O_4 -antiAFP-AFP are formed during the association. The concentration-dependent $\Delta\tau_{eff}/\tau_0$ and $\Delta M_{s,AFP}/M_{s,0}$ show a universal

behavior of the logistic function, which provides a foundation for estimating an unknown amount of biomolecules. The detection platforms are robust and easy to use and show promise for further use in biomedical applications.

Conflict of Interests

The authors declare that there is no conflict of interests regarding the publication of this paper.

Acknowledgments

This work is supported under Grants nos. NSCI01-2120-M-168-001, NSC99-2112-M-168-001-MY3, NSCI02-2112-M-003-017, NSCI01-2112-M-003-009, NSCI02-2923-M003-

001, NSC102-2622-M002-001-CC2, NSC102-2112-M-003-008-MY2, and NSC 100-2112-M-003-011-MY2 and the Ministry of Health and Welfare under Grants nos. DOH102-TD-PB-111-TM007 and DOH102-TD-N-111-002.

References

- [1] G. Zheng, F. Patolsky, Y. Cui, W. U. Wang, and C. M. Lieber, "Multiplexed electrical detection of cancer markers with nanowire sensor arrays," *Nature Biotechnology*, vol. 23, no. 10, pp. 1294–1301, 2005.
- [2] K. Aslan, J. R. Lakowicz, and C. D. Geddes, "Plasmon light scattering in biology and medicine: New sensing approaches, visions and perspectives," *Current Opinion in Chemical Biology*, vol. 9, no. 5, pp. 538–544, 2005.
- [3] S. Y. Yang, R. M. Wu, Z. F. Jian, H. E. Horng, C.-Y. Hong, and H. C. Yang, "One-sample measurement in laser nephelometric immunoassay using magnetic nanoparticles," *Applied Physics Letters*, vol. 89, no. 24, Article ID 244102, 2006.
- [4] C. R. Tamanaha, S. P. Mulvaney, J. C. Rife, and L. J. Whitman, "Magnetic labeling, detection, and system integration," *Biosensors and Bioelectronics*, vol. 24, no. 1, pp. 1–13, 2008.
- [5] D. R. Baselt, G. U. Lee, M. Natesan, S. W. Metzger, P. E. Sheehan, and R. J. Colton, "A biosensor based on magnetoresistance technology," *Biosensors and Bioelectronics*, vol. 13, no. 7-8, pp. 731–739, 1998.
- [6] R. Kötitz, W. Weitschies, L. Trahms, W. Brewer, and W. Semmler, "Determination of the binding reaction between avidin and biotin by relaxation measurements of magnetic nanoparticles," *Journal of Magnetism and Magnetic Materials*, vol. 194, no. 1, pp. 62–68, 1999.
- [7] S. K. Lee, W. R. Myers, H. L. Grossman, H.-M. Cho, Y. R. Chemla, and J. Clarke, "Magnetic gradiometer based on a high-transition temperature superconducting quantum interference device for improved sensitivity of a biosensor," *Applied Physics Letters*, vol. 81, no. 16, pp. 3094–3096, 2002.
- [8] K. Enpuku, T. Minotani, T. Gima et al., "Detection of magnetic nanoparticles with superconducting quantum interference device (SQUID) magnetometer and application to immunoassays," *Japanese Journal of Applied Physics*, vol. 38, pp. L1102–L1105, 1999.
- [9] C.-Y. Hong, C. C. Wu, Y. C. Chiu, S. Y. Yang, H. E. Horng, and H. C. Yang, "Magnetic susceptibility reduction method for magnetically labeled immunoassay," *Applied Physics Letters*, vol. 88, no. 21, Article ID 212512, 2006.
- [10] H. E. Horng, S. Y. Yang, C.-Y. Hong et al., "Biofunctionalized magnetic nanoparticles for high-sensitivity immunomagnetic detection of human C-reactive protein," *Applied Physics Letters*, vol. 88, no. 25, Article ID 252506, 2006.
- [11] H. Lee, E. Sun, D. Ham, and R. Weissleder, "Chip-NMR biosensor for detection and molecular analysis of cells," *Nature Medicine*, vol. 14, no. 8, pp. 869–874, 2008.
- [12] Y. R. Chemla, H. L. Grossman, Y. Poon et al., "Ultrasensitive magnetic biosensor for homogeneous immunoassay," *Proceedings of the National Academy of Sciences of the United States of America*, vol. 97, no. 26, pp. 14268–14272, 2000.
- [13] D. R. Baselt, G. U. Lee, M. Natesan, S. W. Metzger, P. E. Sheehan, and R. J. Colton, "A biosensor based on magnetoresistance technology," *Biosensors and Bioelectronics*, vol. 13, no. 7-8, pp. 731–739, 1998.
- [14] T. Aytur, J. Foley, M. Anwar, B. Boser, E. Harris, and P. R. Beatty, "A novel magnetic bead bioassay platform using a microchip-based sensor for infectious disease diagnosis," *Journal of Immunological Methods*, vol. 314, no. 1-2, pp. 21–29, 2006.
- [15] H. Shao, C. Min, D. Issadore et al., "Magnetic nanoparticles and micromr for diagnostic applications," *Theranostics*, vol. 2, no. 1, pp. 55–65, 2012.
- [16] C. C. Yang, S. Y. Yang, J. J. Chieh, H. E. Horng, C. Y. Hong, and H. C. Yang, "Universal behavior of biomolecule-concentration-dependent reduction in AC magnetic susceptibility of bioreagents," *IEEE Magnetics Letters*, vol. 3, p. 1500104, 2012.
- [17] K.-W. Huang, S.-Y. Yang, Y.-W. Hong et al., "Feasibility studies for assaying alpha-fetoprotein using antibody-activated magnetic nanoparticles," *International Journal of Nanomedicine*, vol. 7, pp. 1991–1996, 2012.
- [18] S. H. Liao, H. C. Yang, H. E. Horng et al., "Time-dependent phase lag of biofunctionalized magnetic nanoparticles conjugated with biotargets studied with alternating current magnetic susceptometer for liquid phase immunoassays," *Applied Physics Letters*, vol. 103, no. 24, Article ID 243703, 2013.
- [19] R. E. Rosensweig, "Heating magnetic fluid with alternating magnetic field," *Journal of Magnetism and Magnetic Materials*, vol. 252, pp. 370–374, 2002.
- [20] S. Y. Yang, J. J. Chieh, W. C. Wang et al., "Magnetic nanoparticles for high-sensitivity detection on nucleic acids via superconducting-quantum-interference-device-based immunomagnetic reduction assay," *Journal of Magnetism and Magnetic Materials*, vol. 323, no. 6, pp. 681–685, 2011.
- [21] S. Y. Yang, J. J. Chieh, K. W. Huang et al., "Molecule-assisted nanoparticle clustering effect in immunomagnetic reduction assay," *Journal of Applied Physics*, vol. 113, no. 14, Article ID 144903, 2013.
- [22] L. Tu, Y. Jing, Y. Li, and J.-P. Wang, "Real-time measurement of Brownian relaxation of magnetic nanoparticles by a mixing-frequency method," *Applied Physics Letters*, vol. 98, no. 21, Article ID 213702, 2011.

Research Article

Time-Evolution Contrast of Target MRI Using High-Stability Antibody Functionalized Magnetic Nanoparticles: An Animal Model

K. W. Huang,^{1,2} S. Y. Yang,³ H. E. Horng,⁴ J. J. Chieh,⁴ H. H. Chen,⁴
C. C. Wu,^{5,6} J. H. Chen,⁷ I.T. Lin,^{8,9} C. C. Yang,³ and H. C. Yang¹⁰

¹ Department of Surgery & Hepatitis Research Center, National Taiwan University Hospital, Taipei 100, Taiwan

² Graduate Institute of Clinical Medicine, College of Medicine, National Taiwan University, Taipei 100, Taiwan

³ MagQu Co., Ltd., New Taipei City 231, Taiwan

⁴ Institute of Electro-Optical Science and Technology, National Taiwan Normal University, Taipei 116, Taiwan

⁵ Department of Internal Medicine, National Taiwan University Hospital, College of Medicine, National Taiwan University, Taipei 100, Taiwan

⁶ Department of Primary Care Medicine, National Taiwan University, Taipei 100, Taiwan

⁷ Department of Material Engineering, Kun Shan University, Tainan City 710, Taiwan

⁸ Center for Molecular Imaging and Translational Medicine, Xiamen University, Xiamen 361, China

⁹ Graduate Institute of Electronics Engineering, National Taiwan University, Taipei 106, Taiwan

¹⁰ Department of Electro-Optical Engineering, Kun Shan University, Tainan City 710, Taiwan

Correspondence should be addressed to S. Y. Yang; syyang@magqu.com

Received 30 May 2014; Accepted 23 July 2014; Published 27 August 2014

Academic Editor: Yali Cui

Copyright © 2014 K. W. Huang et al. This is an open access article distributed under the Creative Commons Attribution License, which permits unrestricted use, distribution, and reproduction in any medium, provided the original work is properly cited.

In this work, high-quality antibody functionalized Fe₃O₄ magnetic nanoparticles are synthesized. Such physical characterizations as particle morphology, particle size, stability, and relaxivity of magnetic particles are investigated. The immunoreactivity of biofunctionalized magnetic nanoparticles is examined by utilizing immunomagnetic reduction. The results show that the mean diameter of antibody functionalized magnetic nanoparticles is around 50 nm, and the relaxivity of the magnetic particles is 145 (mM·s)⁻¹. In addition to characterizing the magnetic nanoparticles, the feasibility of using the antibody functionalized magnetic nanoparticles for the contrast medium of target magnetic resonance imaging is investigated. These antibody functionalized magnetic nanoparticles are injected into mice bearing with tumor. The tumor magnetic-resonance image becomes darker after the injection and then recovers 50 hours after the injection. The tumor magnetic-resonance image becomes the darkest at around 20 hours after the injection. Thus, the observing time window for the specific labeling of tumors with antibody functionalized magnetic nanoparticles was found to be 20 hours after injecting biofunctionalized magnetic nanoparticles into mice. The biopsy of tumor is stained after the injection to prove that the long-term darkness of tumor magnetic-resonance image is due to the specific anchoring of antibody functionalized magnetic nanoparticles at tumor.

1. Introduction

Due to its nontoxicity, nanosized, high-stability, iron oxide magnetic nanoparticles have been applied to *in vitro* and *in vivo* medical applications. For *in vitro* medical applications, several groups have published papers about the immunoassay

using biofunctionalized magnetic nanoparticles as labeling markers [1–6]. These papers reveal that the magnetically labeled immunoassay show high sensitivity, low interference, and versatility in clinics [7, 8]. The *in vivo* applications using magnetic nanoparticles may include the magnetic labeling on cells [9, 10], drug delivery [11, 12], hyperthermia [13, 14],

and so forth. Another important application of magnetic nanoparticles in *in vivo* medicine is the contrast medium for magnetic resonance (MR) imaging [15–18].

From the metabolism point of view, the injected magnetic nanoparticles injected into beings are eventually digested with liver. It has been further demonstrated that only normal liver cells can digest the injected magnetic nanoparticles, while liver tumor cells can not absorb the injected magnetic nanoparticles. With the magnetic nanoparticles, the relaxation time of MR like T_2 for normal liver cells is reduced. Thus, for T_2 -weighted MR imaging, the brightness of normal cells is reduced. However, the brightness of T_2 -weighted MR image for liver tumor cells remains unchanged. Therefore, by injecting magnetic nanoparticles into beings, the bright spots on liver MR image are regarded as tumors [19]. Nowadays, iron oxide magnetic nanoparticles are used as contrast medium in clinics for imaging liver tumors.

For other kinds of tumors, target MR imaging using bio-functionalized Fe_3O_4 magnetic nanoparticles is utilized [20–22]. For a given kind of tumor, specific antigens are expressed by the tumor. Magnetic nanoparticles immobilized with antibodies against the antigens are able to bind with the tumor and attribute to the reduction in the relaxation times of MR. Thus, the MR image of the tumor becomes darker when compared with that of surrounding normal cells. Practically, as the antibody functionalized magnetic nanoparticles are injected to beings and are circulated to the tumor, both the tumor and surrounding normal cells are rich in magnetic nanoparticles. Thus, MR images of the tumor and surrounding normal cells become dark. It is impossible to differentiate the tumor from the surrounding normal cells. After a period of time, the tumor keeps the antibody functionalized magnetic nanoparticles, while the magnetic nanoparticles around the normal cells are washed away. During this period of time, the MR image of the tumor is darker than that of the surrounding normal cells. It is easy to find the tumor according to the MR image. But, the binding of the antibody functionalized magnetic nanoparticles with the tumor is not permanent. The bound magnetic nanoparticles with the tumor eventually are digested or washed away after certain period of time. The above descriptions imply that there exists a suitable time window for imaging the tumor using MR. However, the nanoparticles of the imaging time window of MR for target tumors are very rare.

In this work, the time-evolution of MR images of mice bearing with colorectal tumors is recorded after the injection of antibody functionalized Fe_3O_4 magnetic nanoparticles. Besides, the synthesis of antibody functionalized Fe_3O_4 magnetic nanoparticles is introduced. Since colorectal tumors express carcinoembryonic antigen (CEA), antibody against CEA is conjugated onto Fe_3O_4 magnetic nanoparticles. The characterizations, such as particle size, MR relaxivity, stability and magnetization, of these magnetic nanoparticles are examined.

2. Experimental Details

The protocol of synthesizing magnetic Fe_3O_4 nanoparticles was proposed by MagQu Co., Ltd. [23]. The flow chart for

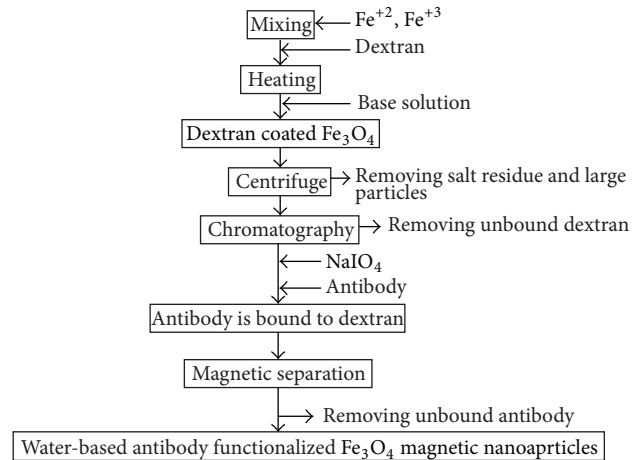


FIGURE 1: Flow chart of synthesizing antibody functionalized magnetic nanoparticles dispersed in PBS solution.

the synthesis of antibody functionalized magnetic nanoparticles is shown in Figure 1. A ferrite solution containing a stoichiometric ratio of 1:2 ferrous sulphate heptahydrate ($FeSO_4 \cdot 7H_2O$) and ferric chloride hexahydrate ($FeCl_3 \cdot 6H_2O$) was mixed with an equal volume of aqueous dextran, which acted as a surfactant for Fe_3O_4 particles dispersed in water. The mixture was heated to 70–90°C and titrated with strong base solution to form black Fe_3O_4 particles. Aggregates and excess unbound dextran were removed by centrifugation and gel filtration chromatography to obtain highly concentrated homogeneous magnetic fluid. The reagent (MF-DEX-0060, MagQu) with desired magnetic concentration was obtained by diluting the highly concentrated magnetic fluid with pH-7.4 phosphate buffered saline (PBS) solution. To make antibodies against carcinoembryonic antigen (CEA) for colorectal cancer, that is, anti-CEA (10C-CR2014M5, Fitzgerald; AT-CEA, MagQu), bound to the dextran on the outmost shell of magnetic nanoparticles, $NaIO_4$ solution was added into the magnetic solution to oxidize dextran, which was then used to create aldehyde groups ($-CHO$). Then, dextran can react with anti-CEA via the linking of $-CH=N-$. Thus, anti-CEA is bound covalently to dextran. Through magnetic separation, unbound anti-CEA was separated from the solution.

The size distribution of Fe_3O_4 magnetic nanoparticles biofunctionalized without/with anti-CEA was analyzed by using dynamic laser scattering (Nanotracer 150, Microtrac). The morphology of anti-CEA functionalized Fe_3O_4 magnetic nanoparticles is analyzed by using a scanning electronic microscope (JSM-6700F, Jeol). The relaxivity of MR for the reagent is measured by 3-T MR imaging instrument (Biospec System, Bruker).

To check the immunoreactivity of anti-CEA functionalized Fe_3O_4 magnetic nanoparticles, the technology so-called immunomagnetic reduction is used [24–26]. The working principle of immunomagnetic reduction (IMR) is illustrated in Figure 2. In IMR, antibody functionalized magnetic nanoparticles are under the actions of multiple ac magnetic fields.

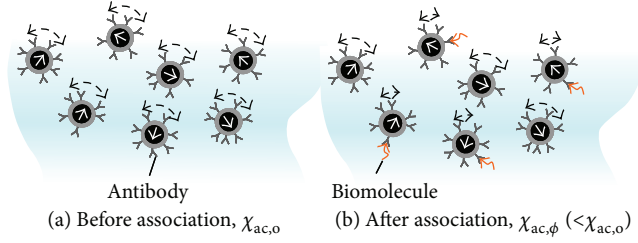


FIGURE 2: Illustration for the mechanism of immunomagnetic reduction.

Thus, magnetic nanoparticles exhibit an ac magnetic susceptibility χ_{ac} . As the antibody functionalized magnetic nanoparticles are mixed with a solution with target biomolecules. Via the antibodies on magnetic nanoparticles, nanoparticles associate with target biomolecules. Before the association, magnetic nanoparticles exhibit an ac magnetic susceptibility, denoted by $\chi_{ac,o}$ in Figure 2(a). After the association, some magnetic nanoparticles become larger, which results in the reduction in the ac magnetic susceptibility. The ac magnetic susceptibility of magnetic nanoparticles after biomolecule-particle association is denoted by $\chi_{ac,\phi}$ in Figure 2(b). $\chi_{ac,\phi}$ is smaller than $\chi_{ac,o}$. The reduction percentage in χ_{ac} of magnetic nanoparticles due to the biomolecule-particle association is defined as IMR signal as follows:

$$\text{IMR} (\%) = \frac{(\chi_{ac,o} - \chi_{ac,\phi})}{\chi_{ac,o}} \times 100\%. \quad (1)$$

The ac magnetosusceptometer (XacPro-E, MagQu) is used to monitor the time dependent χ_{ac} of the anti-CEA functionalized Fe_3O_4 magnetic nanoparticles after mixing with CEA solution. A significant reduction in the ac magnetic susceptibility of magnetic nanoparticles can be found once CEA molecules bind with active anti-CEA on magnetic nanoparticles. Furthermore, more reduction in ac magnetic susceptibility is obtained for more CEA molecules. That is, the sample with higher CEA concentrations shows higher IMR signals. On the other hand, the activity of anti-CEA on magnetic nanoparticles fails; no significant IMR signal can be observed.

For implanting the colorectal tumors, the injections of the CT-26 cell line were processed through the skin on the backs of 8-week-old mice. Three weeks later, 0.06 emu/g and 100 μL of anti-CEA magnetic reagent were injected into the tail veins of five mice. Two groups of mice are used for examinations of MR imaging and Prussian blue (PB) staining, respectively, as tabulated in Table 1. Group 1 formed with two mice, numbered as mouse 1 and mouse 2, is examined using MR imaging instrument. The MR examination schedule was at the 0th, 18th, 30th, 48th, 72nd, and 96th hours for mouse 1 and at the 0th, 12th, 24th, and 46th hours for mouse 2. Here, 0th hour represents the time just before injection. Proving that the anti-CEA Fe_3O_4 magnetic nanoparticles were bound to the tumor tissue required determining the Fe using Prussian blue (PB) staining to examine the tumor tissue of Group 2, which is formed with mouse 3, mouse 4,

TABLE 1: Two groups of mice used for the examinations of MR imaging and PB staining.

Group	Mouse number	Experiment
1	1 and 2	Magnetic resonance (MR) imaging
2	3, 4, and 5	Prussian blue (PB) staining

and mouse 5, which were euthanized at the 0th, 24th, and 98th hours, respectively. The tissue staining was processed (Laboratory Animal Center, National Taiwan University, Taipei, Taiwan), and the $\times 400$ magnification of the optical images was observed using a light microscope.

The 3-T MR imaging (Biospec System, Bruker) and a volume coil were used for T_2 -weighted images. In parallel with the arrangement of the anesthetized mouse, a long tube filled with deionized (DI) water was inserted as the intensity reference to dismiss the instrument drift at various times. Producing the coronal images of each entire mice body at 2 mm intervals required nearly 2 hours.

3. Results and Discussion

The distribution of particle diameter of dextran-coated Fe_3O_4 magnetic nanoparticles is analyzed using dynamic laser scattering. The results are shown in the upper part of Figure 3(a) with the schematically illustration of dextran-coated Fe_3O_4 magnetic nanoparticle. The mean diameter of dextran-coated Fe_3O_4 magnetic nanoparticles was found to be 42.80 nm. After immobilizing anti-CEA on the dextran-coated Fe_3O_4 magnetic nanoparticles, the distribution of particle diameter is analyzed, as shown in the lower part of Figure 3(a). In the inset, the Ys on the dextran-coated Fe_3O_4 magnetic nanoparticle denote anti-CEA. The mean diameter of anti-CEA functionalized Fe_3O_4 magnetic nanoparticles was found to be 51.3 nm, which is larger than that of dextran-coated Fe_3O_4 magnetic nanoparticles by 8.5 nm. Hence, the thickness of anti-CEA on the outmost layer of Fe_3O_4 magnetic nanoparticles is around 4.25 nm. The shapes of the antibody functionalized magnetic nanoparticles are examined by using scanning electronic microscope and are shown in Figure 3(b). It is obvious that each particle is almost identical. Hence, the homogeneity of particle size is high.

To investigate the stability of the suspension of antibody functionalized Fe_3O_4 magnetic nanoparticles in PBS solution, the storing-period dependent mean diameter of nanoparticles is explored. In case of low-stability suspension, the magnetic nanoparticles initially suspended in individual in PBS solution agglomerate with each other as time goes by. An increase in the mean diameter of nanoparticles will be observed. On the other hand, if the mean diameter of nanoparticles was observed to be unchanged, the stability of suspension of magnetic nanoparticles in PBS solution was high. The experimental results are shown in Figure 4. The reagent of antibody functionalized Fe_3O_4 magnetic nanoparticles is stored at 2–8°C. It is clear in Figure 4 that the mean diameter of antibody functionalized Fe_3O_4 magnetic nanoparticles in PBS solution remains around 50 nm for 7.7-month storage.

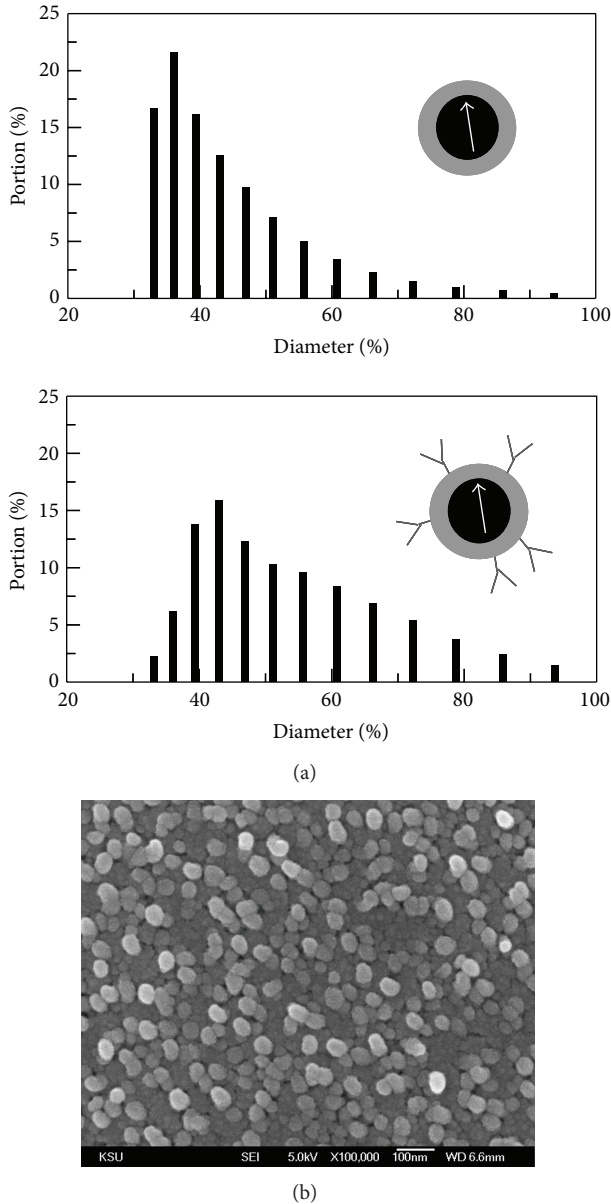


FIGURE 3: Analysis of particle diameter for Fe_3O_4 magnetic nanoparticles (a) without (upper) and with (lower) antibodies suspended in PBS solution using dynamic laser scattering and (b) with antibodies using scanning electronic microscope.

The results evidence the high-stability suspension of antibody functionalized Fe_3O_4 magnetic nanoparticles in PBS solution.

It is important to check the immunoreactivity of anti-CEA as conjugated onto dextran-coated Fe_3O_4 functionalized magnetic nanoparticles. One of methods for this check is to observe the association between the anti-CEA functionalized Fe_3O_4 magnetic nanoparticles and CEA molecules in PBS solution. The method used in this experiment for observing the nanoparticle-CEA association is so-called immunomagnetic reduction [24–26]. The time dependent ac magnetic susceptibility χ_{ac} of the reagent mixing with 5 ng/mL CEA

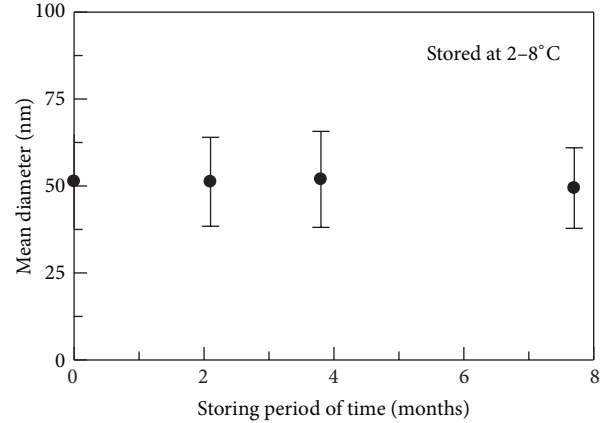


FIGURE 4: Storing-period dependent mean diameter of antibody functionalized Fe_3O_4 magnetic nanoparticles.

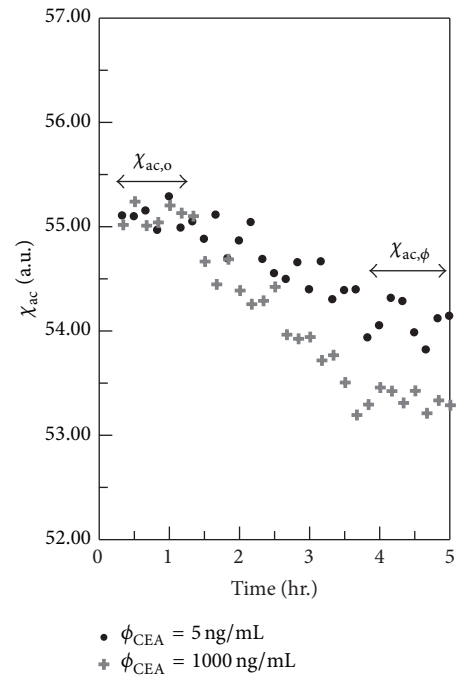


FIGURE 5: Time dependent ac magnetic susceptibility of reagent reacting with CEA in PBS solution of various CEA concentrations.

solution was recorded and shown with dots in Figure 5. It was found that χ_{ac} of the reagent keeps unchanged just after mixing with the CEA solution, as labeled with $\chi_{ac,o}$ in Figure 5. After one hour, the χ_{ac} of the reagent starts to reduce. The reduction in χ_{ac} of the reagent is not terminated until 3.8 hours after the mix of the reagent and the CEA solution. The IMR signal via (1) was found to be 1.68%. The reduction in χ_{ac} of the reagent proves the association between the anti-CEA functionalized Fe_3O_4 magnetic nanoparticles and CEA molecules. As the CEA concentration is increased, say 1000 ng/mL, the reduction in χ_{ac} of the reagent is enhanced, as presented with cross symbols in Figure 5. The IMR signal for 1000 ng/mL CEA

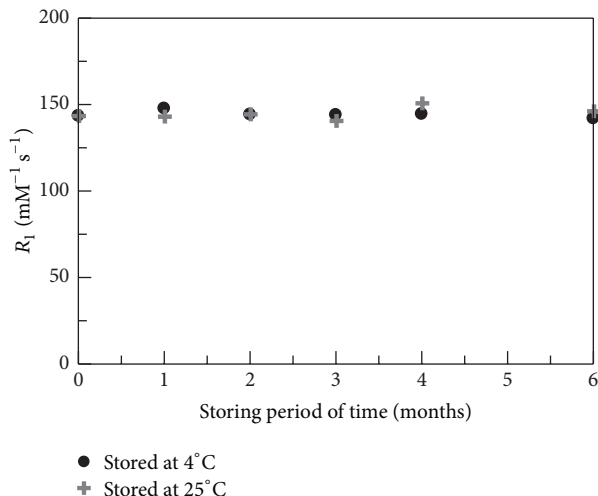


FIGURE 6: Storing period of time dependent relaxivity R_1 of MR for the solutions of dextran-coated magnetic nanoparticles stored at 4°C and 25°C, respectively.

solution is found to be 3.17% via (1). The observed reduction in the χ_{ac} of the reagent in Figure 5 demonstrates that the anti-CEA functionalized Fe_3O_4 magnetic nanoparticles are capable of binding with CEA molecules.

To examine the MR stability of the Fe_3O_4 magnetic nanoparticles suspended in PBS solution, the time-evolution relaxivity of MR, for example, R_1 , is detected. It is worth noting that the solution of dextran-coated Fe_3O_4 magnetic nanoparticles is separated into two groups stored at 4°C and 25°C, respectively. The measured relaxivity R_1 of MR as a function of the storing period of time is shown in Figure 6. It was found that R_1 is around $145 \text{ mM}^{-1}\text{s}^{-1}$ for the solution of dextran-coated magnetic nanoparticles. Furthermore, the R_1 keeps unchanged for six months no matter the solution of dextran-coated magnetic nanoparticles is stored at 4°C or 25°C. This means that the magnetic stability of dextran-coated Fe_3O_4 magnetic nanoparticles can be six months at least.

The anti-CEA functionalized Fe_3O_4 magnetic nanoparticles with high-stability magnetism and suspension are injected into mice implanted with colorectal tumor cells, CT-26. The time-evolution MR images of the tumor are taken after the injection into mouse 1, as shown in Figure 7. The tumor is circled and indicated with an arrow. The brightness of the images at a certain instant is normalized to that of water. The normalized brightness is referred to as image contrast. The image contrast of the circled tumor is analyzed at every image-taking instant. Then, the image contrast of the circled tumor at 0 h is used as a reference value. The ratio in the images contrast of the circled tumor at every image-taking instant to that at 0 h is calculated and shown with dots in Figure 8. The cross symbols in Figure 8 correspond to the time dependent image contrast for mouse 2. The results for both mice definitely show that the image contrast of the colorectal tumor becomes the most significant at around 20 hours after the injection. According to the data shown in

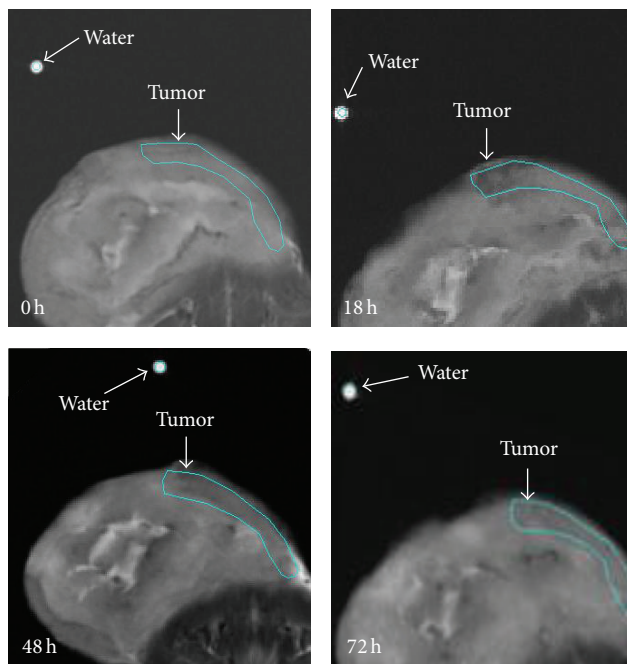


FIGURE 7: Temporal 3-T MR images after the injection of antibody functionalized Fe_3O_4 magnetic nanoparticles into a mouse implanted with tumor (CT-26) from 0 hour (0 h) to 96 hours (96 h).

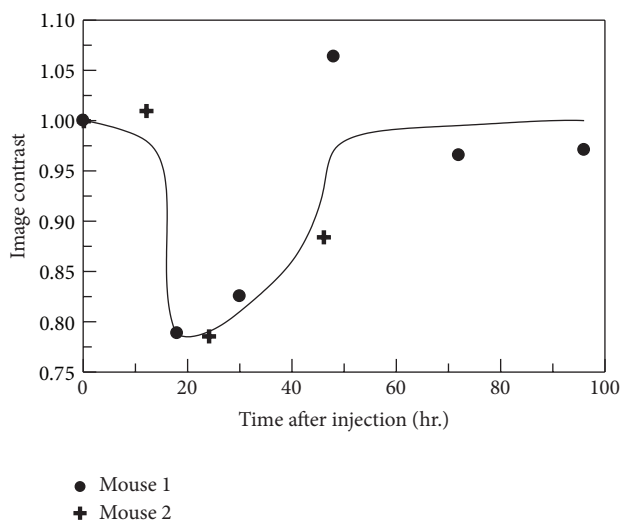


FIGURE 8: Time dependent MR image contrast of the implanted colorectal tumor in mice after the injection of anti-CEA functionalized Fe_3O_4 magnetic nanoparticles.

Figure 8, the brightness of the tumor is reduced by 22% at 20 h as compared to that at 0 h. The brightness of the colorectal tumor recovers after 50 hours after the injection.

The reduction in the brightness of MR image for the colorectal tumor is deduced to be due to the association of anti-CEA functionalized Fe_3O_4 magnetic nanoparticles with the tumor. To prove this deduction, the biopsy of the colorectal tumors in other mice injected with anti-CEA

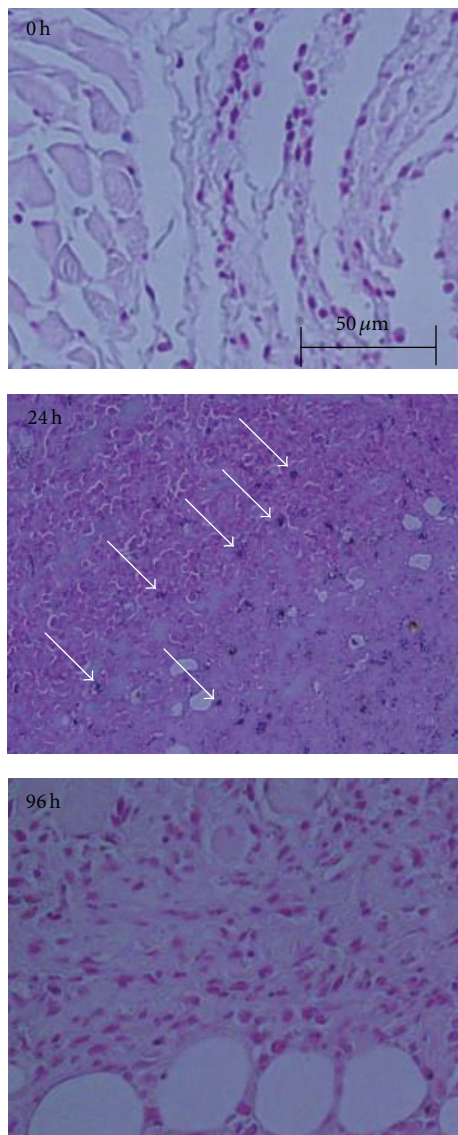


FIGURE 9: Temporal images of Prussian blue staining for the tumor tissue after the injection of antibody functionalized Fe_3O_4 magnetic nanoparticles into a mouse implanted with tumor (CT-26) at 0 hour (0 h), 24 hours (24 h) and 96 hours (96 h).

functionalized Fe_3O_4 magnetic nanoparticles is inspected with tissue staining. To investigate the existence of Fe in the tissue, Prussian blue staining is processed. The results of the Prussian blue staining for tumor tissues taken at various instants after the injection of anti-CEA functionalized Fe_3O_4 magnetic nanoparticles are shown in Figure 9. Before the injection of magnetic nanoparticles, there is no Fe-spot in the tumor tissue. The brightness of MR image of the tumor should remain unchanged; that is, image contrast = 1. This coincides with the results shown in Figure 8. However, lots of Fe-spots can be found in the tumor tissue at 24 hours after the injection, as labeled with arrows. This implies that the brightness of the MR image of the tumor is obviously reduced; that is, image contrast < 1, which is consistent with

the result in Figure 8. At 98 hours after the injection, Fe-spot in the tissue disappears. The brightness of the MR image of the tumor should recover, as found in Figure 8. The results in Figure 9 prove that the reduction in the brightness of MR image of the colorectal tumor is due to the association of anti-CEA functionalized Fe_3O_4 magnetic nanoparticles with the tumor.

Through the careful inspection of Figure 8, significant reduction in the brightness of MR image of the colorectal tumor happens from 20 hours to 40 hours after injecting anti-CEA functionalized Fe_3O_4 magnetic nanoparticles into mice. This means that the anti-CEA functionalized magnetic nanoparticles stay on the tumor for almost 20 hours. Therefore, the suitable time window for MR imaging of the tumor with an aid of antibody functionalized Fe_3O_4 magnetic nanoparticles is from 20 hours to 40 hours after the tail-vein injection.

4. Conclusions

High-stability antibody functionalized Fe_3O_4 magnetic nanoparticles are synthesized for the use of contrast medium of MR imaging. By injecting these nanoparticles into mice, target MR imaging, such as imaging colorectal tumor, is demonstrated. It is further clarified that the suitable time window for MR imaging for the target tumor is from 20 hours to 40 hours after the tail-vein injection.

Conflict of Interests

The authors declare that there is no conflict of interests regarding the publication of this paper.

Acknowledgments

This work was supported by the Ministry of Science and Technology of Taiwan, under Grant nos. 102-2112-M-003-017, 102-2923-M-003-001, 102-2120-M-168-001, 102-2112-M-168-001, 102-2221-E-003-008-MY2, and 101-2221-E-003-005, by the Ministry of Health and Welfare of Taiwan under Grant nos. DOH101-TD-N-111-004, DOH100-TD-N-111-008, and DOH100-TD-PB-111-TM022, and by the Ministry of Economic Affairs of Taiwan under Grant nos. 101-EC-17-A-17-II-0074, 1Z970688, and 1Z0990415 (SBIR).

References

- [1] R. Kötitz, W. Weitschies, L. Trahms, W. Brewer, and W. Semmler, "Determination of the binding reaction between avidin and biotin by relaxation measurements of magnetic nanoparticles," *Journal of Magnetism and Magnetic Materials*, vol. 194, no. 1, pp. 62–68, 1999.
- [2] K. Enpuku, D. Kuroda, A. Ohba et al., "Biological immunoassay utilizing magnetic marker and high T_c superconducting quantum interference device magnetometer," *Japanese Journal of Applied Physics*, vol. 42, no. 12, pp. L1436–L1438, 2003.
- [3] H. E. Horng, S. Y. Yang, Y. W. Huang, W. Q. Jiang, C.-. Hong, and H. C. Yang, "Nanomagnetic particles for SQUID-based magnetically labeled immunoassay," *IEEE Transactions on Applied Superconductivity*, vol. 15, no. 2, pp. 668–671, 2005.

- [4] C. Hong, C. C. Wu, Y. C. Chiu, S. Y. Yang, H. E. Horng, and H. C. Yang, "Magnetic susceptibility reduction method for magnetically labeled immunoassay," *Applied Physics Letters*, vol. 88, no. 21, Article ID 212512, 2006.
- [5] H. Krause, N. Wolters, Y. Zhang et al., "Magnetic particle detection by frequency mixing for immunoassay applications," *Journal of Magnetism and Magnetic Materials*, vol. 311, no. 1, pp. 436–444, 2007.
- [6] S. H. Liao, H. C. Yang, H. E. Horng et al., "Time-dependent phase lag of biofunctionalized magnetic nanoparticles conjugated with biotargets studied with alternating current magnetic susceptometer for liquid phase immunoassays," *Applied Physics Letters*, vol. 103, Article ID 24 3703, pp. 1–3, 2013.
- [7] K. W. Huang, S. Y. Yang, Y. W. Hong et al., "Feasibility studies for assaying α -fetoprotein using antibody-activated magnetic nanoparticles," *International Journal of Nanomedicine*, vol. 7, pp. 1991–1996, 2012.
- [8] M. J. Chiu, S. Y. Yang, T. F. Chen et al., "New assay for old markers-plasma beta amyloid of mild cognitive impairment and Alzheimer's disease," *Current Alzheimer Research*, vol. 9, no. 10, pp. 1142–1148, 2012.
- [9] J. K. Hsiao, M. F. Tai, H. H. Chu et al., "Magnetic nanoparticle labeling of mesenchymal stem cells without transfection agent: Cellular behavior and capability of detection with clinical 1.5 T magnetic resonance at the single cell level," *Magnetic Resonance in Medicine*, vol. 58, no. 4, pp. 717–724, 2007.
- [10] K. G. Neoh and E. T. Kang, "Surface modification of magnetic nanoparticles for stem cell labeling," *Soft Matter*, vol. 8, no. 7, pp. 2057–2069, 2012.
- [11] T. Hiroki, S. Taira, H. Katayanagi et al., "Functional magnetic nanoparticles for use in a drug delivery system," *Journal of Physics*, vol. 200, no. 12, Article ID 122003, 2010.
- [12] H. W. Yang, M. Y. Hua, H. L. Liu, C. Y. Huang, and K. C. Wei, "Potential of magnetic nanoparticles for targeted drug delivery," *Nanotechnology, Science and Applications*, vol. 5, no. 1, pp. 73–86, 2012.
- [13] A. Ito, M. Shinkai, H. Honda, and T. Kobayashi, "Heat-inducible *TNF- α* gene therapy combined with hyperthermia using magnetic nanoparticles as a novel tumor-targeted therapy," *Cancer Gene Therapy*, vol. 8, no. 9, pp. 649–654, 2001.
- [14] T. Kobayashi, "Cancer hyperthermia using magnetic nanoparticles," *Biotechnology Journal*, vol. 6, no. 11, pp. 1342–1347, 2011.
- [15] B. A. Moffat, G. Ramachandra Ready, P. McConville et al., "A novel polyacrylamide magnetic nanoparticle contrast agent for molecular imaging using MRI," *Molecular Imaging*, vol. 2, no. 4, pp. 324–332, 2003.
- [16] B. Chertok, B. A. Moffat, A. E. David et al., "Iron oxide nanoparticles as a drug delivery vehicle for MRI monitored magnetic targeting of brain tumors," *Biomaterials*, vol. 29, no. 4, pp. 487–496, 2008.
- [17] L. Bu, J. Xie, K. Chen et al., "Assessment and comparison of magnetic nanoparticles as MRI contrast agents in a rodent model of human hepatocellular carcinoma," *Contrast Media and Molecular Imaging*, vol. 7, no. 4, pp. 363–372, 2012.
- [18] J. Huang, X. Zhong, L. Wang, L. Yang, and H. Mao, "Improving the magnetic resonance imaging contrast and detection methods with engineered magnetic nanoparticles," *Theranostics*, vol. 2, no. 1, pp. 86–102, 2012.
- [19] Y. X. Wang, "Superparamagnetic iron oxide based MRI contrast agents: current status of clinical application," *Quantitative Imaging in Medicine and Surgery*, vol. 1, no. 1, pp. 35–40, 2011.
- [20] A. Bogdanov Jr. and M. L. Mazzanti, "Molecular magnetic resonance contrast agents for the detection of cancer: past and present," *Seminars in Oncology*, vol. 38, no. 1, pp. 42–54, 2011.
- [21] L. A. Carbonaro, F. Pediconi, N. Verardi, R. M. Trimboli, M. Calabrese, and F. Sardanelli, "Breast MRI using a high-relaxivity contrast agent: an overview," *American Journal of Roentgenology*, vol. 196, no. 4, pp. 942–955, 2011.
- [22] W. Cheng, Y. Ping, Y. Zhang, K. Chuang, and Y. Liu, "Magnetic resonance imaging (MRI) contrast agents for tumor diagnosis," *Journal of Healthcare Engineering*, vol. 4, no. 1, pp. 23–46, 2013.
- [23] W. Jiang, H. C. Yang, S. Y. Yang et al., "Preparation and properties of superparamagnetic nanoparticles with narrow size distribution and biocompatible," *Journal of Magnetism and Magnetic Materials*, vol. 283, no. 2-3, pp. 210–214, 2004.
- [24] C. Y. Hong, C. C. Wu, Y. C. Chiu, S. Y. Yang, H. E. Horng, and H. C. Yang, "Magnetic susceptibility reduction method for magnetically labeled immunoassay," *Applied Physics Letters*, vol. 88, no. 21, Article ID 212512, 2006.
- [25] J. J. Chieh, S.-Y. Yang, H.-E. Horng et al., "Immunomagnetic reduction assay using high- T_c superconducting-quantum-interference-device-based magnetosusceptometry," *Journal of Applied Physics*, vol. 107, no. 7, Article ID 074903, 2010.
- [26] C. C. Yang, S. Y. Yang, H. H. Chen et al., "Effect of molecule-particle binding on the reduction in the mixed-frequency alternating current magnetic susceptibility of magnetic bio-reagents," *Journal of Applied Physics*, vol. 112, no. 2, p. 024704, 2012.